

Aus dem
**Laser-Forschungslabor der Laser-Immunologie-Forschungs-Einrichtung
(LIFE-Zentrum)**

Ludwig-Maximilians-Universität München

Bereichsleitung: PD Dr. rer. biol. hum. Ronald Sroka

Direktor: Prof. Dr. med. Christian Stief

UNTERSUCHUNGEN ZUR LASERINDUZIERTEN LITHOTRIPSIE

Dissertation

zum Erwerb des Doktorgrades der Humanbiologie
an der Medizinischen Fakultät der
Ludwig-Maximilians-Universität zu München

vorgelegt von
Maximilian Eisel
aus München
2019

Mit Genehmigung der Medizinischen Fakultät
der Universität München

Berichterstatter: PD Dr. rer. biol. hum. Ronald Sroka

Mitberichterstatter: PD Dr. med. Markus Bader
Prof. Dr. med. Alexander Karl

Mitbetreuung durch den
promovierten Mitarbeiter: Dr. rer. nat. Adrian Rühm

Dekan: Prof. Dr. med. dent. Reinhard Hickel

Tag der mündlichen Prüfung: 17.12.2019

Inhaltsverzeichnis

Publikationsliste	1
Abstract.....	3
Zusammenfassung.....	5
Untersuchungen zur laserinduzierten Lithotripsie	7
Pathogenese & Pathophysiologie humaner Harnsteine	7
Diagnose der Urolithiasis.....	9
Therapie der Urolithiasis.....	10
Originalmanuskripte.....	13
In vitro investigations of propulsion during laser lithotripsy using video tracking.....	14
Holmium:yttrium-aluminum-garnet laser induced lithotripsy: in-vitro investigations on fragmentation, dusting, propulsion and fluorescence.....	23
Investigation of optical properties of dissected and homogenized biological tissue	39
Literaturverzeichnis.....	51
Danksagung.....	61
Lebenslauf	62
Persönliche Daten.....	62
Berufserfahrung.....	62
Schule & Studium	62
Wissenschaftliche Lehre.....	63
Eidesstattliche Versicherung.....	65



PUBLIKATIONSLISTE

Veröffentlichungen in begutachteten Fachmagazinen:

- **Maximilian Eisel**, Stephan Ströbl, Thomas Pongratz, Frank Strittmatter, Ronald Sroka, „*In vitro investigations of propulsion during laser lithotripsy using video tracking*“, Lasers Surg. Med., 50: 333-339. doi:10.1002/lsm.22770 (2018), **JIF**: 2.726
- **Maximilian Eisel**, Stephan Ströbl, Thomas Pongratz, Frank Strittmatter, and Ronald Sroka, „*Holmium:yttrium-aluminum-garnet laser induced lithotripsy: in-vitro investigations on fragmentation, dusting, propulsion and fluorescence*“, Biomed. Opt. Express 9, 5115-5128 (2018), **JIF**: 3.482
- **Maximilian Eisel**, Stephan Ströbl, Thomas Pongratz, Herbert Stepp, Adrian Rühm, Ronald Sroka, „*Investigation of optical properties of dissected and homogenized biological tissue*“, J. Biomed. Opt. 23(9) 091418 (24 September 2018), **JIF**: 2.367
- Sroka, Ronald; Dominik, Nikolas; **Eisel, Maximilian**; Esipova, Anna; Freymüller, Christian; Heckl, Christian; Hennig, Georg; Homann, Christian; Höhne, Nicolas; Kammerer, Robert; Kellerer, Thomas; Lang, Alexander; Markwardt, Niklas; Pohla, Heike; Pongratz, Thomas; Schmedt, Claus-Georg; Stepp, Herbert; Ströbl, Stephan; Ulaganathan, Keerthanan; Zimmermann, Wolfgang; Rühm, Adrian; *Research and developments of laser assisted methods for translation into clinical application*; Frontiers of Optoelectronics 10(3) 239-254 (2017)
- **Maximilian Eisel**, Frank Strittmatter, Stephan Ströbl, Christian Freymüller, Thomas Pongratz, Ronald Sroka, „*Comparative investigation of multiple-used and single-use flexible endoscopes for urological interventions*“
(Im Revisionsprozess)
- Markus Bader, **Maximilian Eisel**, Frank Strittmatter, Abdulmajeed Alghamdi, Christian Stief, Thomas Pongratz, Ronald Sroka, „*Endoscopic clearance lithotripsy devices bench comparison of stone elimination capacity and drilling speed*“ (geteilte Autorenschaft)
(In Bearbeitung)
- **Maximilian Eisel**, Thomas Pongratz, Frank Strittmatter, Stephan Ströbl, Ronald Sroka, „*Comparison of 1.94 μm Thulium fiber laser, 2.1 μm Ho:YAG laser and 2.94 μm Er:YAG laser: Applicability and efficiency for laserinduced lithotripsy*“
(In Bearbeitung)
- Alexander Kretschmer, Abdulmajeed Alghamdi, **Maximilian Eisel**, Christian Stief, Ronald Sroka, Frank Strittmatter „*Evaluation of a single use ureterorenoscope in patients with kidney stones*“
(In Bearbeitung)

Veröffentlichungen in „Conference Proceedings“:

- **Maximilian Eisel**, Keerthanan Ulaganathan, Frank Strittmatter, Thomas Pongratz, Ronald Sroka, "*Investigations to improve laser induced lithotripsy (Conference Presentation)*," Proc. SPIE 10038, Therapeutics and Diagnostics in Urology: Lasers, Robotics, Minimally Invasive, and Advanced Biomedical Devices, 100380E (19 April 2017);
- Ronald Sroka, **Maximilian Eisel**, Thomas Pongratz, Keerthanan Ulaganathan, Frank Strittmatter, "*Investigations on the fluorescence of urinary stones: how to assist the MD (Conference Presentation)*," Proc. SPIE 10038, Therapeutics and Diagnostics in Urology: Lasers, Robotics, Minimally Invasive, and Advanced Biomedical Devices, 1003804 (19 April 2017);
- Ronald Sroka, Thomas Pongratz, Frank Strittmatter, **Maximilian Eisel**, Stephan Ströbl, "*In-vitro investigation on fragmentation/ dusting and fluorescence during Ho:YAG-Laser induced lithotripsy (Conference Presentation)*," Proc. SPIE 10468, Therapeutics and Diagnostics in Urology 2018, 1046807 (14 March 2018);

weitere Konferenzbeiträge:

- Mündlicher Vortrag: *In-vitro investigation on fragmentation and dusting effects during Ho:YAG-Laser induced lithotripsy* auf der European Conferences on Biomedical Optics (ECBO) EW4D.4, Medical Laser Applications and Laser-Tissue Interactions (MLA), München, 2017

Erfindungsmeldungen:

- **Eisel, Maximilian**; Ströbl, Stephan; Sroka, Ronald *Vorrichtung zur bildgestützten, objektiven Quantifizierung und Bewegungsanalyse bei laserinduzierter Lithotripsie*, 29. April 2017, Aktenzeichen 20 2017 002 293.1, Erfindung freigegeben
- **Eisel, Maximilian**; Ströbl, Stephan; Sroka, Ronald *Vorrichtung zum Schutz endoskopischer Komponenten vor ungewollter Laserapplikation*, 6. Juli 2017, Aktenzeichen 20 2017 003 565.0, Erfindung freigegeben

ABSTRACT

The ureterorenoscopy (URS) with laser induced lithotripsy is a preferred endoscopic method for the treatment of lithiasis and is in direct competition to extracorporeal shockwave lithotripsy (ESWL) and percutaneous nephrolitholapaxy (PCNL). During the laser induced lithotripsy pulsed laser light is guided to the urinary calculus via a light guide wire through the working channel of an endoscope, the stone hence is fragmented by photothermal and mechanical effects. The Ho:YAG laser (λ : 2.1 μm) ranks as gold standard for therapy of urolithiasis, due to the high absorption of this wavelength in water (α : 2.78 mm^{-1}) and good transmission in low OH light guide wire systems. The applied laser energy causes a force to the stone and adjacent fragments, whereby stone movement (propulsion) is induced. Repelled fragments can be hardly detectable or may lead to an increased operation time due to tracking of lost fragments with the endoscope. For one thing remaining fragments potentially result in increased recurrence rates or secondly to overall longer operation time.

To address this medical need, a measurement set-up was constructed for the quantification of the fragmentation rate and propulsion at different laser parameters (optical pulse length, energy per pulse and repetition rate). With the objective to improve the locating of stones and fragments, the spectral fluorescence characteristics of human kidney stones were investigated via fluorescence microscopy using different excitation wavelength.

The systematic evaluation of ablation rates at different laser parameters (Energy (E): 0.5 J/pulse - 2.5 J/pulse, repetition rate (f): 10 Hz - 80 Hz, optical pulse length (t): 0.3 ms - 4 ms) were investigated by shredding artificial calculi (Bego, mixture 15:4, edge length 5mm). In particular the so-called term “dusting” was studied, where the stone is dusted (fragment size < 1 mm) instead of fragmented by carefully chosen laser parameters. The advantage of dusting technology is that the sediment/debris can be flushed out via the rinsing flow due to the small particle size.

The investigation of the propulsion was performed in a set-up consisting of an acrylic glass vessel with a reduced inner bore (\varnothing : 8 mm), which was used as a guiding tube for the artificial stone, accelerated due to laser application from the bottom side. As a result of hydrodynamic and gravitation, the stone returns to its initial position. The movement is recorded via a high-speed camera (1000 fps) and subsequently converted to a movement profile by an image-processing algorithm. A quantification of the propulsion can be made by evaluation and averaging of rising flanks' slopes, respective the mean velocity of the stone.

Human kidney stones were investigated for their fluorescence response at different excitation wavelengths (400 ± 5 nm, 450 ± 10 nm und 550 ± 5 nm), using a spectral fluorescence microscopy. The remitted fluorescence light was detected by a spectrometer after passing specific long pass filters ($\lambda > 470$ nm, $\lambda > 520$ nm, $\lambda > 590$ nm). Additional fluorescence response ($\lambda > 610$ nm) of two kidney stones was observed *in vivo* intraoperatively via an endoscopic camera system at green excitation (λ : 500-570 nm).

The optical tissue properties, absorption and reduced scattering, were investigated via spatial resolved remission and integrating sphere measurements on porcine tissue samples (liver, lung, brain, muscle). The focus was on the comparability and reproducibility between the results gained from dissected versus homogenized tissue samples. New Ho:YAG four cavity laser systems are capable to produce repetition rates up to 100 Hz, pulse energies up to 6 J and pulse lengths up to 4 ms. Collateral damage to surrounding tissue, may occur as a result of the high average laser power either

by direct laser impact to the tissue or due to heating of the mixture of urine and irrigation fluid. The performed evaluation of optical tissue properties can be also translated to the mid infrared wavelength range and can be used as a basis for investigations of collateral damages due to medical laser applications. Therefore, the results of this work can be an important indicator for future technical development of medical laser devices.

ZUSAMMENFASSUNG

Die laserinduzierte Lithotripsie ist eine endoskopische Methode zur Behandlung von Harnsteinleiden. Sie steht in direkter Konkurrenz zur extrakorporalen Stoßwellenlithotripsie (ESWL) und der perkutanen Nephrolitholapaxie (PCNL). Bei der laserinduzierten Lithotripsie wird gepulstes Laserlicht über einen Lichtwellenleiter im Arbeitskanal eines Endoskops direkt auf den Harnstein geleitet und sorgt dort aufgrund photothermischer und mechanischer Effekte für die Zerkleinerung des Steines. Der Ho:YAG Laser (λ : 2.1 μm) gilt aufgrund der hohen Absorption dieser Wellenlänge in Wasser (α : 2.78 mm^{-1}) und der guten Transmission der mittleren-Infrarotstrahlung in Low-OH Glasfasern als Goldstandard für diese Vorgehensweise in der Steintherapie.

Die eingebrachte Laserenergie bewirkt aber auch eine Krafteinwirkung auf den Stein und umliegende Fragmente was zu einer Steinbewegung führt (Propulsion). Durch die Propulsion können zurückgestoßene Fragmente schwer auffindbar sein oder die Operation aufgrund zeitintensiven Nachführens des Endoskops erschweren. Dies kann einerseits zu einer erhöhten Rezidivrate durch Fragmentreste oder zu insgesamt längeren Operationszeit führen.

Daher wurde ein modellhafter Aufbau zur Quantifizierung von Fragmentierungsraten und Propulsionseinflüssen durch Variation der Laserparameter (Energie pro Puls, Repetitionsrate und optische Pulslänge) bei der Ho:YAG laserinduzierten Lithotripsie entwickelt. Des Weiteren wurden die Fluoreszenzeigenschaften von humanen Nierensteinen mittels spektraler Fluoreszenzmikroskopie bei unterschiedlichen Anregungswellenlängen betrachtet, mit dem Ziel das Auffinden von Steinen und Fragmenten technisch zu vereinfachen.

Zur Quantifizierung der Abtragsraten wurde ein Messaufbau konstruiert und im Rahmen von Untersuchungen systematisch verschiedene Laserparameter (Energie (E): 0.5 J/Puls - 2.5 J/Puls, Repetitionsraten (f): 10 Hz - 80 Hz, optische Pulsdauer (t) 0.3 ms - 4 ms an künstlichen Steinen (Bego, Mischverhältnis 15:4, Kantenlänge 5mm) bewertet. Bei der Fragmentierung (Ablation) wurde insbesondere das sogenannte "Dusting" untersucht. Hierbei ist das Ziel den Stein aufgrund geschickt gewählter Laserparameter zu zerstäuben (Fragmente < 1mm) und direkt mit den Spülstrom auszuwaschen.

Die Untersuchung der Propulsion erfolgte mit einem Messaufbau, bestehend aus einem Plexiglasröhrchen mit einer konisch zulaufenden Innenbohrung (\varnothing : 8 mm), welches als Führung für den durch bodenseitige Laserapplikation nach oben beschleunigten künstlichen Stein dient. Aufgrund von Hydrodynamik und Schwerkraft wird der Stein in seine Ausgangsposition zurückgebracht. Diese Steinbewegung wird mit einer High-Speed-Kamera (1000 Bilder/s) aufgenommen und per Software in ein Bewegungsprofil umgewandelt. Durch Bestimmung der Steigung für jede der aufsteigenden Flanken, respektive der mittleren Geschwindigkeit in diesem Zeitintervall, kann eine Quantifizierung der Propulsion erreicht werden.

Von Patienten stammende Harnsteine wurden mit einem Fluoreszenzmikroskop *in vitro* für die Anregungswellenlängen (400 ± 5) nm, (450 ± 10) nm und (550 ± 5) nm auf ihre Fluoreszenz untersucht. Das remittierte Fluoreszenzlicht durchlief vor der spektralen Detektion je nach Anregungslicht verschiedene Langpassfilter ($\lambda > 470$ nm, $\lambda > 520$ nm, $\lambda > 590$ nm). Zusätzlich wurde *in vivo* die Fluoreszenzantwort zweier Nierensteine während einer OP bei grüner Anregung ($\lambda = 500$ - 570 nm) im Spektralbereich oberhalb 610 nm mit einem Endoskopkamarasystem beobachtet.

Die optischen Gewebeeigenschaften, Absorption und reduzierte Streuung, wurden am Schweinemodell (Leber, Lunge, Gehirn, Muskel) über orts aufgelöste Remissions- und Ulbrichtkugelmessungen bestimmt. Die Bestimmung der optischen Eigenschaften von seziierten und homogenisierten Gewebeproben am Schweinemodell fokussierte sich auf die Vergleichbarkeit und Reproduzierbarkeit der Messergebnisse für diese beiden Präparationsmethoden. Neue Ho:YAG Lasersysteme mit vier Laserkavitäten bieten eine große Variation an Laserparametern: Repetitionsraten bis zu 100 Hz, Pulsenergien bis 6 J und Pulslängen von bis zu 4 ms. Durch die hohen eingebrachten mittleren optischen Leistungen (bis zu 120 W) können Kollateralschäden an umliegenden Geweben entweder durch direkten Laserbeschuss oder durch die Erhitzung des Gemisches aus Harn- und Spülflüssigkeit kommen. Die durchgeführten Experimente zur Bestimmung der optischen Eigenschaften sind auch für Laserlicht den mittleren Infrarotbereich anwendbar, bilden die Basis für Untersuchungen zu möglichen Kollateralschäden bei medizinischen Laseranwendungen und können somit wichtige Anhaltspunkte für zukünftige technische Entwicklung von medizinischen Lasergeräten mit sich bringen.

UNTERSUCHUNGEN ZUR LASERINDUZIERTEN LITHOTRIPSIE

Diese Arbeit wird als kumulative Dissertation vorgelegt und besteht aus drei veröffentlichten Originalmanuskripten. Zwei dieser Manuskripte verbinden inhaltlich die modellhaften Messaufbauten zur Quantifizierung von Steinabtragsraten und Propulsion bei Laserlichtapplikation (**Ho:YAG** 2.1 μm) an künstlichen Nierensteinen. Bei den Steinabtragsraten erfolgte die Bewertung zum einen durch die Quantifizierung des durch Ablation erzeugten „**Dusts**“ (Fragmente $< 1\text{ mm}$), zum anderen wurde die Gesamtapplikationszeit und die Zeit des ersten Zerbrechens des Steins ausgewertet. Die **Propulsion** beschreibt eine Bewegung des Steins aufgrund der applizierten Laserenergie. Durch High-Speed-Kameraaufnahmen erhaltene Bewegungsprofile war eine quantitative Aussage über die Stärke der Steinbewegung möglich. Durch Variation der Laserparameter (optische Pulslänge, Repetitionsfrequenz, Energie pro Puls) ist es möglich die Steinabtragseffizienz, als auch die Propulsion zu beeinflussen. Die Aufgabenstellung war derart gestaltet, dass entsprechende Messaufbauten zur Quantifizierung des **Steinabtrages** und der Propulsion entwickelt werden sollten und an geeigneten Laserquellen Versuchsreihen bei variablen Laserparametern durchgeführt werden. Zusätzlich konnte das breitbandige **Fluoreszenzmissionsspektrum** humaner Nierensteine bei unterschiedlichen Anregungswellenlängen durch Fluoreszenzmikroskopie gezeigt werden. Das dritte Manuskript behandelt die Vermessung **optischer Eigenschaften** (Absorption, reduzierte Streuung) von tierischen Geweben (Gehirn, Leber, Lunge Muskel) mittels Ulbrichtkugel- und ortsaufgelöster Remissionsmessung im Wellenlängenbereich von 520 nm bis 800 nm. Die Gewebe wurden dazu in dünne Scheiben seziiert oder zu einer Paste homogenisiert. Durch die Bestimmung der optischen Gewebeeigenschaften lassen sich grundsätzlich Rückschlüsse auf die optische Eindringtiefe des Lichts ziehen und initial potentielle Kollateralschäden durch die Wechselwirkung des Laserlichts mit dem betroffenen Gewebe abschätzen. Die jeweiligen Aufgabenstellungen motivierten sich aus technischen Fortschritten in der Ho:YAG Laserentwicklung (**Unternehmensrelevanz**) und dem direkten Bedarf aus der **Klinik**: Eine effiziente Steinfragmentierung bei geringer Propulsion und raschem Auffinden, kann zu einer kürzeren und schonenderen Behandlungsdauer des Patienten führen, wodurch zum einen wirtschaftliche Aspekte (OP-Belegungszeiten pro Patient, Erhöhung der OP-Dichte pro Tag), aber auch für die Patienten positive Effekte (erhöhte Steinfreiheit, kürzere Krankenhausverweildauer) abgedeckt werden können.

PATHOGENESE & PATHOPHYSIOLOGIE HUMANER HARNSTEINE

Die Steinentstehung in Hohlorganen wird allgemein als Lithiasis bezeichnet und je nach Lokalisation (Niere, Harnleiter, Blase, Gallenblase/-gänge) in: **Urolithiasis** [Nephrolithiasis (Niere), Ureterolithiasis (Harnleiter), Zystolithiasis (Blase)] [1, 2] und Cholelithiasis [Cholezystolithiasis (Gallenblase), Choledocholithiasis (Gallengänge)] unterteilt [3, 4]. Auch in Drüsengeweben können Konkreme ausgebildet werden (z. B. Sialolithiasis) [5, 6]. Die Prävalenz von Harnsteinen liegt bei $> 5\%$, Rezidivraten werden mit bis zu 50% angegeben, bei entsprechender Metaphylaxe kann diese unter 5% betragen [7-14]. Konkreme sind meist erst bei Obstruktion harnableitender Passagen und einer daraus folgenden Rückstauung der Harnflüssigkeit mit Dilatation des Hohlkörpersystems (Niere, Harnleiter, Blase, Harnröhre) problematisch [15]. Durch die Rückstauung der Harnflüssigkeit kann es zur Ausbildung eines Hydroureters, einer Hydronephrose bis hin zum

akuten Nierenversagen kommen [16, 17]. Typische Obstruktionsstellen sind im oberen Harnleiter in Höhe des unteren Nierenpols, an großen Blutgefäßen bei Unter- (Vasa testicularia/ovarica) bzw. Überkreuzung (Vasa iliaca externa), sowie beim Durchtritt der Harnleiter durch die Wand der Harnblase [16]. Obstruktionen äußern sich in einer akuten Nierenkolik mit starken an- und abschwellenden Schmerzen mit Ausstrahlung in den rückwärtigen Flankenbereich, den Bauchbereich oder die Leiste. Je nach Schmerzlokalisation kann bereits eine grobe Einschätzung über die Obstruktionslage erfolgen. Während Konkreme im Nierenbecken oder subpelvinen Ureter Flankenschmerzen mit Ausstrahlung in den medialen Unterbauch zeigen, werden Schmerzsymptome die in die Leistengegend ausstrahlen eher Konkrementen im mittleren oder distalen Ureter zugeordnet [7, 9, 18]. Zusätzlich können Mikro- oder Makrohämaturien nachgewiesen werden [8]. Weitere mögliche Symptome äußern sich in Fieber, Oligurie, Algurie oder Polygurie, sowie in einer allgemeinen Abweichung von der normalen Miktionsfähigkeit [7, 8, 18, 19]. Humane Harnsteinarten lassen sich nach ihrer Vorkommenshäufigkeit im Patienten nach Tabelle 1 darstellen [9, 20, 21].

Tabelle 1: Humane Harnsteinarten nach ihrer Vorkommenshäufigkeit.

Kalzium-Oxalat	> 75 %
Harnsäure	ca.10 %
Magnesium-Ammonium-Phosphat	ca. 5 %
Kalzium-Phosphat	ca. 5 %
Zystin	< 5 %

Harnsteine entstehen durch Konklieren aus dem Urin ausgefallter Stoffe, wodurch sich mit der Zeit größer werdende Konkreme bilden können [22, 23]. Zu den Hauptursachen zählen eine Verringerung des Urinvolumens (Eindicken des Urins), eine erhöhte Calcium-/Oxalat-Sekretion, eine Veränderung des Urin pH-Werts oder Harnwegsinfektionen (ureasebildende Bakterien). Infektiöse Harnsteine sind ein urologischer Notfall und werden durch Antibiotikatherapie, sowie sofortiger Entlastung des betroffenen Harnweges (Stentsetzung, Steintherapie) behandelt [7, 24]. Auch spezielle Krankheitsbilder sowie deren Therapieansatz (Medikamenteninduziert) [25], genetisch bedingte Ursachen [26] und die persönliche Lebensweise (Ernährung, Bewegung) können für die Prädisposition von Harnsteinen eine Rolle spielen [7, 21]. Bei den häufig vorkommenden Kalzium-Oxalat-Steinen wird Randall-Plaque als Anwachsstelle für eine bevorzugte Anreicherungsstelle dieser Stoffe verantwortlich gemacht [22, 27-31]. Randall-Plaques sind Kalzifikationen der in die kleinen Nierenkelche mündenden Markpapillen (Papillae renalis) durch Kalzium-Phosphat (Apatit), das sich ringförmig um die im Nephron befindlichen Tubuli innerhalb der Membranschicht anlagert und nach Verlust der Epithelschicht durch Verdrängung eine Verbindung zu den aus dem Harn ausfallenden Stoffen bilden kann. Zusätzlich wird davon ausgegangen, dass eine Kalzifikation aufgrund der wechselnden Strömungseigenschaften (laminar zu turbulent) in der ab- und aufsteigenden Vasa recta stattfinden und so zusätzlich zur Plaquebildung beitragen kann [32]. Mittels CT-Untersuchungen konnten bei Kalzium-Oxalat-Steinen die früheren apatithaltigen Anwachsstellen eindeutig identifiziert werden [20, 30].

DIAGNOSE DER UROLITHIASIS

Zur Diagnostik von Harnsteinen kommen nicht nur Ultraschall, sondern auch computertomographische- und Röntgenuntersuchungen zum Einsatz. Neben der bildgebenden Diagnostik werden, unabhängig vom Patientenstatus (Kolik, Infekt, temporär schmerzfrei), Laboruntersuchungen von Blut und Urin durchgeführt. Durch eine Analyse der Steinkomposition mittels Infrarotspektroskopie oder Röntgendiffraktomie nach spontanem Steinabgang oder interventioneller Therapie, in Zusammenhang mit den Blut- und Urinmesswerten lässt auf mögliche metabolische, genetische oder infektiöse Ursachen der Steinentstehung rückschließen und die weiteren Therapiemaßnahmen sowie die Metaphylaxe patientenspezifisch gestalten. Die sonografische Untersuchung stellt die Diagnoseapparatur der Wahl für eine schnelle Abschätzung der Symptomatik (Bauchschmerzen, Übelkeit, Erbrechen, ggf. Fieber, selten asymptomatisch) eines Patienten [15, 33]. Durch die Ultraschalluntersuchung können sowohl die Harnblase und die Niere (Kelchsystem, Nierenparenchym) auf pathologische Veränderungen (bspw. Dilatation wegen Flüssigkeitsrückstau) hin untersucht werden, als auch Konkrementen in der Niere, dem distalen und proximalen Harnleiter und der Harnblase erkannt werden. Die Sensitivität und Spezifität werden für Ureter-Steine mit 45 % und 94 %, respektive für Nieren-Steine mit 45 % und 88 %, angegeben [9, 33-35].

Die computertomographische Untersuchung (CT) stellt nach initialer Ultraschalluntersuchung die Methode der Wahl zum Auffinden von Konkrementen und dem pathologischen Zustand, ggf. des gesamten Harnsystems, dar [36, 37]. Durch Zugabe von Kontrastmittel können die Nierenfunktion und die Funktionalität des Harn-Sammelsystems betrachtet werden. Die Sensitivität wird mit 89 % für Konkrementen < 3 mm und 100 % für Konkrementen > 3 mm bei BMI < 30 angegeben. Durch die Einführung von Dual Energy CT Geräten (DECT) kann nicht nur die Konkrementlage, sondern auch die chemische Zusammensetzung ermittelt und visualisiert werden [38-40]. Eventuell kann auch eine Magnet-Resonanz-Tomographie (MRT), obwohl Harnsteine hier nicht bzw. nur extrem schlecht nachzuweisen sind, Aufschlüsse über eine anatomische Obstruktion und den Allgemeinzustand der Harnwege liefern [41, 42]. Insbesondere für Kinder, Jugendliche oder Schwangere wird die MRT- und Sonografie-Untersuchung präferiert, sofern keine unbedingte Indikation für eine CT-Betrachtung besteht, da diese Patientengruppe keinem erhöhten Bestrahlungsrisiko ausgesetzt werden darf [43-47].

THERAPIE DER UROLITHIASIS

Bei akuter Nierenkolik steht die symptomatische Therapie der Schmerzen in Kombination mit einer Entlastung der Harnwege (z. B. Harnleiterschienung) und ggf. eine antiemetische Begleittherapie im Vordergrund. Bei vorherrschendem Harninfekt ist eine antibiotische Behandlung unumgänglich. Eine **konservative Steintherapie** kann nach Anamneseerhebung erfolgen, wenn die Konkrementen kleiner als 5 mm sind und ein spontaner Steinabgang aufgrund der Konkrementlage zu erwarten ist. Zu den konservativen Methoden zählen eine erhöhte Flüssigkeitsaufnahme (Diurese $\geq 2\text{l/d}$), und ggf. Anpassung der Nahrungsgewohnheiten (Reduzierte Eiweißzufuhr, Ansäuerung des Urins durch Fruchtsäfte) [48-51]. Weist eine Steinanalyse auf Harnsäureresteine hin, wird als Kausaltherapie eine orale Chemolitholyse eingeleitet, wodurch der Harn alkalisiert wird und schließlich zur Auflösung des Harnsäuresteins führen kann [52-54]. Unabhängig von der Steinart wird bei der konservativen Steintherapie immer die Flüssigkeitsaufnahme erhöht und vermehrte körperliche Bewegungs- und Entspannungseinheiten empfohlen. Zusätzlich kann der Steinabgang durch Gabe von α -Blockern unterstützt werden [54], eine Überwachung der Risiko-Patienten in definierten Abständen ist erforderlich [55].

Die **operative Steintherapie** findet Anwendung, wenn konservative Maßnahmen fehlgeschlagen haben oder ein zu hohes Risiko (Parenchymatrophie, Hydronephrose, Urosepsis) für den Patienten bei Nichtbehandlung der Obstruktion vorliegt. Neben den nur selten, in Ausnahmefällen durchgeführten, laparoskopischen oder offenen chirurgischen Steinentfernungen, sind drei wesentliche Therapiemöglichkeiten zu nennen: Die extrakorporale Schockwellentherapie (**ESWL**), die perkutane Nephrolitholapaxie (**PCNL**) und die retrograde Ureterorenoskopie (**URS**). Die ESWL ist ein nichtinvasives Verfahren, bei dem der Stein durch außerhalb des Körpers erzeugte und auf den Stein fokussierte Stoßwellen in kleinere Fragmente zertrümmert wird. Die Stoßwellen werden entweder durch elektrohydraulische, elektromagnetische oder piezoelektrische Elemente erzeugt [56-58]. Ziel dieser Behandlung ist es, die Steine in spontan abgangsfähige Konkrementen zu fragmentieren. Eine Harnleiterschienung (DJ-Stent) und α -Blocker-Zugabe kann den spontanen Steinabgang fördern, die Ausbildung einer „Steinstrasse“ reduzieren, wenigstens aber das Harnsystem prophylaktisch entlasten [59-61]. Bei der PCNL erfolgt der Zugang zum Nierenbecken durch perkutane Punktion, wobei die Dilatation des Einstichkanals für die Mini-PCNL maximal 18 Fr beträgt [62]. Der eigentliche Lithotripter ist ein rigides Nephroskop, welches je nach verwendeter Technik dazu im Stande ist den Harnstein elektrohydraulisch, via Ultraschall, pneumatisch oder in einer Kombination (Ultraschall, Pneumatik) dieser Techniken zu fragmentieren. Sofern zugänglich, können Konkrementen unabhängig von Größe und Zusammensetzung mittels PCNL zerkleinert werden. [63-66]. Die URS ist ebenfalls ein minimalinvasives Verfahren mittels flexiblen bei Nierenbecken und semirigiden Endoskopen bei Harnleitersteinen zur Steintherapie [67-69]. Durch die rapiden technologischen Entwicklungen der flexiblen Endoskope (Bildqualität, Flexion, Schaftdurchmesser-Reduktion) werden viele Operationen der Harnwege bei Steinleiden mit URS durchgeführt. Als Goldstandard gilt derzeit die laserinduzierte (Holmium:Yttrium-Aluminum-Garnet Laser) Lithotripsie, wobei gepulstes Laserlicht ($\lambda = 2.1\text{ }\mu\text{m}$) durch eine Glasfaser direkt zur Behandlungsstelle transportiert wird [70-75]. Der **Fragmentierungsprozess** basiert einerseits auf **photothermischer** Schädigung durch die hohe Absorption α von Licht dieser Wellenlänge [76, 77] des im

Stein gebundenen Wassers, welches hierdurch schlagartig verdampft. Durch die physikalisch bedingte Volumenzunahme der gasförmigen Phase, wird enormer mechanischer Stress auf die Struktur des Steins innerhalb der jeweiligen spezifischen Eindringtiefe δ , definiert als der reziproke Wert des Absorptionskoeffizienten, des Laserlichts ausgeübt und führt letztendlich zur Ablation von Steinfragmenten an der Oberfläche des Steins [78-81]. Es gelten folgende Werte für die Absorption α und die Eindringtiefe δ in Wasser [82]: Ho:YAG (λ : 2.1 μm , α : 2.78 mm^{-1} , δ : 0.36 mm). Neben der Energiedisposition im Stein wird Energie in der wässrigen Lösung aus Harn und Spülflüssigkeit an der Behandlungsstelle absorbiert, wodurch Dampfblasen im Medium gebildet werden, welche nach einer von den Lasereinstellungen (Pulslänge, Frequenz, Energie pro Puls) abhängigen Zeit wieder in sich zusammenfallen und dabei Druck- und Stoßwellen auslösen [81]. Dieser **photomechanische** Effekt trägt nur bedingt zur Ablation bei, vielmehr werden instabile Strukturen an der Steinoberfläche, entweder entstanden durch die Laserlichtapplikation oder durch das natürliche Kristallwachstum des Steins, abgetragen. Vornehmlich wird in neueren Ho:YAG-Lasersystemen durch geeignete Laserparameter die Blase als Transit-Tunnel für die Laserstrahlung ausgenutzt, da die Absorption dieser Wellenlänge in Wasserdampf deutlich geringer als in Wasser ist und dadurch die nicht an der Ausbildung der Dampfblase beteiligten Photonen direkt zu Stein geleitet respektive zur Abtragung beitragen können. In der Literatur wurde dieser Effekt unter dem Begriff „Moses-Technologie“ definiert [81, 83]. Einhergehend mit der gewünschten Zerkleinerung des zu behandelten Harnsteins durch das gepulste Laserlicht, erfahren der Stein oder Fragmente davon durch die eingebrachte Energie eine Beschleunigung und werden dadurch von der Faserspitze des Lichtwellenleiters weggestoßen. Dieser Effekt wird in der Literatur **Retropulsion** oder **Propulsion** genannt [84-91].

Durch die Propulsion können Fragmente in schwerer zugängliche oder schlecht einsehbare Bereiche des Urogenital-Traktes befördert werden. Daraus resultiert zum einen eine längere Operationszeit, da der Operateur ein Nachführen des Endoskops einleiten muss, es können aber auch Fragmente übersehen werden. Dadurch kann eine scheinbare Steinfreiheit [92, 93] angenommen werden, obwohl noch potentiell rezidiv-bildende Konkreme im Harnsystem zurückbleiben [94]. Dies wird unter anderem als Erklärung für die hohen Rezidivraten nach fünf Jahren von über 50 % trotz Steinfreiheitsraten (SFR) von bis zu mehr als 90 % für die oben genannten Methoden (SWL, PNL, URS) oder kombinierte Therapieansätze herangezogen [95-98]. Grundsätzlich ist bei der laserinduzierten Lithotripsie durch Anpassung der Laserparameter (optische Pulslänge, Frequenz, Energie pro Puls) eine Variation bis hin zur optimalen Einstellung der Abtragseffizienz und der Propulsion möglich. Insbesondere durch die Vermarktung sogenannter „**Dusting-Settings**“ [81, 93, 99-102] für die Lithotripsie Operation erfolgten technologische Entwicklungen bis hin zu Vierkopf (Ho:YAG) Lasergeräten mit bis zu 120 W mittlerer Leistung [102-105]. Bei der Erzeugung von „**Dust**“ (Fragmente < 1 mm) sollen die Abtragsprodukte direkt über den Spülstrom aus dem Körper befördert werden und dadurch die Zahl potentieller rezidiv-bildender Konkreme reduziert werden. Bei gleichzeitig geringer Propulsion können selbst kleine Fragmente die normalerweise mittels Steinfangkörbchen oder Zangen aus dem Körper entfernt werden, mit dem Laser zerkleinert werden und dadurch die Operationszeit positiv beeinflussen. Nichtsdestotrotz darf die Patientensicherheit gegenüber der Behandlungseffizienz nicht vernachlässigt werden. Durch die eingebrachten hohen mittleren Leistungen von bis zu 120 W sind thermische Schädigungen (Erhitzung des Gemisches aus Harn- und Spülflüssigkeit) des den Behandlungsort umgebenden Gewebes oder durch direkte Lasereinstrahlung möglich [106-110]. Um kollaterale Schädigungen des

umliegenden Gewebes durch Laserstrahlung zu verhindern, wurden Stein-Gewebe-Unterscheidungs-Algorithmen auf Basis der **Fluoreszenzantwort** humaner Steine [111, 112] durch Anregung mittels des Ziellasers (520 nm – 635 nm) entwickelt. Sollte kein Fluoreszenzsignal von einem Stein vor der Faserspitze detektiert werden, wird automatisch der Strahlengang blockiert und es ertönt ein Warnsignal [113]. Zusätzlich wurde eine Methode entwickelt die über Bildverarbeitungs-Algorithmen, basierend auf denen für die Propulsionsbestimmung, die Positionsbestimmung der Faserspitze in Bezug auf das distale Ende des Endoskop-Arbeitskanals ermittelt. Ist die Faser im Arbeitskanal oder zu nahe an der bildgebenden Optik, wird der Strahlengang des Lasers blockiert, um eine potenzielle Schädigung des Endoskops oder schlimmstenfalls des Patienten zu verhindern. Ein ähnliches System zum Schutz des Endoskopes vor ungewollter Laser-Applikation ist in der Literatur zu finden [113]. Neben der Entwicklung von Ho:YAG basierten Lasersystemen wurden zeitgleich auch **Thulium-Faserlaser** ($\lambda = 1.94 \mu\text{m}$) als effiziente und vielversprechende Technologie zur Lithotripsie stetig weiterentwickelt und getestet [114-117]. Durch die im Vergleich zum Ho:YAG-Laser höhere Absorption in Wasser ($\alpha_{\text{Thulium}}: 12.54 \text{ mm}^{-1}$; $\alpha_{\text{Ho:YAG}}: 2.78 \text{ mm}^{-1}$) [76, 77] ist eine schnellere Fragmentierung grundsätzlich möglich [117]. Die bessere Strahlqualität ($M^2 < 1.5$) lässt die Einkoppelung des Lichts in Fasern bis zu $100 \mu\text{m}$ und kleiner zu [81]. Zusätzlich sind Repetitionsraten von bis zu 1 kHz möglich wodurch sich neue Hochfrequenz-Settings ergeben, die vorteilhaft für die Steinbehandlung sein können [81]. Experimente zur Fragmentierungseffizienz, Dusting-Rate und Propulsion mit einem diodengepumpten system ($\lambda = 2.94 \mu\text{m}$) zeigten vielversprechende Ergebnisse. Insbesondere der deutlich höhere Absorptionskoeffizient dieser Wellenlänge in Wasser ($\alpha_{\text{Erbium}}: 1220 \text{ mm}^{-1}$) stellt für die Steintherapie einen vielversprechenden Vorteil dar, allerdings sind derzeitige Faser-Transportsysteme (z.B. Saphir, Hollow-Core) derzeit aufgrund geringer Flexibilität (großer Biegeradius), ihrer thermischen oder mechanischen Stabilität nur beschränkt für endoskopische Anwendungen in einem für die Steintherapie benötigten Leistungsreich sinnvoll zu nutzen.

ORIGINALMANUSKRIPTE

Maximilian Eisel, Stephan Ströbl, Thomas Pongratz, Frank Strittmatter, Ronald Sroka, „*In vitro investigations of propulsion during laser lithotripsy using video tracking*“, Lasers Surg. Med., 50: 333-339. doi:10.1002/lsm.22770 (2018), **JIF**: 2.726

Maximilian Eisel, Stephan Ströbl, Thomas Pongratz, Frank Strittmatter, and Ronald Sroka, „*Holmium:yttrium-aluminum-garnet laser induced lithotripsy: in-vitro investigations on fragmentation, dusting, propulsion and fluorescence*“, Biomed. Opt. Express 9, 5115-5128 (2018), **JIF**: 3.482

Maximilian Eisel, Stephan Ströbl, Thomas Pongratz, Herbert Stepp, Adrian Rühm, Ronald Sroka, "Investigation of optical properties of dissected and homogenized biological tissue", J. Biomed. Opt. 23(9) 091418 (24 September 2018), **JIF**: 2.367

IN VITRO INVESTIGATIONS OF PROPULSION DURING LASER LITHOTRIPSY USING VIDEO TRACKING

Maximilian Eisel, Stephan Ströbl, Thomas Pongratz, Frank Strittmatter, Ronald Sroka, „*In vitro investigations of propulsion during laser lithotripsy using video tracking*“, Lasers Surg. Med., 50: 333-339. doi:10.1002/lsm.22770 (2018), JIF: 2.726

Kurzfassung: Bei der laserinduzierten Lithotripsie wird gepulstes Laserlicht über einen Lichtwellenleiter in einem flexiblen Endoskop zur Behandlungsstelle transportiert und zur Fragmentierung von Konkrementen genutzt [67-69, 71-73]. Die eingebrachte Energie trägt aber nicht nur zur Zerkleinerung des Harnsteines bei, sondern induziert auch eine Bewegung auf den Stein (**Propulsion/Retropulsion**) oder dessen Fragmente [84-91]. Es existieren verschiedene Messapparaturen um die Propulsion bei verschiedenen Laserparametern (optische Pulslänge, Frequenz, Energie pro Puls), meist unter Wasser oder in NaCl-Lösung, zu bestimmen. Ein vielfach zitiertes Set-up ist das **Pendel-Modell**, wobei ein Stein am unteren Ende einer auslenkbaren Befestigung fixiert ist. Bei Laserapplikation wird die Auslenkung über eine oder mehrere Hochgeschwindigkeits-Kameras festgehalten [84, 86, 118]. Eine ähnliche Methode bewertet die **horizontale Bewegung** eines künstlichen Steines nach Laserapplikation durch eine Hochgeschwindigkeits-Kamera oder die insgesamt zurückgelegte Strecke bis der Stein wieder zur Ruhe kommt [88-91]. In einem kürzlich entwickelten Messaufbau wird die **vertikale nach oben** gerichtete Steinbewegung nach Laserapplikation durch einen vertikal von unten eingebrachten Lichtwellenleiter mittels Hochgeschwindigkeits-Kamera-Aufnahmen ausgewertet [83]. Alle dieser Ansätze verwenden zur Bewertung der Propulsion nur einen **Einzelpuls**, bzw. den ersten Puls einer Pulsreihe. Insbesondere der erste Puls entspricht zumeist noch nicht den vom Benutzer eingestellten Parametern, da erst durch Regelung über beispielsweise eine interne Energiemesskarte die endgültigen Pulsenergien und -dauern erreicht werden. Um reproduzierbare experimentelle Bedingungen bei jeder Messung zu garantieren, wurden künstliche würfelförmige Steine (hier: BegoStone, BEGO GmbH & Co. KG, Bremen, Germany) mit einer Kantenlänge von 5 mm zur Evaluation verwendet. Die Härte der Steine wird über das Mischverhältnis von Steinpulver zu Wasser (15:4) eingestellt. Die Härte der hergestellten Steine lag zwischen der von humanen Steinen mit einer Materialkomposition von Calcium-Oxalat-Monohydrat und Magnesium-Ammonium-Phosphat-Hydrogen [84].

Bei dem hier vorgestellten Aufbau zur Messung der Propulsion, wird im Gegensatz zu den oben erwähnten Methoden eine **Serie von Pulsen**, die daraus resultierende Steinbewegung mit einer Hochgeschwindigkeits-Kamera festgehalten. Im Anschluss wird mit einer in MatLab® (MathWorks Corporation, Natick, MA, USA) geschriebenen Software das **Bewegungsprofil** des Steins ausgewertet. Das Steinmodell wird, geführt in einer vertikalen Plexiglasröhre, durch Laserapplikation über eine von unten eingeführte Faser nach oben beschleunigt und fällt aufgrund der entgegengerichteten Schwerkraft wieder zurück in seine Ausgangsposition. Zur Überprüfung der Reproduzierbarkeit der Propulsions-Messungen wurde in einem ersten Setting ($n=5$) nur die Pulslänge (0.3 ms, 0.6 ms, 1.0 ms) bei gleichbleibender Pulsenergie (1 J) und Repetitionsrate (10 Hz) variiert. Um die Messmethode mit früher durchgeführten Pendelversuchen [86] vergleichen zu können, betrug in einem zweiten Setting ($n=15$) die Pulsenergie 0.8 J bzw. 1.2 J bei gleichbleibender Pulslänge (0.3 ms) und Repetitionsrate (10 Hz). Die Auf- und Abbewegung kann über eine Hochgeschwindigkeits-Kamera (1000 fps) in einem Zeitintervall von maximal 7 Sekunden aufgezeichnet werden. Über die Software wird der Rotanteil jedes Bildes herausgefiltert und ein entsprechendes binäres Abbild erzeugt. Der Rotanteil wird verwendet, da Bego-Steine Aufgrund ihres Eisenoxidanteils (ca. 1 %) rötlich erscheinen. Im binären Bild erscheint der Stein weiß und alle umgebenden Elemente schwarz. Durch Schwerpunktsbestimmung der weißen Fläche kann die vertikale Position des Steins für jedes Bild bewertet und als bildweises Bewegungsprofil aufgezeich-

net werden. Durch Bestimmung und Mittelung der Steigung einer jeden aufsteigenden Flanke, respektive der **Geschwindigkeit** des Modell-Steins, kann ein Maß zur Quantifizierung der Propulsion bei unterschiedlichen Laserparametern erzeugt und ausgewertet werden. Die Untersuchungen zeigen, dass die Stärke der Propulsion durch die optische Pulsenergie und die optische Pulslänge beeinflusst werden können. Wird die Pulsenergie bei gleichbleibender Pulslänge erhöht, so zeigt sich eine Erhöhung der Steinbewegung, wird hingegen die Pulslänge bei fester Energie erhöht verringert sich die Propulsion. Durch eine geeignete Kombination aus Pulslänge und Energie können somit Settings erstellt werden, welche eine hohe Abtragsrate bei geringer Propulsion aufweisen.

Der Anteil von Maximilian Eisel an dieser Arbeit war, die Konstruktion und Realisierung eines kompakten Messaufbaus zur Propulsion-Bestimmung und die schriftliche Ausarbeitung. Die Fertigung des Führungsröhrchens, als auch die Planung und Auslegung der Arbeitsabstände zur Hochgeschwindigkeits-Kamera und der Applikationsfaser zum Stein, sowie die störungsfreie Spülwasserversorgung waren ebenfalls Teil dieser Arbeit. Die Programmierung der Bildverarbeitungssoftware in MatLab und des Auswertalgorithmus wurde tatkräftig durch Herrn Stephan Ströbl als Teil seiner Masterarbeit unterstützt. Der gesamte Messaufbau wurde als Gebrauchsmuster beim Deutschen Patent- und Markenamt (Aktenzeichen 20 2017 002 293.1) angemeldet.

In Vitro Investigations of Propulsion During Laser Lithotripsy Using Video Tracking

Maximilian Eisel,^{1,2*} Stephan Ströbl,^{1,2} Thomas Pongratz,^{1,2} Frank Strittmatter,² and Ronald Sroka^{1,2}

¹Laser-Forschungslabor, LIFE-Zentrum, University Hospital of Munich, Munich, Germany

²Department of Urology, University Hospital of Munich, Munich, Germany

Objectives: Ureteroscopic laser lithotripsy is an important and widely used method for destroying ureter stones. It represents an alternative to ultrasonic and pneumatic lithotripsy techniques. Although these techniques have been thoroughly investigated, the influence of some physical parameters that may be relevant to further improve the treatment results is not fully understood. One crucial topic is the propulsive stone movement induced by the applied laser pulses. To simplify and speed up the optimization of laser parameters in this regard, a video tracking method was developed in connection with a vertical column setup that allows recording and subsequently analyzing the propulsive stone movement in dependence of different laser parameters in a particularly convenient and fast manner.

Materials and Methods: Pulsed laser light was applied from below to a cubic BegoStone phantom loosely guided within a vertical column setup. The video tracking method uses an algorithm to determine the vertical stone position in each frame of the recorded scene. The time-dependence of the vertical stone position is characterized by an irregular series of peaks. By analyzing the slopes of the peaks in this signal it was possible to determine the mean upward stone velocity for a whole pulse train and to compare it for different laser settings. For a proof of principle of the video tracking method, a specific pulse energy setting (1 J/pulse) was used in combination with three different pulse durations: short pulse (0.3 ms), medium pulse (0.6 ms), and long pulse (1.0 ms). The three pulse durations were compared in terms of their influence on the propulsive stone movement in terms of upward velocity. Furthermore, the propulsions induced by two different pulse energy settings (0.8 J/pulse and 1.2 J/pulse) for a fixed pulse duration (0.3 ms) were compared. A pulse repetition rate of 10 Hz was chosen for all experiments, and for each laser setting, the experiment was repeated on 15 different freshly prepared stones. The latter set of experiments was compared with the results of previous propulsion measurements performed with a pendulum setup.

Results: For a fixed pulse energy (1 J/pulse), the mean upward propulsion velocity increased (from 120.0 to 154.9 mm · s⁻¹) with decreasing pulse duration. For fixed pulse duration (0.3 ms), the mean upward propulsion velocity increased (from 91.9 to 123.3 mm · s⁻¹) with increasing pulse energy (0.8 J/pulse and 1.2 J/pulse). The latter result corresponds roughly to the one obtained with

the pendulum setup (increase from 61 to 105 mm · s⁻¹). While the mean propulsion velocities for the two different pulse energies were found to differ significantly ($P < 0.001$) for the two experimental and analysis methods, the standard deviations of the measured mean propulsion velocities were considerably smaller in case of the vertical column method with video tracking (12% and 15% for $n = 15$ freshly prepared stones) than in case of the pendulum method (26% and 41% for $n = 50$ freshly prepared stones), in spite of the considerably smaller number of experiment repetitions ("sample size") in the first case.

Conclusion: The proposed vertical column method with video tracking appears advantageous compared to the pendulum method in terms of the statistical significance of the obtained results. This may partly be understood by the fact that the entire motion of the stones contributes to the data analysis, rather than just their maximum distance from the initial position. The key difference is, however, that the pendulum method involves only one single laser pulse in each experiment run, which renders this method rather tedious to perform. Furthermore, the video tracking method appears much better suited to model a clinical lithotripsy intervention that utilizes longer series of laser pulses at higher repetition rates. The proposed video tracking method can conveniently and quickly deliver results for a large number of laser pulses that can easily be averaged. An optimization of laser settings to achieve minimal propulsive stone movement should thus be more easily feasible with the video tracking method in connection with the vertical column setup. Lasers Surg. Med. © 2017 Wiley Periodicals, Inc.

Key words: laser lithotripsy; propulsion; retropulsion; video tracking; urology; Ho:YAG laser

Conflicts of Interest Disclosures: All authors have completed and submitted the ICMJE Form for Disclosure of Potential Conflicts of Interest and none were reported.

This manuscript is part of the inaugural thesis of Maximilian Eisel to be submitted at the Medical Faculty of the Ludwig-Maximilians-Universität, Munich.

*Correspondence to: Maximilian Eisel, MSc, Laser-Forschungslabor, LIFE-Zentrum, University Hospital of Munich, Munich, Möslweg, 482399 Raisting, Germany.

E-mail: max.eisel@med.uni-muenchen.de

Accepted 11 November 2017

Published online in Wiley Online Library

(wileyonlinelibrary.com).

DOI 10.1002/lsm.22770

INTRODUCTION

During ureteroscopic laser lithotripsy [1–3], laser pulses are applied to the stone to be fragmented in a stochastic manner, yet preferentially in direct or close contact between application fiber and stone surface in the moment of laser impact [4]. Besides the desired fragmentation process, the applied laser pulses also induce a propulsive movement of the stone, which can prolong the required treatment time due to the necessity of stone chasing and the possibility of losing stone fragments [5]. The resulting incomplete stone clearance could be one of the major reasons for recurrence [6–8].

In recent investigations, a number of setups were developed to investigate and to quantify the unwanted propulsive effect during stone fragmentation. All these experiments are performed in water or saline solution [7,9–13].

By means of the well-known pendulum method [9,12,13], the stone movement due to laser impact can be quantified *via* the maximum deflection angle of the pendulum. With the stone in neutral position, the distal fiber end is arranged horizontally and in contact to the stone's surface. The pendulum's deviation following the first emitted laser pulse is then observed by a high speed camera, which is positioned perpendicular to the oscillation plane.

A similar approach is based on the measurement of the horizontal movement of stones guided by a tube or rim [7,8,10,11]. Light pulses are applied through an optical fiber in the same way as in case of the pendulum setup, and it is again only the first laser pulse that determines the movement of the stone. The movement is observed by a camera system and/or the total moved distance is determined to quantify the propulsive stone movement.

A further, recently developed experimental method uses the observation of the vertical motion of a stone *via* a high speed camera, followed by a frame-by-frame evaluation of the recorded video sequence [14]. The laser pulses are applied through a vertically oriented optical fiber guided to the stone from the bottom. Upon laser activity, the stone is driven upward and falling back due to gravity.

All three approaches share the disadvantage that the analyzed movement originates from only one single laser pulse, in fact the first one if a series of pulses is applied. The intensity and duration of the first laser pulse, however, can usually not be specified or defined, especially in the case of medical laser systems.

To overcome such problems and to carry out reproducible experiments for comparing laser lithotripsy devices for medical use, a method for quantitative and reproducible measurement of the propulsion movement was developed. Such experiments are prerequisites to identify laser emission parameters with which the propulsion can be reduced to a minimum.

MATERIALS AND METHODS

Experimental Setup

To guarantee reproducible experimental conditions, real human stones are hardly suitable, as they strongly vary in

composition, structure, and surface roughness. Therefore, an artificial stone model was used, comprising cubical stones (edge length: 5 mm) manufactured from plaster (BegoStone, BEGO GmbH & Co. KG, Bremen, Germany) with a compound-to-water ratio of 15:4, leading to mechanical stone properties comparable to in-vivo ureter stones, ranging between those of COM (calcium oxalate monohydrate) and MAPH (magnesium ammonium phosphate hydrogen) urinary stones [9]. The mean mass of the stone phantoms used was $(0.215 \pm 0.015 \text{ g})$.

As sketched in Figure 1, the artificial stone was put into a wide bore hole ($\varnothing = 9 \text{ mm}$, depth = 40 mm) drilled from above into an acrylic glass bar ($\varnothing = 25 \text{ mm}$, $h = 50 \text{ mm}$). The light-guiding fiber ($\varnothing_{\text{core}}$: 365 μm , $\varnothing_{\text{outer}}$: 600 μm) was inserted into the so-formed test chamber through a narrow bore hole ($\varnothing = 2.3 \text{ mm}$) from the bottom.

In addition, horizontal holes ($\varnothing = 6 \text{ mm}$) were drilled into the glass bar near the top to establish a water flow system ensuring a clear view as small dust particles created during laser light application were rinsed away. The flowrate was set to 150 ml/min during the experiments. Here, dust is defined by a fragment size below 1 mm, while bigger fragments are counted as fragments [15]. To ensure reproducible conditions at the start of each experiment, the initial distance between distal fiber end and stone surface was adjusted to $(2.0 \pm 0.1 \text{ mm})$. This distance value was empirically found to be well suited as it yielded largely reproducible average stone movements in all performed experiments. Upon laser activity, the distance between stone surface and fiber tip changes more or less periodically due to acceleration by the laser pulses and gravity as a counteracting force that let the stone fall back roughly into its initial position. Details of this roughly periodic stone movement depend on the selected laser settings.

A Ho:YAG laser device (Auriga, StarMedTec, Starnberg, Germany) was used to generate pulsed laser light at a wavelength of 2.1 μm . The laser settings could be varied in

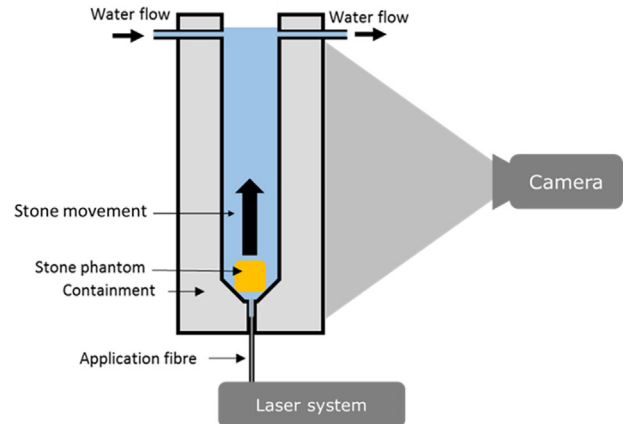


Fig. 1. Experimental setup for the propulsion measurement. The acrylic glass tube is used as a sample chamber, the laser pulses are applied from the bottom *via* an optical fiber. The resulting stone phantom movement is recorded by a camera system.

terms of pulse duration, pulse energy, and repetition rate. The laser settings used for propulsion measurements are listed in Table 1.

During laser pulse application, the stone movement was recorded in the form of an RGB movie by means of a digital camera (DSC RX-100 V, Sony, Tokyo, Japan) with a frame rate of 1,000 fps. The recording time was limited to 7 seconds by the internal buffering capacity.

Video Tracking Software

The recorded video files were analyzed with a homemade video tracking software for use with MatLab[®] (MathWorks Corporation, Natick, MA). The analysis was performed solely on the red channel of the video sequence, because the BegoStone phantom material contains about 1% of red iron oxide, providing a high contrast between stone and background in that colour channel. The RGB video file was split into single frames, from which the red color channel was extracted as an 8 bit brightness image. Pixels were assigned to the stone only if their brightness value and those of the eight surrounding pixels exceeded a certain threshold value. Thereby, it is prevented that isolated red pixels are attributed to the stone and included in the stone position analysis, which would falsify the result. The threshold was set to 2/3 of the maximum possible intensity value 255. This value was empirically found to be well suited to ensure that a variation in illumination had practically no effect on the obtained stone position. The subset of pixels attributed to the stone was surrounded by the corresponding minimum-size rectangle for illustration purposes, as shown in Figure 2 left. The right panel of Figure 2 shows a corresponding binary (i.e., black-and-white) image where the pixels attributed to the stone are white while all others are black. The centroid position of the white area is calculated and indicated by a small cross in the left image of Figure 2 and used to determine the y-position of the stone

The (vertical) y-coordinate of the centroid position was determined for each frame and plotted as a function of the frame number as shown in Figure 3. To quantify the laser pulse impact on the stone, the mean upward propulsion

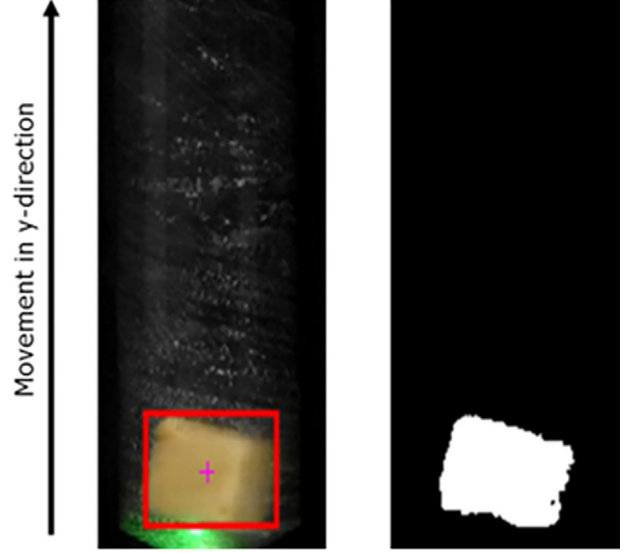


Fig. 2. Tracking of the stone's centroid position based on threshold-exceeding pixels in the red channel of one frame of the recorded video sequence (left). Only the threshold-exceeding pixels are associated with the stone and represented in a binary black-and-white image (right).

velocity of the stone was determined from the slopes of the rising flanks of all sufficiently high peaks in the graph. An empirically developed numerical flank detection filter was used to identify the rising flanks of the laser-induced stone movement: Each y-value gets compared to the y-value recorded 10 frames later. As long as the latter y-value is bigger, the slope of the connection line between the two data points is positive. Each series of subsequent y-values fulfilling this condition was interpreted as a rising flank. The data points with the lowest and the highest y-values within each rising flank,

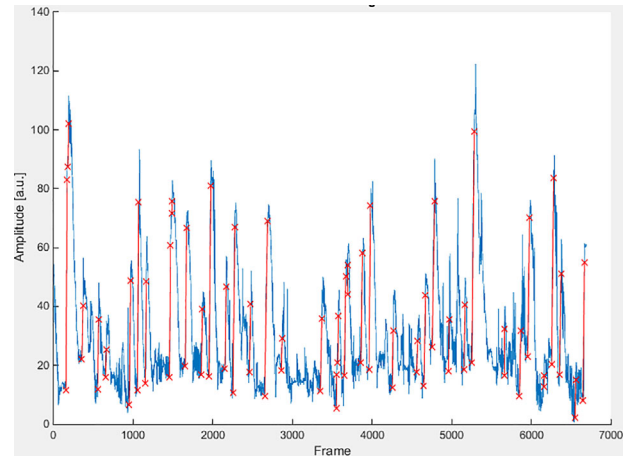


Fig. 3. Vertical centroid coordinate observed during stone movement as a function of the frame number (7,000 frames were recorded at 1,000 fps over 7 s recording time).

TABLE 1. Laser Settings Used for Reproducibility Testing of the Vertical Column Method With Video Tracking and for Comparison to Former Pendulum Measurements. The last column contains the number of independent experiments performed in each case

	E_{pulse} (J)	f_{rep} (Hz)	t_{pulse} (ms)	n
Reproducibility testing	1.0	10	0.3	5
	1.0	10	0.6	5
	1.0	10	1.0	5
Setup comparison	0.8	10	0.3	15
	1.2	10	0.3	15

(t_{\min}, y_{\min}) and (t_{\max}, y_{\max}) , were then used to calculate the flank's slope as the upward-velocity

$$v = \frac{\Delta y}{\Delta t} = \frac{y_{\max} - y_{\min}}{t_{\max} - t_{\min}}$$

Two kinds of experiments were performed: A reproducibility test of the vertical column setup with video tracking and comparison experiments to further investigate this method in terms of potential improvements in comparison to the well-established pendulum setup [12]. In Table 1, the experimental parameters and the numbers of performed independent experiments are listed.

Statistical Evaluation

Based on the slopes of the rising flanks, the velocities of every upward-movement were calculated and afterwards averaged. Hence, for every 7-second video sequence, a mean upward propulsion velocity value v_{mean} was obtained. These v_{mean} values were statistically compared for different laser settings based on significance t -tests ($P < 0.05$, significance level) performed with the statistical software SigmaPlot (V.11.0, Systat Software GmbH, Erkrath, Germany). The obtained propulsion velocities are plotted with the corresponding standard errors in case of the reproducibility test and with the corresponding standard deviations in case of the pendulum setup.

RESULTS

In Figure 4 the results of the reproducibility tests (left: experiment 1, right: experiment 2) performed at a fixed pulse energy of 1 J/pulse and a fixed repetition rate of 10 Hz are shown for different pulse durations: short pulses (0.3 ms), medium pulses (0.6 ms), and long pulses (1.0 ms).

The mean values and the standard errors of the upward propulsion velocity are illustrated as obtained in five

independent experiment repetitions. For long pulses (experiment 1: $(120.0 \pm 2.9 \text{ mm} \cdot \text{s}^{-1})$, experiment 2: $(128.3 \pm 6.9 \text{ mm} \cdot \text{s}^{-1})$, the mean upward propulsion velocity is significantly lower in comparison to short pulses (experiment 1: $[154.9 \pm 5.8 \text{ mm} \cdot \text{s}^{-1}]$, experiment 2: $[168.5 \pm 5.4 \text{ mm} \cdot \text{s}^{-1}]$). The result for medium pulse duration is also significantly different from that for long pulse duration (experiment 1: $[143.8 \pm 7.8 \text{ mm} \cdot \text{s}^{-1}]$, experiment 2: $[149.9 \pm 2.7 \text{ mm} \cdot \text{s}^{-1}]$). There was no statistical difference between short pulse and medium pulse ($P = 0.287$) in experiment 1, but in experiment 2 the difference was significant ($P = 0.015$), which can be traced back to the small sample size ($n = 5$ experiment repetitions). Furthermore, no significant difference between the mean upward propulsion velocities obtained in the two experiments was found, neither for short pulses ($P = 0.123$), medium pulses ($P = 0.487$), and long pulses ($P = 0.301$). Overall it could be shown that propulsion measurements with the employed experimental and analysis methods yielded reproducible results for the investigated stone phantoms and laser settings.

In a second set of propulsion velocity measurements, a comparison with former pendulum measurements was performed, employing pulse energies of 0.8 and 1.2 J and a fixed pulse duration of 0.3 ms. The experiments just differed in the employed pulse repetition rate, which was 3 Hz in case of the pendulum setup and 10 Hz in case of the vertical column method with video tracking. As in pendulum measurements only the first laser pulse contributes to the stone propulsion, the repetition rate is irrelevant in this. In Figure 5, the mean values and the standard deviations of the vertical propulsion velocities induced by two different pulse energies in 15 experiment repetitions are compared for the vertical column setup with video tracking and the pendulum setup [12].

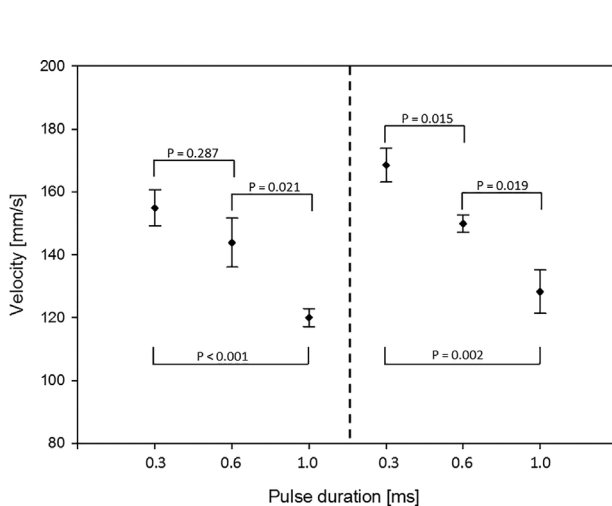


Fig. 4. Results obtained during the reproducibility test of the vertical column method with video tracking (left: experiment 1, right: experiment 2). Laser parameters: 1J-10 Hz, short pulse (0.3 ms), medium pulse (0.6 ms), long pulse (1.0 ms). ($n = 5$ experiment repetitions, t -test performed using SigmaPlot 11.0).

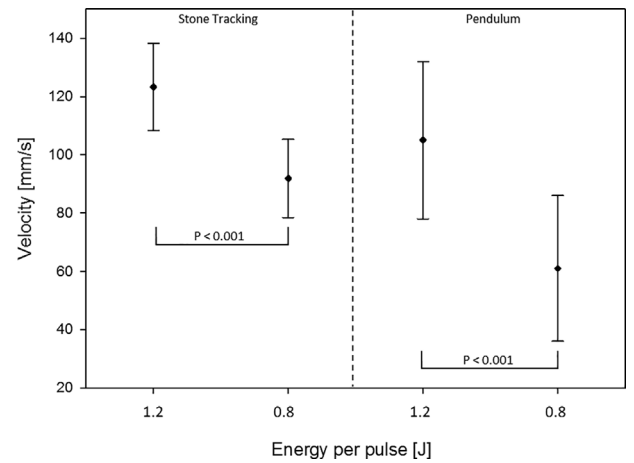


Fig. 5. Comparison of the laser-induced stone phantom propulsion velocities obtained with the vertical column method with video tracking software and previously published results obtained with a pendulum setup [11] for identical laser settings. The mean propulsion velocities and their standard deviations are illustrated, t -tests ($P < 0.001$) were performed to test if differences between the obtained results are statistically significant.

With both methods the two different laser settings can be distinguished with regard to the laser-induced stone movement with high significance ($P < 0.001$). It is obvious, however, that the errors bars are larger in the data obtained with the pendulum setup despite the corresponding large sample size of $n = 50$ (single-pulse) measurements [12], while for the tracking method the sample size was $n = 15$ (number of video sequences). For fixed pulse duration (0.3 ms), both methods yielded, expectedly, higher propulsion velocities when using a higher pulse energy of 1.2 J/pulse (vertical column with video tracking: $(123.3 \pm 15.0 \text{ mm} \cdot \text{s}^{-1}) (\pm 12\%)$, pendulum: $(105 \pm 27 \text{ mm} \cdot \text{s}^{-1}) (\pm 26\%)$, while for 0.8 J/pulse the propulsion velocities were lower (vertical column with video tracking: $(91.9 \pm 13.4 \text{ mm} \cdot \text{s}^{-1}) (\pm 15\%)$, pendulum: $(61 \pm 25 \text{ mm} \cdot \text{s}^{-1}) (\pm 41\%)$).

DISCUSSION

The vertical column-based propulsion measurement setup with video tracking analysis was developed to investigate the stone propulsion effect of medical laser systems and their specific parameter settings in a convenient manner and with improved reproducibility compared to existing alternative methods. Based on the results of the performed experiments, employing the proposed method in combination with reproducible fragmentation experiments should allow to explore useful laser parameters for clinical laser application in lithotripsy more easily than in the past [5]. Clearly, the described method so far pertains only to the characterization of the propulsive stone movement and not to the investigation of fragmentation mechanisms. However, the proposed method could certainly be combined with such investigations. Besides the optimisation of the fragmentation process the safety of the patient during the treatment should be taken into account. An interesting approach was recently published [16], where the fluorescence light of human calculi excited by the aiming beam (532 nm) was used to differentiate between ureteral tissue and stone. This signal could be used to implement a feedback loop preventing the laser being fired accidental on ureteral tissue.

It could be shown that, despite the considerable differences between the vertical column setup and the pendulum setup, the observed dependencies of the propulsion values on the laser settings were in general well comparable. The results are well consistent with the findings of other groups, for example, with regard to the observation of higher propulsion velocities in the case of shorter pulse durations [17–23].

Influences of the water flow on the observed propulsive stone movements can be neglected as the flow rate could be set to the same flow rate for each measurement. Hence, it is assumed that the water turbulences were similar in different measurements.

Apart from the generation of dust, the continuously induced fragmentation of the stone phantom represents a further limitation of the vertical column setup, in

particular for long observation times. Fragmentation could already become of major concern once material ablation leads to a non-negligible change of the stone's mass. In the experiments reported here, ablation of stone material was neglected. For more detailed investigations it is recommendable to check if this is fully justified, that is, whether ablation during the observation time (here 7-seconds) has no influence to the obtained results.

In comparison to the pendulum setup and similar approaches, the method for propulsion measurements proposed here largely facilitates investigating the average laser impact during a longer series of laser pulses. The pendulum method is sensitive only to the stone propulsion induced by a single laser pulse, and, at least in the case of existing laser devices built for medical use, the only relevant pulse has so far always been the first pulse in a series of laser pulses, which is particularly undesirable if that first laser pulse is for technical reasons not yet equivalent to the average pulse within the subsequent pulse series.

As the vertical column method with video tracking allows for the measuring the effects of multiple consecutive pulses, it becomes fairly easy to average these effects over a high number of pulses. The limiting factor for the number of pulses is the maximum recording time of the camera system, for example, in this case 7 seconds, as determined by the limited buffering capacity.

The vertical column method with video tracking has the advantage that it strongly facilitates the analysis of the impact of a large number of laser pulses on the propulsive stone movement, for example, in terms of the mean upward propulsion velocity of a stone phantom. The setup was optimized to create reproducible results under (at least statistically) identical conditions for each experiment in a series of experiment repetitions. As the vertical column setup is a hands-free device, the influence of an operator is largely excluded or at least restricted to the initial fiber positioning and the flow rate adjustment. The first not yet energy-stabilized pulses in a longer series of pulses have no influence on the measurement results, as the recording of the stone movement may be started some time (1 second in the present case) after starting the pulse sequence. For the same reason, the initial stone positioning has no influence on the results. Most of the advantages summarized here are based on the guidance of the stone within the acrylic glass vessel, in combination with the effect of gravity. As a result, it was possible to obtain a high result reproducibility despite the small number of experiment repetitions.

As usual, the immediate translation of the reported experimental results into clinical considerations are impeded by the fact that in the reported experiments standard BegoStone phantoms of rather well-defined size, mass, and other physical properties [24] were used in a highly simplified artificial ureter model (bore hole in PMMA). It was not the aim of this study to very realistically imitate clinical situations, but rather to gain

reproducible results from a standardized measurement setup which can then be used to optimize medical laser devices for optimal clinical benefit, that is, an optimal relationship between minimal stone propulsion and maximum fragmentation efficacy. Clinical stones are of different composition and structure, highly patient-specific, and they vary in size and mass. Thus the impact of laser parameters may be different from those reported here [25]. Also, the reproducibility will be lower in case of real clinical stones due to their largely varying material properties.

In the reported experiments, cubical stone phantoms were used, which may be regarded as a drawback due to considerably different properties with regard to flow in fluids in comparison to spherical phantoms. The effect of the shape of the used phantoms should be investigated in future experiments. In the experiments reported here, the influence of fluid dynamics has not been discussed. However, since the environmental conditions were identical in every measurement, it was easily possible to obtain reproducible results.

For the available camera frame rate of 1,000 fps, it was not possible to resolve the stone acceleration process during the laser pulse impact phase directly, because the pulse duration was 1 ms or shorter in all conducted experiments. Stone observation during the acceleration phase would certainly be of considerable interest in order to determine the laser-induced force applied to the stone.

The described setup and evaluation method appear suitable and promising to test and compare different commercially available laser systems and their emission parameters with regard to their propulsion effect in a hands-free and reproducible manner. The fragmentation and dusting efficiency has to be investigated separately or potentially in parallel with a refined setup and in regard to recent findings of other groups investigating different fragmentation methods [26]. To gain a broader overview and deeper insight into the mechanisms determining the propulsion effect during lithotripsy, a larger number of laser settings, as well as several different laser sources should be investigated. The mass loss of the stone phantom due to ablation should be taken into account, and it should be investigated whether the time-dependent ablation observed during a few seconds of laser application might potentially be sufficient to predict the macroscopic mass loss expectable over longer treatment times. This will be part of an upcoming experimental study in the near future.

CONCLUSION

A video tracking method for objectively determining the propulsive movement of artificial stones during laser lithotripsy was developed. The stone tracking method allows for a more exact quantification of the laser pulse induced movement and thus the underlying physical processes and mechanisms. By recording and analyzing the stone movement over time, the mean upward propulsion velocity could be determined for single laser pulses

and compared for different laser settings. This method provides a robust and simple approach for the optimization of laser parameters, such as pulse duration, repetition rate, and pulse energy, in order to achieve an optimal combination of low stone propulsion and high fragmentation efficacy, which can then be evaluated in a clinical setting.

REFERENCES

1. Dretler SP. Laser lithotripsy: A review of 20 years of research and clinical applications. *Lasers Surg Med* 1988;8(4): 341–356.
2. Hofstetter A. Lasers in urology. *Lasers Surg Med* 1986;6(4):412–414.
3. Vogel A. Nonlinear absorption: Intraocular microsurgery and laser lithotripsy. *Phys Med Biol* 1997;42(5):895–912.
4. Papatsoris AG, Skolarikos A, Buchholz N. Intracorporeal laser lithotripsy. *Arab J Urol* 2012;10(3):301–306.
5. Kronenberg P, Traxer O. Update on lasers in urology 2014: Current assessment on holmium: Yttrium-aluminum-garnet (Ho:YAG) laser lithotripter settings and laser fibers. *World J Urol* 2015;33(4):463–469.
6. Dretler SP. Ureterscopy for proximal ureteral calculi: Prevention of stone migration. *J Endourol* 2000;14(7): 565–567.
7. Lee HO, Ryan RT, Teichman JMH, et al. Stone retropulsion during holmium: Yag lithotripsy. *J Urol* 2003;169(3):881–885.
8. Sofer M, Watterson JD, Wollin TA, Nott L, Razvi H, Denstedt JD. Holmium: YAG laser lithotripsy for upper urinary tract calculi in 598 patients. *J Urol* 2002;167(1):31–34.
9. Hutchens TC, Gonzalez DA, Irby PB, Fried NM. Fiber optic muzzle brake tip for reducing fiber burnback and stone retropulsion during thulium fiber laser lithotripsy. *J Biomed Optics* 2017;22(1):018001.
10. Kang HW, Lee H, Teichman JMH, Oh J, Kim J, Welch AJ. Dependence of calculus retropulsion on pulse duration during HO: YAG laser lithotripsy. *Lasers Surg Med* 2006;38(8): 762–772.
11. Sea J, Jonat LM, Chew BH, et al. Optimal power settings for holmium: YAG lithotripsy. *J Urol* 2012;187(3):914–919.
12. Sroka R, Haseke N, Pongratz T, et al. In vitro investigations of repulsion during laser lithotripsy using a pendulum set-up. *Lasers Med Sci* 2012;27(3):637–643.
13. Wollin DA, Ackerman A, Yang C, et al. Variable pulse duration from a new holmium:YAG laser: The effect on stone comminution, fiber tip degradation, and retropulsion in a dusting model. *Urology* 2017;103:47–51.
14. Elhilali MM, Badaan S, Ibrahim A, Andonian S. Use of the moles technology to improve holmium laser lithotripsy outcomes: A preclinical study. *J Endourol* 2017;31(6): 598–604.
15. Bader MJ, Pongratz T, Khoder W, et al. Impact of pulse duration on Ho: YAG laser lithotripsy: Fragmentation and dusting performance. *World J Urol* 2015;33(4):471–477.
16. Lange B, Jocham D, Brinkmann R, Cordes J. Stone/tissue differentiation for holmium laser lithotripsy using autofluorescence: Clinical proof of concept study. *Lasers Surg Med* 2017;49(4):361–365.
17. Defidio L, De Dominicis M, Di Gianfrancesco L, Fuchs G, Patel A. Improving flexible ureterorenoscope durability up to 100 procedures. *J Endourol* 2012;26(10):1329–1334.
18. Finley DS, Petersen J, Abdelshehid C, et al. Effect of holmium: YAG laser pulse width on lithotripsy retropulsion in vitro. *J Endourol* 2005;19(8):1041–1044.
19. Marguet CG, Sung JC, Springhart WP, et al. In vitro comparison of stone retropulsion and fragmentation of the frequency doubled, double pulse nd: YAG laser and the holmium: YAG laser. *J Urol* 2005;173(5):1797–1800.
20. Gupta PK. Is the holmium:YAG laser the best intracorporeal lithotripter for the ureter? A 3-year retrospective study. *J Endourol* 2007;21(3):305–309.

21. Bell JR, Penniston KL, Nakada SY. In vitro comparison of stone fragmentation when using various settings with modern variable pulse holmium lasers. *J Endourol* 2017; 31(10): 1067–1072.
22. Kamal W, Kallidonis P, Koukiou G, et al. Stone retropulsion with Ho: YAG and Tm: YAG lasers: A clinical practice-oriented experimental study. *J Endourol* 2016;30(11): 1145–1149.
23. Li R, Ruckle D, Keheila M, et al. High-frequency dusting versus conventional holmium laser lithotripsy for intrarenal and ureteral calculi. *J Endourol* 2017;31(3):272–277.
24. Liu Y, Zhong P. BegoStone—A new stone phantom for shock wave lithotripsy research (L). *J Acoust Soc Am* 2002;112(4): 1265–1268.
25. Teichman JM, Vassar GJ, Glickman RD. Holmium: Yttrium-aluminum-garnet lithotripsy efficiency varies with stone composition. *Urology* 1998;52(3):392–397.
26. Klaver P, de Boorder T, Rem AI, Lock T, Noordmans HJ. In vitro comparison of renal stone laser treatment using fragmentation and popcorn technique. *Lasers Surg Med* 2017;49(7):698–704.

HOLMIUM:YTTRIUM-ALUMINUM-GARNET LASER INDUCED LITHOTRIPSY: IN-VITRO INVESTIGATIONS ON FRAGMENTATION, DUSTING, PROPULSION AND FLUORESCENCE

Maximilian Eisel, Stephan Ströbl, Thomas Pongratz, Frank Strittmatter, and Ronald Sroka, „*Holmium:yttrium-aluminum-garnet laser induced lithotripsy: in-vitro investigations on fragmentation, dusting, propulsion and fluorescence*“, Biomed. Opt. Express 9, 5115-5128 (2018), **JIF**: 3.482

Kurzfassung: Anhand einer Variation von Laserparametern, einer Kombination aus optischer Pulslänge, Repetitionsrate und Energie pro Puls, wurden die Fragmentierungseigenschaften und die jeweils induzierte Propulsion untersucht. Des Weiteren wurden die Fluoreszenzeigenschaften von humanen Nierensteinen mittels spektraler Fluoreszenzmikroskopie bei unterschiedlichen Anregungswellenlängen betrachtet. Für die Versuche wurde ein experimenteller Ho:YAG-Laser verwendet, welcher eine weite Variation an Parametern bereitstellte (Pulslängen bis zu 4 ms, Repetitionsraten bis 80 Hz und Energien pro Puls bis 2.5 J). Die verwendeten Laserparameter wurden aufgrund früherer Experimente, sowie derzeit in der Literatur publizierter Settings entsprechend ausgewählt [83, 86, 100, 119-121].

Für die **Fragmentierungs**-Experimente wurden würfelförmige Bego-Steine (Kantenlänge 5 mm, Mischverhältnis 15:4) [120] in einem unter Wasser befindlichen Plexiglasbehälter durch Laserapplikation von einer von oben eingeführten Faser ($\varnothing_{\text{Kern}}$ 365 μm) zerkleinert. Die Zeit bis alle Fragmente klein genug waren, um die im Boden befindlichen Löcher (\varnothing : 2.3 mm) zu passieren, wurde als Gesamtzeit (t_{tot}) für die Laserbehandlung gewertet. Zusätzlich wurde die Zeit des ersten Auseinanderbrechens (t_{break}) des künstlichen Steins genommen. Der Anteil des erzeugten „Dusts“ (Fragmente < 1 mm) [119] wurde durch vorheriges Wiegen der Steingesamtmasse gegenüber dem Fragmentgewicht (Fragmentgröße > 1 mm) nach der Laserapplikation errechnet. Die Laserparameter wurden dann anhand der aufgenommenen Applikationszeiten und dem erzeugten Dust-Anteil bewertet.

Die **Propulsion** wurde mit dem in [120] beschriebenen Messaufbau durch Analyse der mit einer Hochgeschwindigkeits-Kamera (1000 fps) aufgenommenen Bewegungsprofile ausgewertet. Das Set-up wurde für die Verwendung von kugelförmigen künstlichen Steinen (\varnothing : 6 mm) optimiert. Durch die Verwendung von sphärischen Steinen konnten deutliche Verbesserungen der Bewegungsprofile erzeugt werden, da sich diese im Gegensatz zu den würfelförmigen Steinen nicht sporadisch verkeilten und dadurch teils nicht zu bewertende Abschnitte im Profil erzeugten.

Durch spektrale **Fluoreszenz**-Mikroskopie (Anregungswellenlängen: 400 nm, 450 nm, 550 nm) konnte die breitbandige Fluoreszenzantwort (470 nm – 750 nm), je nach verwendetem Langpassfilter, von humanen Nierensteinen exemplarisch dargestellt werden. Während einer Operation konnte die Fluoreszenzantwort humaner Nierensteine ($\lambda_{\text{det.}} > 610 \text{ nm}$) nach Anregung im grünen Wellenlängenbereich ($\lambda_{\text{exc.}}$ 500-570 nm) gezeigt werden.

Die Untersuchungen zeigten, dass Settings mit einer Pulslänge von mehr als 1 ms, bei gleichzeitiger Erhöhung der Pulsenergie- und Repetitionsraten (>30 Hz), einen vielversprechenden Ansatz für die effiziente Steinzerkleinerung darstellen. Bei den Propulsionsexperimenten wurden die kubischen Steine durch sphärische ersetzt, dies führte zu einer deutlich besseren **Reproduzierbarkeit** der Ergebnisse durch die besseren Strömungseigenschaften der kugelförmigen künstlichen Steine. Die Fluoreszenzantwort von humanen Nierensteinen kann für die Auffindung von Steinfragmenten oder für **Sicherheitssysteme** zum Patienten- und Komponentenschutz genutzt werden.

Der Anteil von Maximilian Eisel an dieser Arbeit war die Erstellung bzw. Weiterentwicklung eines Messaufbaus zur Bestimmung der Fragmentierungseffizienz und Propulsion bei Laserapplikation auf ein Steinmodell, die Durchführung der Messreihen (Propulsion, Fragmentierung, Fluoreszenz) und das Zusammenfassen der erhaltenen Daten in einer Publikation. Eine mit Herrn Stephan Ströbl am Labor entwickelte *Vorrichtung zum Schutz endoskopischer Komponenten vor ungewollter Laserapplikation*, basierend auf dem bei der Propulsion verwendeten Farndetektionsalgorithmus, wurde als Gebrauchsmuster beim Deutschen Patent- und Markenamt angemeldet (Aktenzeichen 20 2017 003 565.0).



Holmium:yttrium-aluminum-garnet laser induced lithotripsy: in-vitro investigations on fragmentation, dusting, propulsion and fluorescence

MAXIMILIAN EISEL,^{1,2,*} STEPHAN STRÖBL,^{1,2} THOMAS PONGRATZ,^{1,2} FRANK STRITTMATTER,² AND RONALD SROKA^{1,2}

¹Laser-Forschungslabor, LIFE-Zentrum, University Hospital of Munich, Munich, Germany

²Department of Urology, University Hospital of Munich, Munich, Germany

*Max.Eisel@med.uni-muenchen.de

Abstract: The fragmentation efficiency on Bego artificial stones during lithotripsy and the propulsive effect (via video tracking) was investigated for a variety of laser settings. A variation of the laser settings (pulse energy, pulse duration, repetition rate) altered the total application time required for stone fragmentation, the stone break up time, and the propulsion. The obtained results can be used to develop lithotripsy devices providing an optimal combination of low stone propulsion and high fragmentation efficacy, which can then be evaluated in a clinical setting. Additionally, the fluorescence of human kidney stones was inspected endoscopically in vivo. Fluorescence light can be used to detect stone-free areas or to clearly distinguish calculi from surrounding tissue or operation tools.

© 2018 Optical Society of America under the terms of the [OSA Open Access Publishing Agreement](#)

1. Introduction

Ureteroscopic Ho:YAG laser lithotripsy is a preferred method for treating urinary stone disease [1–6]. Clinical lithotripsy is performed endoscopically by application of laser pulses to the calculi. The laser light is guided to the stone by an optical wave guide that is inserted into the working channel of either a rigid or flexible endoscope. Clinically, Ho:YAG lasers ($\lambda = 2.1 \mu\text{m}$) are widely used for this application, owing to the high absorption coefficient of water at the respective wavelength. This allows to induce not only thermo-mechanical ablation on the stone surface, but also photothermal fragmentation by expansion of the water contained in urinary stones [7]. To compare different laser systems and laser parameters, different experimental set-ups have been proposed [8–14]. Such set-ups were designed to quantify the fragmentation rate and the dusting efficacy. Although the term dust has not been defined finally to distinguish between the two processes, a definition of dust as fragments smaller than 1 mm has been proposed [15]. Along with the desired stone destruction, pulsed laser light also accelerates the urinary stone (propulsion effect), resulting in the need to “chase the stone” with the endoscope along the ureter. Such manoeuvres may result in a longer treatment time and the possibility of losing the stone or stone fragments [9, 10, 16]. Both, fragmentation and propulsion processes, are highly influenced by the chosen laser parameters (pulse energy, pulse duration, repetition rate) [15, 17, 18]. The propulsion can be measured via a variety of methods, for example by evaluating the maximum deflection angle of a pendulum due to laser impact [18–21] or by analysing horizontal [9–12] or vertical stone movements [13] in terms of maximum stone displacement. The main disadvantage of these techniques is that the propulsion effect of only one single laser pulse can be evaluated. In this study, a combination of maximum vertical stone displacement analysis and object tracking via high speed camera was used to determine the propulsion characteristics of pulse trains over an observation time of 7 seconds [22]. Beyond the quantification of stone destruction and propulsion, a third challenge is posed by the proper detection of small fragments. Small fragments may remain untreated clinically because of insufficient visibility and/or low

contrast with the surrounding tissue under white light illumination. Suitable recognition techniques have been proposed and are still under development [23–25]. In view of these three clinical challenges, the following investigations on fragmentation and propulsion of artificial stones as well as fluorescence response of human calculi were performed to identify optimisation potential in the procedure of laser lithotripsy. The main focus was set on the fragmentation and propulsion experiments using an experimental laser system, while for fluorescence response measurements first results are shown.

2. Material and methods

2.1 Laser device and artificial calculi

As laser source an experimental Ho:YAG device ($\lambda = 2.1 \mu\text{m}$) was used, providing a huge range of laser settings: pulse energies (E) from 0.5 J/pulse up to 2.5 J/pulse, repetition rates (f) from 10 Hz to 80 Hz, and optical pulse durations (t) up to 4 ms. A detailed listing of the settings used is shown in Table 1. One combined setting was used where the stone was fragmented until the stone broke up (t_{break}) with 0.5 J/pulse, 0.4 ms pulse length and 80 Hz repetition rate, then the fragmentation was continued using 2.5 J/pulse, 4.0 ms and 10 Hz. As the used laser source was an experimental device it was decided to use an optical fiber with core diameter of 365 μm for all experiments to guarantee optimal coupling efficacy and to prevent damage to the coupling optics, the coupling plug or the fiber itself. With the laser device it was possible to create a great variation in pulse length (0.25 ms- 4.0 ms), energy per pulse (0.4 J/pulse - 2.5 J/pulse). Depending on the pulse length and energy per pulse repetition rates up to 80 Hz could be used. The selection of settings in Table 1 was chosen due to experiences from former experiments [15, 20, 22, 26] with standard Ho:YAG laser sources and current state of the art laser settings using high repetition rates in combination with variations in pulse length and energy per pulse [13, 27, 28].

Table 1. Laser settings used for fragmentation and propulsion experiments

E [J]	t [ms]	f [Hz]	P_{Average} [W]
0.5	0.3	10	5
0.5	0.4	80	40
0.5	0.6	10	5
0.5	1.0	10	5
0.5	1.2	40	20
0.5	1.3	10	5
0.5	1.6	10	5
0.5	2.2	30	15
1.0	0.3	10	10
1.0	0.6	10	10
1.0	1.0	10	10
1.0	1.2	10	10
1.0	0.8	40	32
1.0	1.2	40	40
1.0	1.6	10	10
1.0	2.2	30	30
1.5	0.3	10	15
1.5	1.0	10	15
2.0	0.3	10	20
2.0	1.0	10	20
2.0	4.0	10	20
2.5	4.0	10	25

Cubical (edge length: 5 mm) and spherical (\varnothing : 6 mm) artificial calculi made out of Bego powder (BEGO, BEGO GmbH & Co KG, Bremen, Germany) were used for the fragmentation and propulsion experiments. All stones were used “dry” without immersion in water beforehand. The hardness of the calculi was adjusted by the compound-to-water ratio

(here: 15:4) and comparable to human kidney stones, for a composition intermediate between calcium oxalate monohydrate and ammonium magnesium phosphate hydrate [29].

2.2 Fragmentation set-up

Laser light delivered via a standard optical fibre ($\varnothing_{\text{core}}$: 365 μm) was directed perpendicularly from the top onto the surface of artificial calculi recumbent in an acrylic glass vessel that was submerged in water (Fig. 1). An adjustable water flow (max. 250 ml/min) provided for clear vision even if the used laser setting produced a lot of dust. By moving the application fiber smoothly across the surface of the stone phantom, thereby maintaining mechanical contact, the stone was ablated layer by layer until the vessel was free from any stone debris.

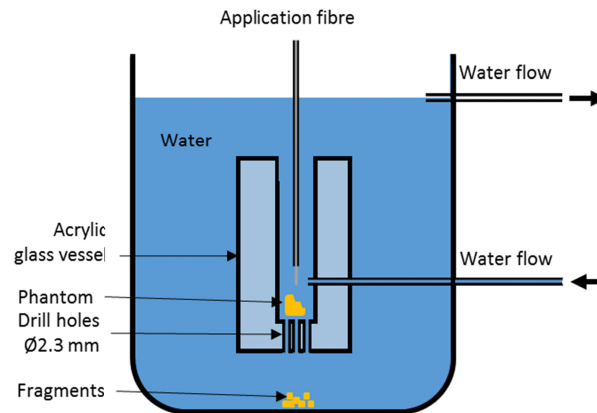


Fig. 1. Experimental set-up for the investigation of fragmentation and dusting efficacy.

The total application time (t_{total}) was defined as the period it took to destruct the stone until all fragments were smaller than 2.3 mm [30] and hence had fallen through the holes drilled into the bottom of the vessel. Additionally, the “break up” time (t_{break}) was recorded, defined as the application time after which the stone broke up for the first time, marking the cross-over from pure dusting to combined fragmentation and dusting. The time after break ($t_{\text{afterbreak}}$) was defined as the remaining time, calculated according to E1 of Table 2. Weighing of each single artificial calculus was performed prior to each experiment. After each experiment and after sieving and drying of the residual fragments (defined by a fragment size between 1 mm and 2.3 mm), the fragments were weighed (MC1, SartoriusAG, Göttingen, Germany). The amount of dust (m_{dust}) produced could then be calculated by taking the difference between the initial mass (m_{initial}) and the residual fragments’ mass (m_{fragment}) (E2). The dusting ratio $D = m_{\text{dust}}/m_{\text{initial}}$ was used as a quantitative measure of the dusting efficacy (E3). All experiments were performed several times ($n \geq 5$) for each set of laser parameters (pulse energy, pulse duration, repetition rate) according to Table 1.

Table 2. Evaluation of the fragmentation experiment.

E1	Total application time t_{total}	$t_{\text{afterbreak}} = t_{\text{total}} - t_{\text{break}}$
E2	Mass of dust m_{dust}	$m_{\text{dust}} = m_{\text{initial}} - m_{\text{fragment}}$
E3	Dust ratio D	$D = m_{\text{dust}}/m_{\text{initial}} \cdot 100\%$

2.3 Propulsion set-up

As shown in Fig. 2, a user-independent experiment set-up was created in which the pulsed laser light was applied from below to cubical and spherical BegoStone phantoms loosely guided within a vertical column filled with water. The stone movement was recorded via a high speed camera system with 1000 fps (DSC RX-100 V, Sony, Tokyo, Japan). The total recording time was limited to 7 seconds by the internal buffer space, hence just 7 second long movement profiles could be evaluated.

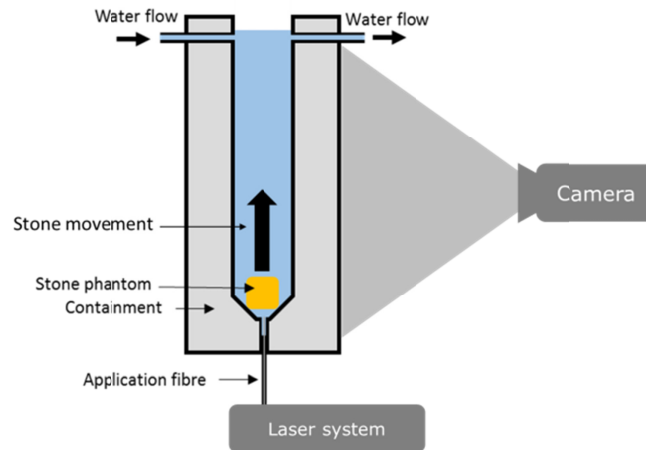


Fig. 2. Experimental set-up for the propulsion measurement.

These movement profiles were generated by a video tracking method [22] that uses an automatic algorithm to determine the vertical stone position (centroid amplitude) in each frame of a recorded scene. Two exemplary movement profiles are shown in Fig. 3 for a cubical and a spherical artificial stone. The time-dependence of the vertical stone position is characterized by an irregular series of peaks. By analysing the slopes of the rising flanks of these peaks it was possible to determine the mean upward velocity of the stone for a whole pulse train scene of up to 7 s duration and finally to use this for comparison of the propulsion effects associated with different laser settings.

The water flow was set constant (150 ml/min) and provided for clear vision into the vessel under consistent conditions (regarding water level and flow) for every single experiment on cubical and spherical artificial stones. A repetition rate of 10 Hz was chosen for all experiments, while pulse energies were varied from 0.5 J/pulse to 2.0 J/pulse in 0.5 J/pulse steps and pulse durations from 0.3 ms to 1.0 ms according to Table 1. For each laser setting, the experiment was repeated on $n = 15$ different freshly prepared stones. The mean value out of these 15 measurements was used to estimate the propulsion effect for each laser setting.

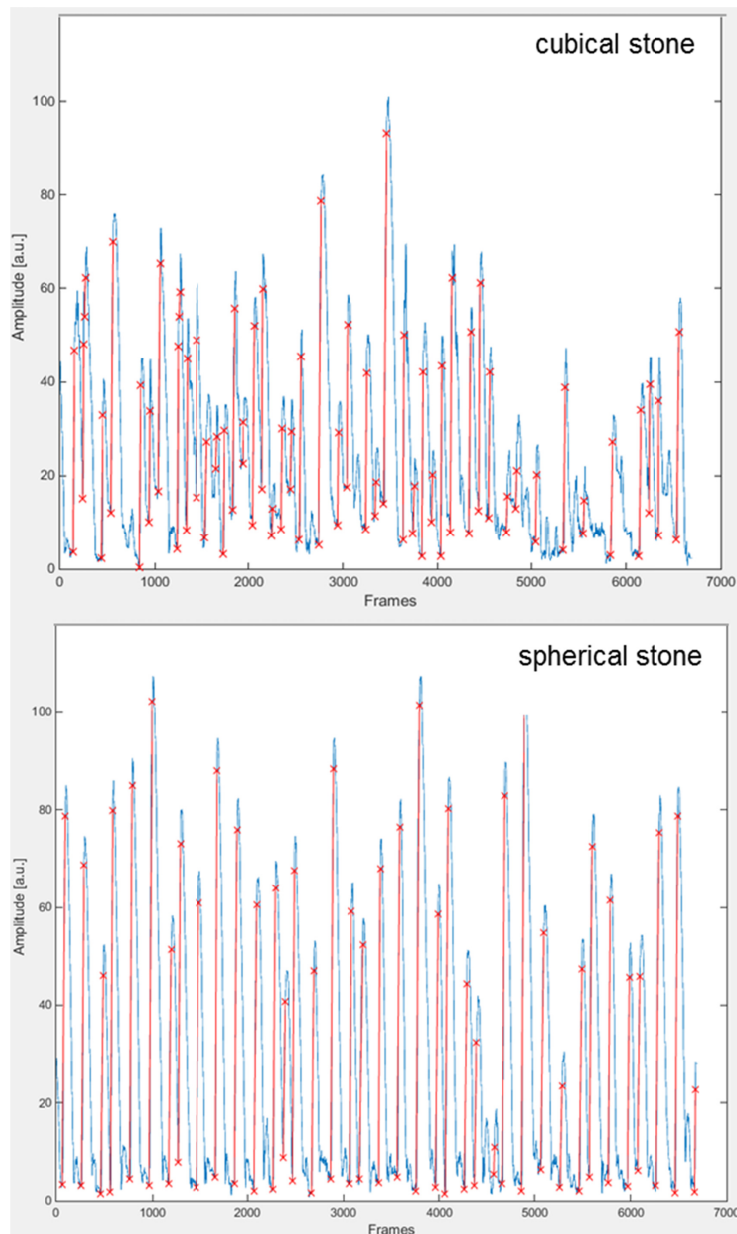


Fig. 3. Vertical centroid coordinate of a cubical (upper graph) and a spherical (lower graph) phantom stone observed during laser application (1 J/pulse, 1 ms, 10 Hz) as a function of the frame number.

2.4 Fluorescence measurement

Urinary stones harvested from patients were spectrally analyzed in in-vitro measurements via a fluorescence microscope (Leica DM IRBE, Wetzlar, Germany) under illumination with light from a bandpass filtered mercury arc lamp (Osram HBO 103, Munich, Germany) as shown in Fig. 4. Images were taken with an attached camera system (telcam SL pal 20212020, KARL STORZ GmbH & Co. KG, Tuttlingen, Germany), while a spectrometer (USB 2000 + , Ocean Optics, Ostfildern, Germany) recorded the spectral data from a small spot in the center of the image (Fig. 4).

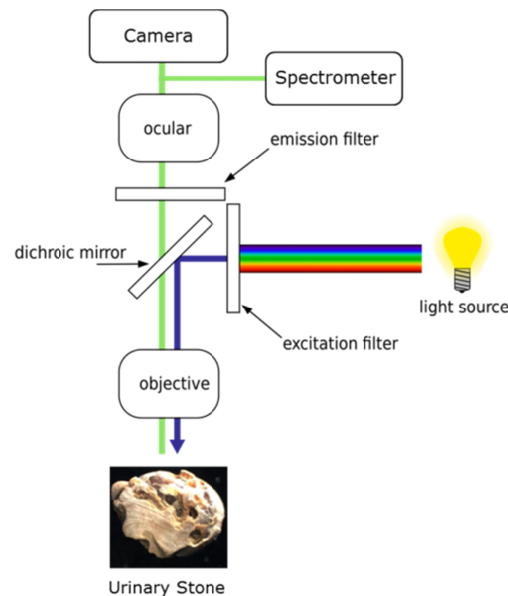


Fig. 4. Schematic set-up of fluorescence microscope.

Using different excitation filters, light of the wavelength bands (400 ± 5) nm, (450 ± 10) nm and (550 ± 5) nm was applied to the stone (30% calcium-oxalate-monohydrate, 70% carbonate apatite) for fluorescence excitation. The thereupon emitted fluorescence light was detected after passing long pass filters of $\lambda > 470$ nm, $\lambda > 520$ nm and $\lambda > 590$ nm, respectively.

Additionally, the fluorescence of two urinary stones (stone 1: 100% calcium-oxalate-monohydrate; stone 2: 80% uric acid, 20% calcium-oxalate-monohydrate) was inspected in-vivo during endoscopic stone treatments to identify potential advantages of fluorescence guidance during this procedure. In this case, the endoscopic scene was illuminated first with white light and subsequently with green light ($\lambda = 500\text{-}570$ nm, Light source: D-Light C 20133220, Karl-Storz SE & Co. KG, Tuttlingen, Germany; Band pass filter: 540/60, transmission $>80\%$ in the range 500-567 nm, AHF Analysetechnik, Tübingen, Germany). The stone fluorescence was observed through a long pass filter ($\lambda > 610$ nm) via the ocular of the endoscope. White light and fluorescence response images were subjectively compared to each other.

2.5 Statistical evaluation

Statistical evaluation of the data (mean, standard deviation, significance) was performed using Sigma Plot (V.11.0, Systat Software GmbH, Erkrath, Germany). To test the significance of differences between the obtained means for multiple groups, the one way ANOVA (Holm-Sidak) method was used.

3. Results

3.1 Fragmentation

In Fig. 5 and Fig. 6 selected results of the experiments regarding t_{total} , t_{break} , and $t_{\text{afterbreak}}$ are shown. Figure 5 presents all settings with average powers 10 W (upper section) and 5 W (lower section) using pulse length from 0.3 ms up to 1.6 ms. The amount of dust produced ranged between around 60% (1.0J/pulse, 0.3 ms, 10 Hz) and 73% (1J/pulse, 1.2 ms, 10 Hz). Concerning t_{break} all settings showed significant difference ($p < 0.001$), except for the two 5W settings (with 1.3 ms and 1.6 ms optical pulse length) ($p = 0.056$). Regarding the total

application time t_{total} the 10W situations showed just significant difference for pulse length of 0.3 ms and 1.2 ms, while all 5 W settings were significant different.

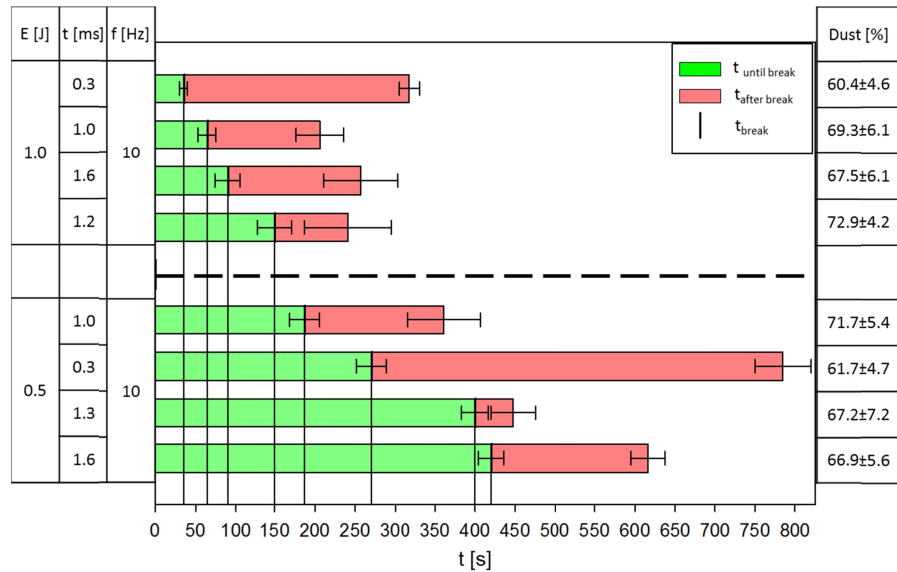


Fig. 5. Fragmentation times and dusting ratios for varying pulse duration, obtained at a constant repetition rate of 10 Hz for pulse energies of 1.0 J (P_{Average} : 10W, upper section) and 0.5 J (P_{Average} : 10W, lower section), respectively. Different optical pulse lengths (0.3ms-1.6ms) were investigated. Error bars represent the standard deviations of the total application time t_{total} and the break up time t_{break} . The dusting ratios with their respective standard deviation are shown in the right column.

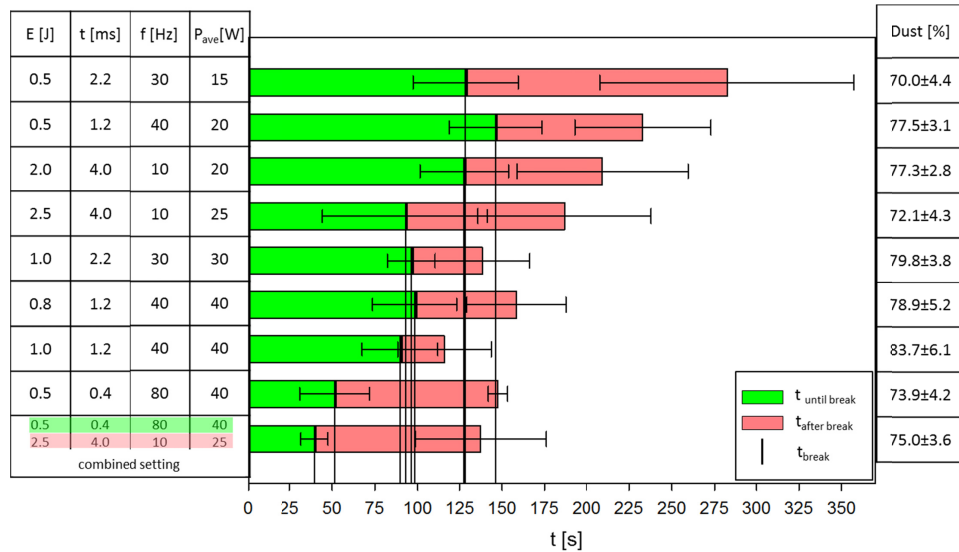


Fig. 6. Fragmentation times and dusting ratios for a selection of pulse energies, pulse durations, and repetitions rates sorted by the average power of each setting. Error bars represent the standard deviations of the total application time t_{total} and the break up time t_{break} . In case of the combined setting the laser configuration (0.5J/pulse, 0.4 ms, 80 Hz) for treatment until t_{break} is highlighted in green and the setting for further fragmentation (2.5J/pulse, 4.0 ms, 10 Hz) in red. The dusting ratios with their respective standard deviation are shown in the right column.

In Fig. 6 the fragmentation experiment results for settings from average power of 15 W up to 40 W are illustrated. The highest application time t_{total} was around 280 s, the shortest time measured roughly 115 s. Dusting ratios were ranging between 70% (setting 1: 0.5 J/pulse, 2.2 ms, 30 Hz) up to nearly 84% (setting 7: 1.0 J/pulse, 1.2 ms, 40 Hz). The four fastest settings concerning t_{total} were (setting 5: 1.0 J/pulse, 2.2 ms, 30 Hz), setting 7 (setting 8: 0.5 J/pulse, 0.4 ms, 80 Hz) and (setting 9: setting 8 + 4). No significant difference ($p < 0.001$) could be found concerning the total application time, for t_{break} there were significant differences except for setting combinations of 5 and 7 ($p = 0.597$) as well as for 8 and 9 ($p = 0.593$). Doubling the energy per pulse from 0.5 J for setting 1 (0.5 J/pulse, 2.2 ms, 30 Hz) to 1.0 J in setting 5 (1.0 J/pulse, 2.2 ms, 30 Hz) showed significant difference in t_{total} but not in t_{break} . Comparing the two 40 Hz settings 2 (0.5 J/pulse, 1.2 ms, 40 Hz) and 7 (1.0 J/pulse, 1.2 ms, 40 Hz) there was significant difference for t_{total} and t_{break} . All in all the fragmentation of stones using a variety of laser settings showed a great variation in total application time from around 120 s (1.0 J, 1.2 ms, 40 Hz) (Fig. 6) to almost 800 s (0.5 J, 0.3 ms, 10 Hz) (Fig. 5). Apparently, based on the selection of laser settings in Fig. 5, a pulse energy of at least 1.0 J is recommendable for efficient fragmentation in terms of total application time. In combination with high repetition rates (80 Hz), however, low pulse energy settings (0.5 J, 0.4 ms, 80 Hz) may also lead to fairly fast fragmentation (Fig. 6).

3.2 Propulsion

In Fig. 7 the evaluated average vertical velocity values are displayed for a selection of 9 different laser settings, in each case for both, the cubical and the spherical phantom model. The propulsive effect, respectively the mean upward velocity of the stone, increases with increasing pulse energy only very slightly, whereas an elongation of the pulse duration is clearly associated with a declining mean upward velocity. As the repetition rate remained unchanged at 10 Hz in all experiments, it is not possible to make a statement about a potential influence of the repetition rate on the propulsive effect.

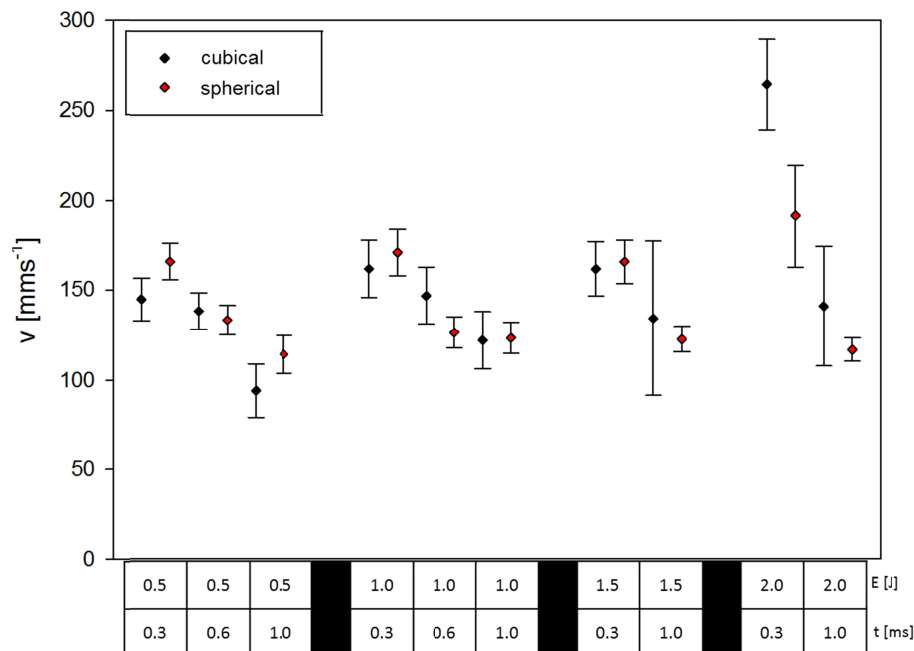


Fig. 7. Comparison of laser-induced stone phantom propulsion velocities v obtained with the video tracking software at a constant repetition rate of 10 Hz for different pulse energies E (0.5J-2J), respectively average powers P_{Ave} (5W-20W) and pulse durations t . The data points and error bars represent the mean propulsion velocities and their standard deviations.

3.3 Fluorescence

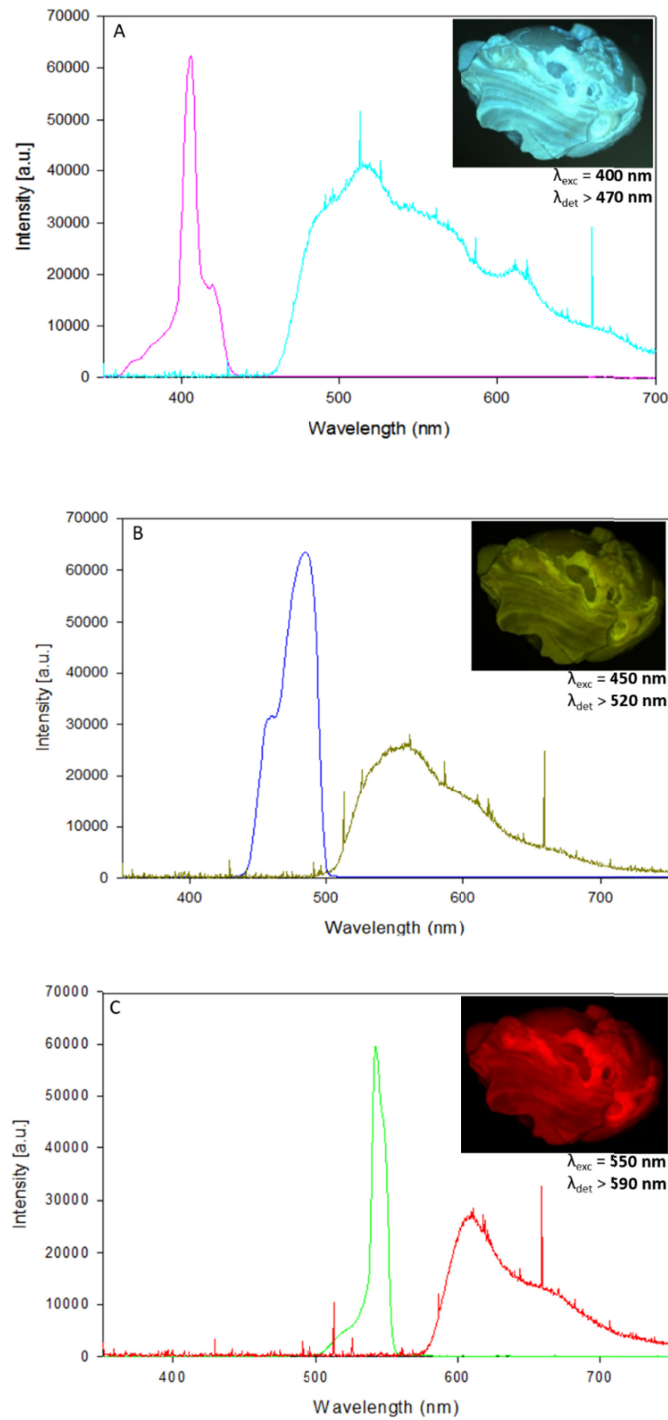


Fig. 8. Fluorescence response of a human kidney stone (Inset) using three different excitation wavelengths (λ_{exc} : 400 nm, 450 nm, 550 nm) and corresponding long pass emission filters (λ_{onset} : 470 nm, 520 nm, 590 nm).

In Fig. 8 exemplary fluorescence emission spectra are shown, obtained in vitro from a human kidney stone for three different excitation wavelengths (λ_{exc} : 400 nm, 450 nm, 550 nm). The graphs illustrate that the stones exhibit a well detectable amount of fluorescence emission, covering a broad spectral range from 580 nm to 740 nm when excited with 550 nm and detected through a long pass filter with a nominal onset wavelength of 590 nm.

Endoscopic white light and fluorescence images of urinary stones obtained in a clinical situation under white light and green light illumination (λ_{exc} : 500-570 nm, λ_{det} : >610 nm), respectively, are shown in Fig. 9. Under white light illumination the stone can hardly be distinguished from surrounding tissue and catheters, under green light illumination the boundaries between stone and tissue are clearly visible. Due to the emitted fluorescence, stone 1 shows an enhancement in contrast. Stone 2 is already clearly distinguishable from the surrounding tissue under white light illumination. Endoscopic devices (e.g. catheter, guide wire, marked by red cycles in Fig. 9) are not visible at all in the case of fluorescence detection under green light illumination as they do not show any fluorescence under these conditions.

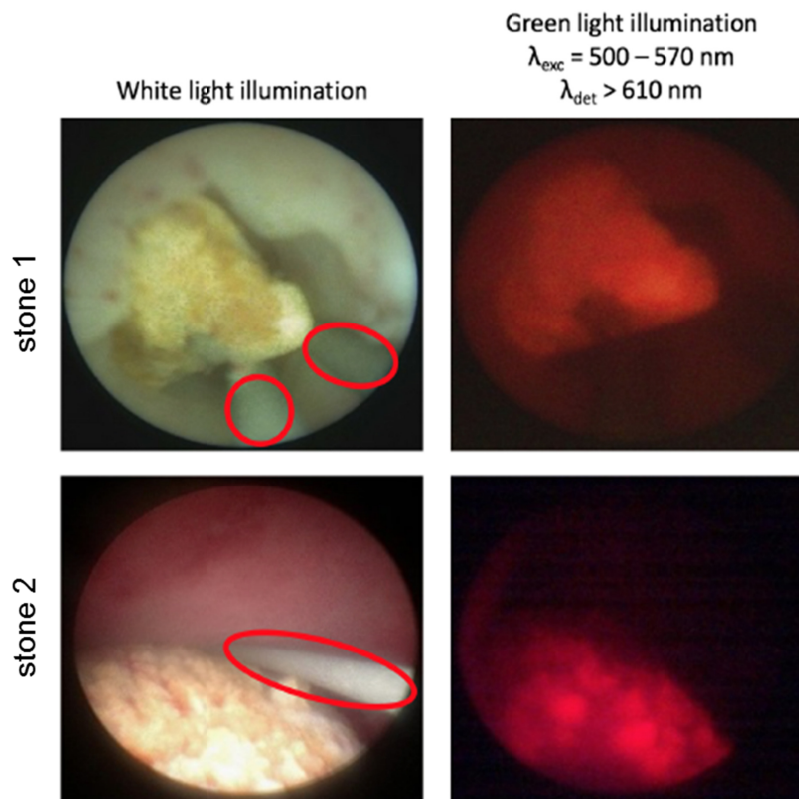


Fig. 9. White light and fluorescence images of two urinary stones recorded in vivo with an endoscopic camera system. For fluorescence excitation, filtered green light illumination (λ_{exc} = 500 – 570 nm) was applied, for fluorescence detection, a long-pass filter (λ_{det} > 610nm) was implemented in the imaging system. Endoscopic tools are highlighted with red circles.

4. Discussion

Our examination of stone fragmentation using a selection of different laser settings showed that varying the laser parameters (pulse energy, pulse duration, repetition rate) altered the total application time as well as the break up time. In this context the propulsion, even if not measured for all settings, appears to be higher for shorter pulse duration (for constant pulse energy and repetition rate) and may also have an additional effect on the fragmentation due to

time consuming chasing of the fragments respectively the break-up behaviour. For time-effective fragmentation it would be desirable to have maximal ablation rate (total application time short) with late break-up of the treated stone (fragments occur very late during the application) and low propulsion when it comes to “chasing” the remaining fragments. Generally speaking, a simultaneous increase of pulse energy and/or pulse duration as well as using repetition rates above 30 Hz seems to be a promising approach in the improvement of laser induced lithotripsy. This can be extrapolated from Fig. 5 and Fig. 6, using repetition rates of 10 Hz (Fig. 5) the shortest settings regarding to t_{total} ranged between 200 s (1J/pulse, 1 ms, 10 Hz) and 260 s (1J/pulse, 1.6 ms, 10 Hz), whereas in Fig. 6 fastest t_{total} lay between 115 s (setting 7: 1.0J/pulse, 1.2ms, 40Hz) and 150 s (setting 8: 0.5J/pulse, 0.4 ms, 80 Hz). The dusting ratios varied between 61% and 84% in all cases.

Doubling of the energy per pulse for constant pulse duration and repetition rate as mentioned beforehand (setting 1: 0.5J/pulse, 2.2 ms, 30 Hz; setting 5: 1.0J/pulse, 2.2 ms, 30 Hz) and (setting 2: 0.5 J/pulse, 1.2 ms, 40 Hz; setting 7: 1.0 J/pulse, 1.2 ms, 40 Hz) results in significant reduction of t_{total} , but not in the same way for t_{break} . Even though a setting using low energy per pulse and short pulse length at high repetition rates (Fig. 6: setting 8: 0.5J/pulse, 0.4 ms, 80 Hz) was effective regarding to t_{total} , but a short break up time thenceforward the remaining fragments are further crushed due to recently described “popcorn-technique” [31, 32]. There was also no improvement in t_{total} using setting 8 until t_{break} in combination with setting 4 (2.5J, 4.0 ms, 10 Hz) for continuing the treatment of the fragments. Unfortunately the experimental laser system was just available to test the settings presented, therefore it would be of interest to test such “combined settings” on significant impact on the improvement of the overall efficacy of the treatment. The correlation between the laser parameters, fragmentation times and dusting efficacy has to be further investigated, particularly in combination with the generated propulsion. Based on these first preliminary data sets in this work it will be possible to continue on profound data. Recently another potential method was published which uses experimental data on fragmentation (here: ablation volume) and propulsion at different laser settings (here: pulse duration and number of pulses, for constant pulse energy) to derive an analytic model function for predicting treatment efficacy from laser parameters [30]. This might be an interesting tool for further optimization of laser settings and laser development.

In the propulsion experiments [22], the result reproducibility was better when using spherical (first used in this work) instead of cubical stone phantoms. In Fig. 3 it is illustrated that the movement profile of the spherical stones (lower graph) during laser application is more uniform compared to that of the cubical stones (upper graph). In former experiments using cubes it was observed that the cubes became sometimes stuck in the experimental apparatus, hence the movement profile was more irregular compared to the spherical phantoms. Obviously this renders such experiments time-consuming and the result quality less satisfactory or both, which is why spherical artificial stones were introduced in this work to improve the overall quality of the set-up. In Fig. 7, most results obtained for the propulsion velocity are nevertheless in agreement for both phantom shapes. In other respects, further optimisation of the propulsion set-up might be useful in terms of adjustments to fibre distance and water flow. The experimental set-ups for fragmentation and propulsion experiments were developed on the one hand to mimic a clinical situation, but also to guarantee reproducible and reliable results in lab tests, therefore the both set-ups were optimized for good handling (Operator) and accessibility (laser fiber, maintenance). The main focus lay on the reproducible comparison of different laser settings and laser systems. Especially in case of the Propulsion set-up the vertical movement of the stone was used for evaluation was used as the gravitation served as “constant” counterforce to bring the stone back into its origin position. By keeping the water flow and level constant it was possible to achieve very similar conditions for each stone respectively laser setting tested. Even though the clinical situation differs from these experimental set-ups, the experimental procedure was in case of the

propulsion experiment independent of the investigator, using the fragmentation set-up the influence of the operator (subjective influences, including motivation and experience, on the obtained results and conclusions) could successively be minimized [15]. As a consequence, a high reproducibility could gradually be achieved in the evaluation of different laser systems and laser parameters.

Besides fragmentation and movement of calculi, the fluorescence of human kidney stones was investigated in this study. Interesting approaches in this area were recently introduced that involved fluorescence excitation on kidney stones with the aiming beam of a laser system [24, 25]. This enables one to develop a feedback system for the laser device to differentiate hard and soft tissue in front of the fiber tip and finally to avoid accidental laser pulse application to surrounding soft tissue [33]. In this study it could be shown that the urinary stones emitted sufficiently intense fluorescence light, allowing to clearly distinguishing them from surrounding tissue or operation tools such as guide wires, catheters and endoscopes. With that, an endoscope-based safety feature can be envisioned in combination with a suitable color tracking algorithm. In case of the stone or the fiber out of sight or for instance inside the working channel there is a risk to hit operation tools, which could be avoided by activation of an emergency alarm [34]. Innovations in laser development resulted in the introduction of high power Ho:YAG lasers on the market, providing an average power around 100W, which can be very efficient in stone destruction [35–37]. Furthermore, attention should in particular also be dedicated to heat generation inside the urinary tract when using such high power laser devices [38–42]. Fluorescence-assisted endoscopic laser lithotripsy should be introduced in particular in connection with high power laser devices. While these may be equipped with temperature measurement features to minimize possible heat-induced damages to surrounding soft tissue, fluorescence may provide a prompt feedback signal to prevent direct laser application on tissue. Further investigations on all efficacy and safety aspects of lithotripsy (fragmentation, dusting, propulsion, stone recognition, and stone/tissue differentiation) should certainly be performed to improve the clinical outcome for the benefit of the patient.

5. Conclusion

Based on the set-ups used in this study, reproducible data sets concerning fragmentation for a variation of energy per pulse (0.5J-2.5J), pulse length (0.25 ms-4.0ms) and repetition rates (10Hz- 80Hz) were created. Elongation of pulse length ($>1\text{ms}$) in combination with simultaneously increase of energy per pulse dependent on the laser system's capacity and higher repetition rates ($>30\text{ Hz}$) seems to be a promising approach to improve fragmentation efficacy. Propulsion experiments were performed for different energies per pulse (0.5J-2.5J), pulse length (0.3ms, 0.6ms, 1.0ms) at repetition rates of 10 Hz showing that the reproducibility of the results could be improved by the use of spherical instead of cubical artificial stones. In combination these data sets can be used to obtain laser lithotripsy procedure, meaning using the full potential (high ablation rate, smallest fragment diameter (dust), lowest propulsion) of laser devices currently or in the future available on the market. Broadband fluorescence response of human calculi could be a useful tool to retrieve lost stones or fragments (possible increase of stone free rate) or can be used as a further safety feature for laser lithotripsy (reduction of collateral damage to surrounding tissue or endoscopic devices).

Acknowledgments

This manuscript is part of the inaugural thesis of Maximilian Eisel to be submitted at the Medical Faculty of the Ludwig-Maximilians-Universität, Munich.

Disclosures

The authors declare that there are no conflicts of interest related to this article.

References

1. M. T. Gettman and J. W. Segura, "Management of ureteric stones: issues and controversies," *BJU Int.* **95**(s2), 85–93 (2005).
2. S. P. Dretler, "Laser lithotripsy: a review of 20 years of research and clinical applications," *Lasers Surg. Med.* **8**(4), 341–356 (1988).
3. A. Hofstetter, "Lasers in urology," *Lasers Surg. Med.* **6**(4), 412–414 (1986).
4. A. Vogel, "Nonlinear absorption: intraocular microsurgery and laser lithotripsy," *Phys. Med. Biol.* **42**(5), 895–912 (1997).
5. B. Altay, B. Erkurt, and S. Albayrak, "A review study to evaluate holmium:YAG laser lithotripsy with flexible ureteroscopy in patients on ongoing oral anticoagulant therapy," *Lasers Med. Sci.* **32**(7), 1615–1619 (2017).
6. A. Hofstetter, "The Laser in Urology (State of the Art)," *Laser-Medizin* **15**(4), 155–160 (2000).
7. A. J. Marks, J. Qiu, T. E. Milner, K. F. Chan, and J. M. H. Teichman, "Laser lithotripsy physics," in *Urinary Tract Stone Disease*, N. P. Rao, G. M. Preminger, and J. P. Kavanagh, eds. (Springer, 2011), pp. 301–309.
8. R. Sroka, T. Pongratz, F. Strittmatter, M. Eisel, and S. Ströbl, "In-vitro investigation on fragmentation/dusting and fluorescence during Ho:YAG-Laser induced lithotripsy," (Conference Presentation) in *SPIE BiOS* (SPIE, 2018).
9. H. Lee, R. T. Ryan, J. M. H. Teichman, J. Kim, B. Choi, N. V. Arakeri, and A. J. Welch, "Stone retropulsion during holmium:YAG lithotripsy," *J. Urol.* **169**(3), 881–885 (2003).
10. M. Sofer, J. D. Watterson, T. A. Wollin, L. Nott, H. Razvi, and J. D. Denstedt, "Holmium:YAG laser lithotripsy for upper urinary tract calculi in 598 patients," *J. Urol.* **167**(1), 31–34 (2002).
11. H. W. Kang, H. Lee, J. M. H. Teichman, J. Oh, J. Kim, and A. J. Welch, "Dependence of calculus retropulsion on pulse duration during Ho: YAG laser lithotripsy," *Lasers Surg. Med.* **38**(8), 762–772 (2006).
12. J. Sea, L. M. Jonat, B. H. Chew, J. Qiu, B. Wang, J. Hoopman, T. Milner, and J. M. Teichman, "Optimal power settings for Holmium:YAG lithotripsy," *J. Urol.* **187**(3), 914–919 (2012).
13. M. M. Elhilali, S. Badaan, A. Ibrahim, and S. Andonian, "Use of the Moses Technology to Improve Holmium Laser Lithotripsy Outcomes: A Preclinical Study," *J. Endourol.* **31**(6), 598–604 (2017).
14. P. Kronenberg and O. Traxer, "In vitro fragmentation efficiency of holmium: yttrium-aluminum-garnet (YAG) laser lithotripsy--a comprehensive study encompassing different frequencies, pulse energies, total power levels and laser fibre diameters," *BJU Int.* **114**(2), 261–267 (2014).
15. M. J. Bader, T. Pongratz, W. Khoder, C. G. Stief, T. Herrmann, U. Nagele, and R. Sroka, "Impact of pulse duration on Ho:YAG laser lithotripsy: fragmentation and dusting performance," *World J. Urol.* **33**(4), 471–477 (2015).
16. S. P. Dretler, "Ureteroscopy for Proximal Ureteral Calculi: Prevention of Stone Migration," *J. Endourol.* **14**(7), 565–567 (2000).
17. R. Sroka, T. Pongratz, G. Scheib, W. Khoder, C. G. Stief, T. Herrmann, U. Nagele, and M. J. Bader, "Impact of pulse duration on Ho:YAG laser lithotripsy: treatment aspects on the single-pulse level," *World J. Urol.* **33**(4), 479–485 (2015).
18. P. Kronenberg and O. Traxer, "Update on lasers in urology 2014: current assessment on holmium:yttrium-aluminum-garnet (Ho:YAG) laser lithotripter settings and laser fibers," *World J. Urol.* **33**(4), 463–469 (2015).
19. T. C. Hutchens, D. A. Gonzalez, P. B. Irby, and N. M. Fried, "Fiber optic muzzle brake tip for reducing fiber burnback and stone retropulsion during thulium fiber laser lithotripsy," *J. Biomed. Opt.* **22**(1), 018001 (2017).
20. R. Sroka, N. Haseke, T. Pongratz, V. Hecht, D. Tilki, C. G. Stief, and M. J. Bader, "In vitro investigations of repulsion during laser lithotripsy using a pendulum set-up," *Lasers Med. Sci.* **27**(3), 637–643 (2012).
21. J. J. Zhang, D. Rajabhandharaks, J. R. Xuan, R. W. J. Chia, and T. Hasenberg, "Calculus migration characterization during Ho:YAG laser lithotripsy by high-speed camera using suspended pendulum method," *Lasers Med. Sci.* **32**(5), 1017–1021 (2017).
22. M. Eisel, S. Ströbl, T. Pongratz, F. Strittmatter, and R. Sroka, "In vitro investigations of propulsion during laser lithotripsy using video tracking," *Lasers Surg. Med.* **50**(4), 333–339 (2018).
23. D. Schlager, J. Schütz, A. Brandenburg, and A. Miernik, "1201 - Seek and destroy: A novel laser system with real-time automatic target identification for urinary stone lithotripsy. An in-vivo study," *Eur. Urol. Suppl.* **17**(2), e1682 (2018).
24. B. Lange, J. Cordes, and R. Brinkmann, "Stone/tissue differentiation for holmium laser lithotripsy using autofluorescence," *Lasers Surg. Med.* **47**(9), 737–744 (2015).
25. B. Lange, D. Jocham, R. Brinkmann, and J. Cordes, "Stone/tissue differentiation for Holmium laser lithotripsy using autofluorescence: clinical proof of concept study," *Lasers Surg. Med.* **49**(4), 361–365 (2017).
26. K. Stock, D. Steigenhöfer, T. Pongratz, R. Graser, and R. Sroka, "Investigation on cavitation bubble dynamics induced by clinically available Ho:YAG lasers," *Photonics Lasers Med.* **5**(2), 141–150 (2016).
27. R. Li, D. Ruckle, M. Keheila, J. Maldonado, M. Lightfoot, M. Alsyoud, A. Yeo, S. R. Abourbih, G. Olgin, J. L. Arenas, and D. D. Baldwin, "High-frequency dusting versus conventional holmium laser lithotripsy for intrarenal and ureteral calculi," *J. Endourol.* **31**(3), 272–277 (2017).
28. D. A. Wollin, E. C. Carlos, W. R. Tom, W. N. Simmons, G. M. Preminger, and M. E. Lipkin, "Effect of laser settings and irrigation rates on ureteral temperature during holmium laser lithotripsy, an in vitro model," *J. Endourol.* **32**(1), 59–63 (2018).

29. E. Esch, W. N. Simmons, G. Sankin, H. F. Cocks, G. M. Preminger, and P. Zhong, "A simple method for fabricating artificial kidney stones of different physical properties," *Urol. Res.* **38**(4), 315–319 (2010).
30. D. A. Rebeck, A. Macejko, V. Bhalani, P. Ramos, and R. B. Nadler, "The natural history of renal stone fragments following ureteroscopy," *Urology* **77**(3), 564–568 (2011).
31. P. Klaver, T. de Boorder, A. I. Rem, T. M. T. W. Lock, and H. J. Noordmans, "In vitro comparison of renal stone laser treatment using fragmentation and popcorn technique," *Lasers Surg. Med.* **49**(7), 698–704 (2017).
32. A. H. Aldoukhi, W. W. Roberts, T. L. Hall, and K. R. Ghani, "Holmium laser lithotripsy in the new stone age: dust or bust?," *Frontiers in Surgery* **4**, 57 (2017).
33. D. Beaucamp, R. Engelhardt, P. Hering, and W. Meyer, *Stone Identification during Laser Induced Shock Wave Lithotripsy* (Springer Berlin Heidelberg, 1990).
34. K. Xavier, G. W. Hruby, C. R. Kelly, J. Landman, and M. Gupta, "Clinical evaluation of efficacy of novel optically activated digital endoscope protection system against laser energy damage," *Urology* **73**(1), 37–40 (2009).
35. M. S. Nomikos, G. Koritsiadis, N. Bafaloukas, G. Athanasopoulos, and S. Papanikolaou, "P10 - Safety and efficacy of high power Holmium-Yag laser in percutaneous nephrolithotomy," *Eur. Urol. Suppl.* **17**(4), e2017 (2018).
36. J. W. Lee, J. Park, M. C. Cho, H. Jeong, H. Son, and S. Y. Cho, "PD30-12 How to perform the dusting technique for calcium oxalate stones during Ho:YAG lithotripsy," *J. Urol.* **197**(4), 582 (2017).
37. S. Chen, L. Zhu, S. Yang, W. Wu, L. Liao, and J. Tan, "High- vs low-power holmium laser lithotripsy: a prospective, randomized study in patients undergoing multitract minipercutaneous nephrolithotomy," *Urology* **79**(2), 293–297 (2012).
38. S. Hein, R. Petzold, M. Schoenthaler, U. Wetterauer, and A. Miernik, "Thermal effects of Ho: YAG laser lithotripsy: real-time evaluation in an in vitro model," *World J. Urol.* **36**(9), 1469–1475 (2018).
39. D. A. Wollin, E. C. Carlos, W. R. Tom, W. N. Simmons, G. M. Preminger, and M. E. Lipkin, "Effect of laser settings and irrigation rates on ureteral temperature during holmium laser lithotripsy, an in vitro model," *J. Endourol.* **32**(1), 59–63 (2018).
40. A. H. Aldoukhi, K. R. Ghani, T. L. Hall, and W. W. Roberts, "Thermal response to high-power holmium laser lithotripsy," *J. Endourol.* **31**(12), 1308–1312 (2017).
41. A. H. Aldoukhi, T. L. Hall, K. R. Ghani, A. D. Maxwell, B. MacConaghy, and W. W. Roberts, "Caliceal fluid temperature during high-power holmium laser lithotripsy in an in vivo porcine model," *J. Endourol.* **32**(8), 724–729 (2018).
42. W. R. Molina, I. N. Silva, R. Donalisio da Silva, D. Gustafson, D. Sehr, and F. J. Kim, "Influence of saline on temperature profile of laser lithotripsy activation," *J. Endourol.* **29**(2), 235–239 (2015).

INVESTIGATION OF OPTICAL PROPERTIES OF DISSECTED AND HOMOGENIZED BIOLOGICAL TISSUE

Maximilian Eisel, Stephan Ströbl, Thomas Pongratz, Herbert Stepp, Adrian Rühm, Ronald Sroka, J. Biomed. Opt. 23(9) 091418 (24 September 2018), <https://doi.org/10.1117/1.JBO.23.9.091418>, JIF: 2.367

Kurzfassung: Die Kenntnis der **optischen Eigenschaften** von biologischen **Geweben** ist eine Voraussetzung für viele lichtbasierte diagnostische und therapeutische Ansätze in der Medizin, wie beispielsweise die photodynamische Therapie (PDT) [122-124] oder Diagnostik (PDD) [125, 126], die Photokoagulation [127, 128] und fluoreszenzdiagnostische Verfahren [129, 130]. Die Bestimmung der optischen Eigenschaften, Absorption μ_a und reduzierter Streuung μ_s' , erfolgte in einem Wellenlängenbereich von λ : 520 nm – 800 nm durch **Ulbrichtkugelmessungen** über einen „Inverse Adding Doubling“-Algorithmus [131, 132] (IAD) und durch **ortsaufgelöste Remissionmessungen** [133, 134]. Diese beiden Messmethoden sind den indirekten photometrischen Techniken (dicke Probe, multiple interne Streuprozesse) zugehörig, hierbei werden die makroskopischen optischen Eigenschaften durch beispielsweise IAD oder Diffusionsnäherung anhand zuvor gemessener Größen (z.B. Remission, Reflexion, Transmission) bestimmt [135]. Gewebe vom Schwein (Gehirn, Leber, Lunge, Muskel) wurde innerhalb von 48 Stunden nach Schlachtung in 1 mm dicke Scheiben sezirt oder mit einem Pürierstab zu einer Paste verarbeitet (Homogenisierung) [136]. Biologische Gewebe weisen durch ihren komplexen internen Aufbau (verschiedene Zelltypen, Bindegewebe, Blutgefäße, etc.) eine heterogene Struktur auf [137-140]. Bei beiden hier verwendeten Messmethoden werden Vereinfachungen in Bezug auf die zu vermessende Probe, wie z.B. eine Homogenität der makroskopisch vorherrschenden optischen Eigenschaften, angenommen [127]. Die Vergleichbarkeit der Messergebnisse durch beide Messmethoden mit jeweils **sezirten** und **homogenisierten** Gewebeproben wurde untersucht, insbesondere welche Änderungen der optischen Eigenschaften durch den Homogenisierungsprozess entstehen. Die Probenverarbeitung und Präparation für die jeweiligen Messaufbauten war deutlich schneller und einfacher mit den homogenisierten Geweben im Vergleich zu den sezirten möglich. Zusätzlich ist die **Reproduzierbarkeit** ($n=5$) mit homogenisierten Proben erhöht, da interne Gewebestrukturen bei der Homogenisierung zerstört werden. Die Ergebnisse zeigten eine gute Übereinstimmung beider Präparationsmethoden für μ_s' . Der Absorptionskoeffizient μ_a hingegen wich, voraussichtlich durch Gleichverteilung zuvor lokalisierten Blutes in das Gesamtvolumen, von den Messwerten für sezirtes Gewebe teils deutlich ab. Zusammenfassend ist eine Homogenisierung, insbesondere von kleinen oder sehr heterogenen Proben, eine vielversprechende Methode zur *ex vivo* Präparation für zuvor genannte ausgewählte Anwendungen in der Medizin sein. Diese Datenbank an optischen Eigenschaften von biologischen Geweben kann als Grundlage für Berechnungen und Simulationen von Gewebe-Licht-Interaktionen herangezogen werden.

Der Anteil von Maximilian Eisel an dieser Arbeit war die Beschaffung und Verarbeitung/Präparation der Gewebeproben, sowie die Versuchsdurchführung und –auswertung. Eine Literaturrecherche und die Zusammenfassung in der hier präsentierten Publikation wurden ebenfalls durchgeführt. Besonderer Dank gilt an dieser Stelle dem Team der Metzgerei Weichart für die Bereitstellung der erforderlichen Gewebeproben.

Journal of Biomedical Optics

BiomedicalOptics.SPIEDigitalLibrary.org

Investigation of optical properties of dissected and homogenized biological tissue

Maximilian Eisel
Stephan Ströbl
Thomas Pongratz
Herbert Stepp
Adrian Rühm
Ronald Sroka

Investigation of optical properties of dissected and homogenized biological tissue

Maximilian Eisel,^{a,b,*} Stephan Ströbl,^{a,b} Thomas Pongratz,^{a,b} Herbert Stepp,^{a,b} Adrian Rühm,^{a,b} and Ronald Sroka^{a,b}

^aKlinikum der Universität München, Laser-Forschungslabor, LIFE-Zentrum, Munich, Germany

^bUniversity Hospital of Munich, Department of Urology, Munich, Germany

Abstract. Knowledge of tissue optical properties, in particular the absorption μ_a and the reduced scattering coefficient μ'_s , is required for diagnostic and therapeutic applications in which the light distribution during treatment has to be known. As it is generally very difficult to obtain this information with sufficient accuracy *in vivo*, optical properties are often approximately determined on *ex vivo* tissue samples. In this case, the obtained optical properties may strongly depend on the sample preparation. The extent of the expectable preparation-dependent differences was systematically investigated in comparative measurements on dissected and homogenized porcine tissue samples (liver, lung, brain, and muscle). These measurements were performed at wavelengths 520, 635, 660, and 785 nm, using a dual-step reflectance device and at a spectral range of 515 to 800 nm with an integrating sphere setup. In a third experiment, the density of tissue samples (dissected and homogenized) was investigated, as the characteristic of the packaging of internal tissue structures strongly influences the absorption and scattering. The standard errors of the obtained absorption and reduced scattering coefficients were found to be reduced in case of homogenized tissue. Homogenizing the tissues also allows a much easier and faster sample preparation, as macroscopic internal tissue structures are destroyed in the homogenized tissue so that a planar tissue sample with well-defined thickness can easily and accurately be prepared by filling the tissue paste into a cuvette. Consequently, a better reproducibility result was obtained when using homogenized samples. According to the density measurements accomplished for dissected and homogenized tissue samples, all types of tissues, except lung, showed a decrease in the density due to the homogenization process. The presented results are in good agreement for μ'_s regardless of the preparation procedure, whereas μ_a differs, probably influenced by blood content and dehydration. Because of faster and easier preparation and easier sample positioning, homogenization prior to measurement seems to be suitable for investigating the optical properties *ex vivo*. Additionally, by means of using the homogenization process, the sample size and thickness do not need to be particularly large, as is the case for most biopsies from the OR. © 2018 Society of Photo-Optical Instrumentation Engineers (SPIE) [DOI: 10.1117/1.JBO.23.9.091418]

Keywords: optical properties; biological tissue; spatially resolved reflectance; total diffuse reflectance; integrating sphere; density measurements.

Paper 170778SSPRRR received Dec. 1, 2017; accepted for publication Aug. 30, 2018; published online Sep. 24, 2018.

1 Introduction

Optical diagnostic and therapeutic applications usually depend on knowledge of the light distribution in the treated area, for instance in photodynamic therapy (PDT)^{1–3} and diagnosis (PDD),^{4,5} photocoagulation,^{6,7} and fluorescence diagnosis in general.^{8,9} The light distribution in turn depends on the optical tissue properties (μ_a , μ_s) and their distribution in space.^{10–12} There are several photometric techniques (direct and indirect) available for measurement of optical properties. Direct measurements (thin sample, single scattering events) focus on one particular microscopic coefficient and normally do not use a model for light propagation. Indirect methods (thick sample and multiple scattering) calculate the macroscopic optical parameters via an inverse model [inverse adding doubling (IAD), diffusion approximation] from measured quantities (e.g., diffuse/collimated reflection or transmission).¹³ The estimation of optical properties of extracted biological tissues is often performed by single- or double-integrating sphere (IS) technique.^{14–20} Another approach is to exploit the backscattered light from

a thick sample surface either for absolute measurement or spatially resolved evaluation.^{21–27} In a modified form, backscattered light can be also used for time resolved,²⁸ frequency domain,²⁹ and spatial-frequency domain³⁰ measurements, and finally also using OCT-technology.³¹ Furthermore, such techniques have the potential to be adjusted to clinical applications.

Biological tissue, however, does usually not show uniform optical properties within a macroscopic volume as it contains regions made up of different types of cells, connective tissue, vessels, and boundary layers, such as an organ capsule (serous membrane) or membranes.^{32–35} As well, natural degradation of the tissue samples and the related changes in pH, moisture, and oxygenation have to be taken into account.¹² Precise and reproducible slicing of the tissue to investigate the optical properties by IS techniques is challenging, and often the fixing compounds used in preparation must be taken into account.³⁶ Shredding the tissue causes most of its internal structures to be destroyed or more evenly distributed,¹⁰ thus creating a macroscopic volume with rather uniform optical properties. Although studies concerning the comparison of different measurement techniques

*Address all correspondence to: Maximilian Eisel, E-mail: Max.Eisel@med.uni-muenchen.de

are available and a lot of investigations into tissue mimicking phantoms (layered and homogenous) are performed,^{37–40} the influence of the structure of tissue sample on the optical properties has not been investigated systematically on biological samples so far. Thus, the objective of this investigation is the comparison of the optical properties measured on dissected, sliced tissue samples and their corresponding homogenized versions using the IS technique and a dual-step reflectance method (DSR). Both employed methods use mathematical approximations, like the radiative transfer equation, in combination with homogeneous optical tissue properties to calculate the optical properties from reflection or transmission measurements on the illuminated sample. These approximations often rely on simplifying assumptions about the investigated tissue volume, such as homogeneity of the optical tissue properties.⁶

In addition to evaluating whether the homogenizing process is suitable to obtain at least similar optical properties values by using dissected tissue samples, or whether the interference is too harsh to the tissue's structure, a simplification and thus time-saving aspect of the tissue preparation process accompanied by an increase of reproducibility should be tested. In particular the method of homogenizing is very interesting for small, heterogeneous, or traumatized samples from biopsies or resections (e.g., cholesteatoma⁴¹ and glioblastoma⁴²). As the optical properties of *ex vivo* samples highly depend on the storage conditions and further processing^{7,11,32,43} and may thus decidedly differ from those of *in vivo* tissue, future work should be focused on the relation between these two kinds of state of tissue conditions.

2 Materials and Methods

2.1 Samples and Sample Preparation

Measurements, performed on porcine brain, liver, lung, and muscle from the abattoir, were used within 48 h after sacrifice, representing heterogenic pasty, bloody, uncongested, and structured conditions, respectively. The samples were stored in a refrigerator in separated plastic containers at a temperature of 4°C until experiments. For DSR measurements, the tissue samples (dissected: \varnothing : ~40 mm; homogenized \varnothing : ~80 mm) were placed into plastic Petri dishes (\varnothing : 80 mm; height: 25 mm). A sample thickness of ~10 mm was chosen to prevent light interaction with the bottom of the Petri dish. An even sample surface was imperative for reproducible measurement results. Tissue homogenization¹⁰ was accomplished using a commercial hand blender (STUDIO St10, Sertronics GmbH, Saarlouis, Germany) for 2 min at ~12,000 rpm (power mode II). IS measurements were performed on samples dissected into rectangular slices with at least 30-mm edge length and a thickness of 1 mm. The tissue slices were positioned between two microscope slides (50 mm × 50 mm × 1 mm) separated by 1-mm-thick spacers. In this way, a squeezing of the sample between the glass slides was avoided and a defined thickness could be obtained to prevent an unwanted alteration of the scattering and absorption coefficients.^{6,32} The homogenized tissue paste was equally distributed on a glass slide and covered by a second glass slide with the 1-mm spacer in between. Careful positioning guaranteed minimal squeezing of the tissue paste.

The sample preparation (dissection/homogenizing) took place immediately before measurement, hence guaranteeing reproducible tissue conditions.

2.2 Experimental Setups

2.2.1 Dual-step reflectance measurement

The determination of optical properties was accomplished by (a) spectral measurement of the total diffuse reflectance of the tissue surface using a broadband white-light source and (b) detecting the spatially resolved diffuse reflectance from the tissue surface illuminated with a monochromatic laser beam in a sharply defined spot via a CCD camera. These two procedures were condensed to one setup, termed DSR setup. This setup is described in the following.

The spectral measurement of the total diffuse reflectance of the tissue surface was performed by perpendicular illumination of the sample surface by a halogen white-light source (Xenophot, Osram, Germany) coupled into an optical fiber ($\varnothing_{\text{core}}$: 1000 μm , NA: 0.37), as shown in Fig. 1. The achromatic lens ($f = 5 \text{ mm}$) at the distal end of the optical fiber ensures a uniform light distribution within a circular spot on the tissue surface ($\varnothing_{\text{spot}}$: 20 mm). The remitted light is collected by means of a second optical fiber ($\varnothing_{\text{core}}$: 600 μm , NA: 0.37), which is aligned under 45 deg with respect to the tissue surface. The polished flat end of this detection fiber is positioned at a distance of 50 mm to the intersection point of the fiber axis and the sample surface. To obtain correct results, it has to be ensured that the surface area from which remitted light is collected into the detection fiber is fully contained within the homogeneously illuminated spot on the tissue surface. The detection fiber guides the collected light to a spectrometer (S2000, Ocean Optics, Ostfildern, Germany). The spectrometer is sensitive in the spectral range from 200 to 850 nm. For each measurement a reference spectrum was taken, using a Lambertian reflectance standard (SG3060/7, \varnothing : 30 mm, reflectance: 30%, L.O.T. – Oriol GmbH & Co. KG, Darmstadt, Germany) using the same geometrical setup. The software OOIBASE (Ocean Optics, Dunedin, Florida) was used to visualize and save the respective spectra of sample and standard.

By measuring the remitted light intensities of the tissue sample (I_{sample} , I_{standard}) in comparison with the Lambertian remission standard R_s , the total diffuse reflectance R of the sample surface can be evaluated according to Eq. (1):

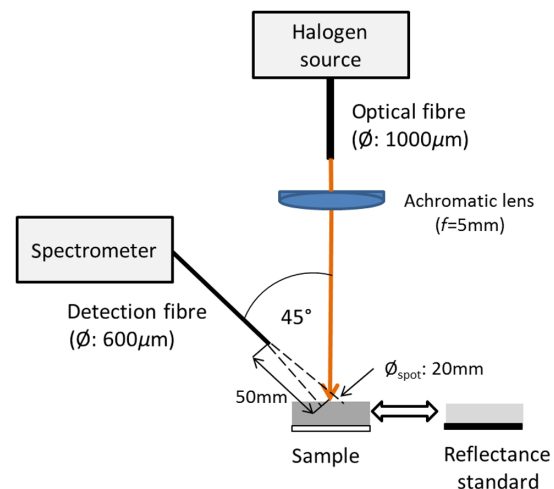


Fig. 1 Spectral total diffuse reflectance measurement setup comprising a fiber-coupled halogen lamp and a 45-deg inclined detection fiber attached to a spectrometer.

$$R = \frac{I_{\text{sample}}}{I_{\text{standard}}} \cdot R_{\text{standard}} \quad (1)$$

In approximation the following equation can be used:⁴⁴

$$R \approx \exp \left[-\frac{A(q)}{\sqrt{3(1 + \frac{1}{q})}} \right], \quad (2)$$

where

$$q = \frac{\mu_a}{\mu'_s}, \quad (3)$$

denotes the quotient of the sample's absorption and reduced scattering coefficient. The function $A(q)$ additionally depends on the relative refractive index $n_{\text{rel}} = \frac{n_{\text{surrounding}}}{n_{\text{sample}}}$, and can be determined by Monte Carlo simulations. By inverting Eq. (2) via lookup tables and interpolation, the quotient q can be calculated for any experimentally obtained values of R_d .

For the spatially resolved reflectance measurement, a monochrome CCD camera (SensiCam Long Exposure, PCO Computer Optics GmbH, Kelheim, Germany) was used to record the spatial intensity distribution on the sample surface while irradiated with a narrow laser beam. The employed setup allowed the determination of optical properties at four specific fixed wavelengths. For this purpose, four laser diodes (Flexpoint Dot, Laser Components, and Olching, Germany) were arranged annularly around the CCD camera and focused into one single spot, as can be seen in Fig. 2. The laser diodes emit at central wavelengths of 520, 635, 660, and 785 nm at a maximum optical power of 5 mW. The intersection point of all laser beams is located within the object plane of the camera. The measurement procedure was partially automated and implemented in a MATLAB code (MATLAB, The MathWorks Inc., Natick, Massachusetts).

The CCD camera takes an image of the tissue sample surface, while laser light of a single laser diode illuminates a small spot ($\varnothing: \ll 0.4$ mm) on the sample surface. The procedure is repeated for every laser diode wavelength; hence, one image is generated for every specific wavelength. For evaluation the radial dependence of the light intensity around the laser spot has to be measured; therefore, the light intensity is mapped as a function of the pixel distance from the center of the illuminated light spot.

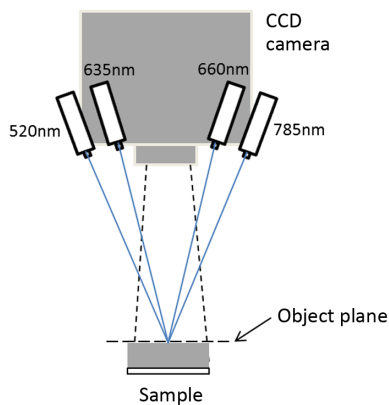


Fig. 2 Spatially resolved reflectance measurement setup comprising a CCD camera and four laser diodes emitting at central wavelengths 520, 635, 660, and 785 nm.

To increase the dynamic range of the remitted light distribution, suitable measures must be taken such that almost every pixel contains a signal clearly distinguishable from the background. To achieve this, images of the light distribution are taken by gradually increasing the integration time of the camera from a minimum value (2 ms), where no pixels are saturated, to a maximum value (5000 ms). Through this step-by-step increase of the integration time, more and more pixels near the spot center become saturated, whereas more and more pixels far from the spot center provide a signal well distinguishable from the background. When considering only unsaturated pixels with signals well above the background and averaging over all respective time-normalized intensities in each of these pixels, a combined gray-scale image with an enhanced dynamic range can be generated. By binning of its pixels into suitably chosen intervals of radial distance from the illumination spot center and averaging over the signal intensities in each bin, a graph of the averaged radial dependence of the diffusely remitted light intensity can be constructed. The sample's effective attenuation coefficient,

$$\mu_{\text{eff}} = \sqrt{3\mu_a(\mu_a + \mu'_s)}, \quad (4)$$

can then be determined by fitting a model curve to this graph, based on Monte Carlo simulations with preset values for the scattering anisotropy $g(\lambda_n)$, the refractive index $n_{\text{sample}}(\lambda_n)$ of the sample, and the value $q(\lambda_n)$ determined from the total diffuse reflectance measurements for the respective (laser) wavelength λ_n as described above.^{45,46}

2.2.2 Integrating sphere setup

The determination of the optical properties using the integrating sphere (IS) was performed, among others, by the indirect spectral measurement of diffuse reflected and transmitted light intensities during illumination of a tissue sample by a white-light source. Subsequently, an IAD procedure^{47,48} can be used to evaluate the optical properties μ_a and μ'_s , provided that the scattering anisotropy g is predefined. Figure 3 shows exemplarily the setup for the measurement of the diffuse transmitted light.

A xenon arc lamp (D-light, Karl Storz, Tuttlingen, Germany) was coupled into a multimode optical fiber ($\varnothing_{\text{core}}$: 1.5 mm, NA: 0.37). At the distal end of the fiber the light passes an iris, which was used to adjust the beam diameter and to reduce stray light. A lens (f : 60 mm) focuses the beam onto the sample. Between the distal fiber end and the first iris, a shutter is located and can be used to perform dark measurements for background corrections. The IS (\varnothing : 101.6 mm, Labsphere North Sutton) is coated with Spectralon[®], which has a reflectivity of about 99% in the spectral range from 400 to 1500 nm. The reflected or transmitted diffuse light is detected in the spectral range from 200 to 850 nm via an optical fiber ($\varnothing_{\text{core}}$: 500 μm , NA: 0.3) attached to a spectrometer (S2000, Ocean Optics, Dunedin) by collecting stray light from the sphere surface within the fiber's numerical aperture.

The spectral determination of the optical properties μ_a and μ'_s of a tissue sample was performed by calculating the diffuse transmission T_d and the diffuse reflectance R_d out of three spectral measurements in counts/ms (Sig_{Td} , Sig_{Rd} , and Sig_{Ref}) in the wavelength range between 400 and 800 nm. The device configurations during the three spectral measurements are shown in Fig. 4.

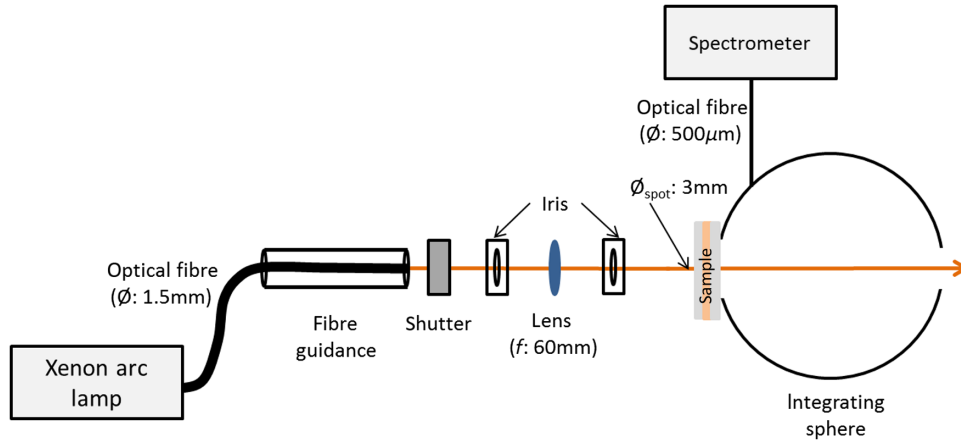


Fig. 3 Schematic setup for the measurement of the diffuse transmitted light passing the sample. Collimated transmitted light leaves the sphere without any interaction.

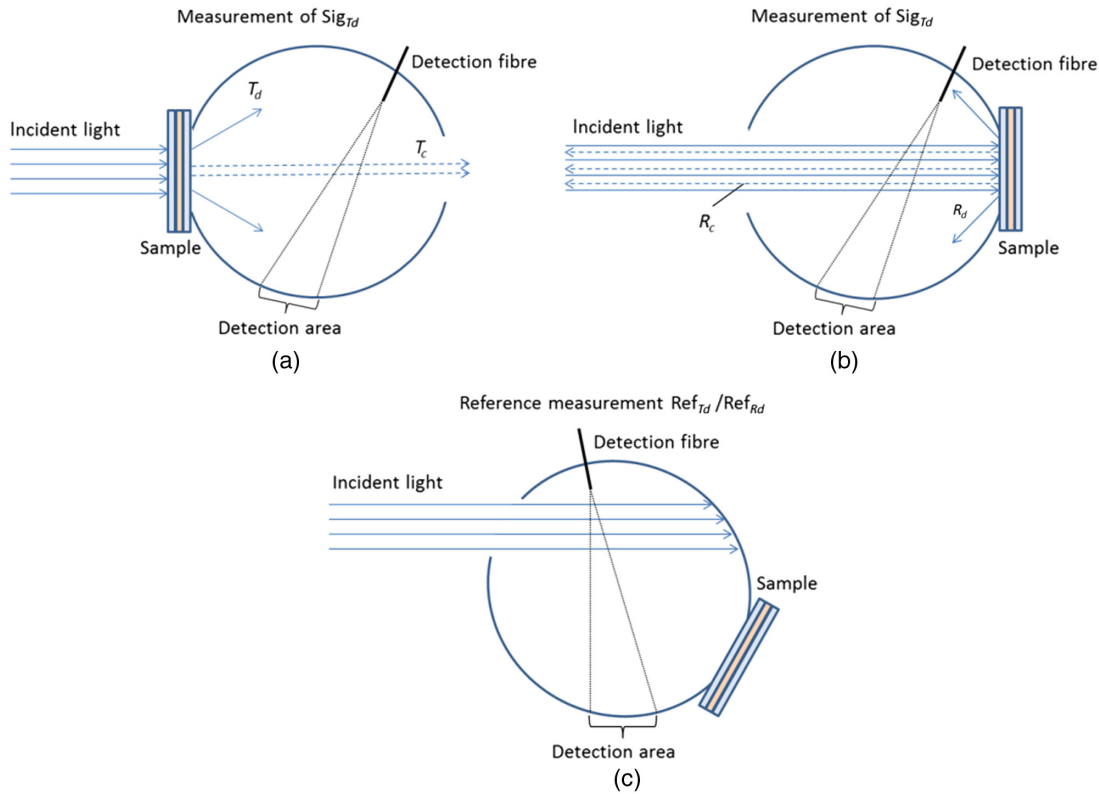


Fig. 4 Top view of the IS for the measurements of (a) Sig_{Td} , (b) Sig_{Rd} , and (c) Sig_{Ref} .

Due to the low collimated transmission signal, it was not possible to determine the anisotropy factor g , which would otherwise be possible with an extended set of measurements (not shown here). As a consequence, μ_s could not be calculated independently; hence, constant literature values were allocated to the scattering anisotropy g and the refractive indices n_{sample} of the sample, namely 0.8⁴³ and 1.37,^{49,50} respectively. Dark spectra (Bg_{Td} , Bg_{Rd} , and Bg_{Ref}) were taken and subtracted from the signals as background noise. T_d and R_d can be calculated by the following Eqs. (5) and (6):

$$T_d = \frac{\text{Sig}_{Td} - \text{Bg}_{Td}}{\text{Sig}_{Ref} - \text{Bg}_{Ref}} \cdot R_{\text{sphere}}, \quad (5)$$

$$R_d = \frac{\text{Sig}_{Rd} - \text{Bg}_{Rd}}{\text{Sig}_{Ref} - \text{Bg}_{Ref}} \cdot R_{\text{sphere}}. \quad (6)$$

The variable R_{sphere} represents the wavelength depending reflectance of the IS's inner coating Spectralon®. Using the inverse adding doubling method established by Prahl et al.,^{47,48} the optical properties μ_a and μ'_s can then be computed from T_d and R_d .

2.2.3 Tissue density measurements

Mass density measurements were performed on dissected and homogenized tissue samples to identify potential density

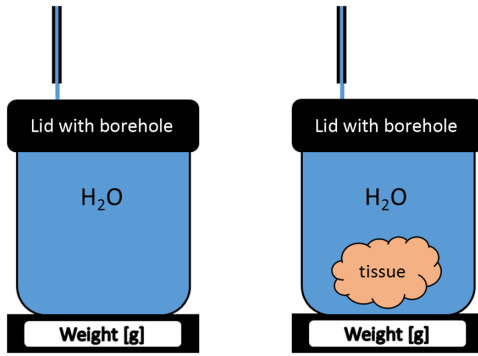


Fig. 5 Experimental setup for density measurement of biological tissue.

changes during the homogenizing process as these may be linked to optical property changes. For every tissue, $n = 5$ density measurements were performed, whereby sample volumes of at least 1 cm^3 were used. For that purpose, a vessel placed on top of a scale (BP 310 S, Sartorius, Göttingen, Germany) (Fig. 5) was filled with water and the corresponding volume (V_w) was determined. Thereupon the vessel was emptied, a volume of tissue had been prepared, its mass m_{sample} had been determined, and then inserted into the vessel, and the scale tared. By filling the vessel with water, the reduced volume V_r can be estimated. The water volume displaced by the sample volume V_{sample} can then be calculated as $\Delta V = V_w - V_r$. The tissue density can then be calculated according to the equation [Eq. (7)] as

$$\rho_{\text{sample}} = \frac{m_{\text{sample}}}{V}. \quad (7)$$

2.3 Data Analysis

The data analysis and representation were performed using Sigma Plot (V.11.0, Systat Software GmbH, Erkrath, Germany). For brevity, abbreviations were used for the four combinations of experimental method and tissue preparation as follows: for the IS setup I and ID in combination with dissected tissue, respectively, IH in combination with homogenized tissue; for the DSR setup R and RD and RH, respectively.

Optical properties were determined for each of the four experiment/preparation combinations, each of the four different laser wavelengths of the DSR setup, and each of the four different tissue types. In each case, the obtained optical properties are graphically represented by mean values (μ_{mean}) out of $n = 5$ measurements, while the error bars represent the corresponding standard errors (μ_{err}). As the IS measurements were performed with a broadband white-light source, the results are shown as full spectra (515 to 800 nm) with error bars at the DSR wavelength positions. The relative standard error, i.e., the ratio of the standard error and the mean value, was evaluated in percent in each case. Afterward, the ratio of the relative standard error for homogenized and dissected tissue was calculated for each case, i.e., for each experimental method, for each wavelength λ , and for each of the four tissue types:

$$(r\lambda; \text{IS}) = \frac{\mu_{\text{err}}(\lambda; \text{IH})/\mu_{\text{mean}}(\lambda; \text{IH})}{\mu_{\text{err}}(\lambda; \text{ID})/\mu_{\text{mean}}(\lambda; \text{ID})}, \quad (8)$$

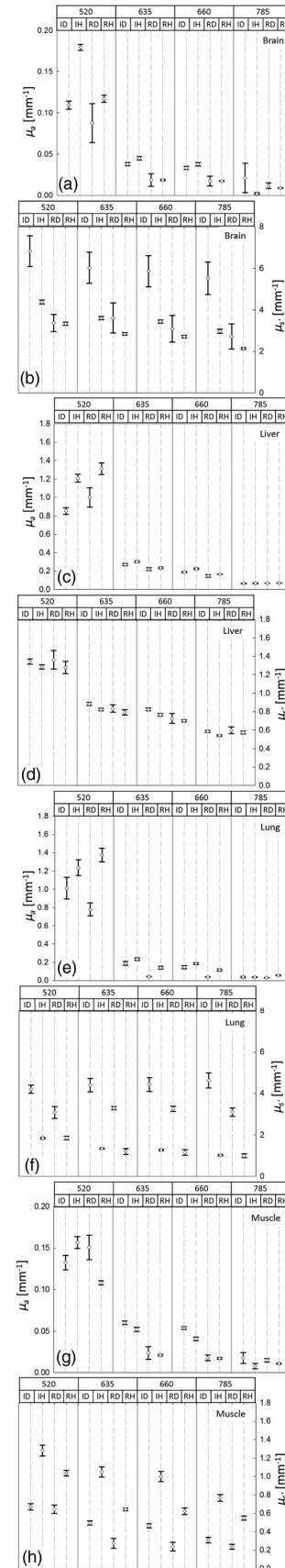


Fig. 6 Optical properties of dissected (ID and RD) and homogenized (IH and RH) brain tissue samples, for the wavelengths 520, 635, 660, and 785 nm. [mean \pm stderr ($n = 5$)]. (a) Brain tissue: μ_a , (b) μ_s . (c) Liver: μ_a , (d) μ_s . (e) Lung: μ_a , (f) μ_s . (g) Muscle: μ_a , (h) μ_s .

$$r(\lambda; \text{DSR}) = \frac{\mu_{\text{err}}(\lambda; \text{RH})/\mu_{\text{mean}}(\lambda; \text{RH})}{\mu_{\text{err}}(\lambda; \text{RD})/\mu_{\text{mean}}(\lambda; \text{RD})}. \quad (9)$$

A ratio value $r < 1$ indicates a smaller relative standard error in case of homogenized compared with dissected tissue. Ratio values $r > 1$ indicate that the dissected tissue samples showed smaller relative standard errors. A reference line at $r = 1$ was included in each of these graphs for clarity.

3 Results

3.1 Optical Property Measurements

The optical properties obtained for each experiment/preparation combination at the four different wavelengths of the DSR setup are shown in Figs. 6(a)–6(h) for each tissue type (brain, liver, lung, and muscle). The absorption coefficient μ_a is shown in the left column, the reduced scattering coefficient μ'_s in the right column.

In most cases, the absorption coefficient μ_a was found to be higher for homogenized tissues (IH and RH) than for the corresponding dissected tissues (ID and RD). Muscle tissue [Fig. 6(g)] shows the opposite behavior, except at 520 nm,

where the IS measurements again yielded a higher μ_a value for homogenized tissue (IH versus ID). Overall, in almost all measurements, the relative standard error decreased using homogenized tissue samples instead of dissected ones.

IS measurements on brain tissue [Fig. 6(b)] (and liver tissue [Fig. 6(d)], with lower significance) yield smaller values for μ'_s in case of homogenized samples. Independent of the experimental method, the same holds for lung tissue [Fig. 6(f)], whereas the opposite behavior is obtained for muscle tissue [Fig. 6(h)]. DSR measurements on brain and liver tissue did not yield significant differences between dissected and homogenized tissue.

For liver tissue, the differences between dissected and homogenized tissue are generally very small, except at a wavelength of 520 nm [Figs. 6(c) and 6(d)].

The comparison of the ratio of relative standard errors of homogenized and the corresponding dissected tissue samples is shown in Fig. 7. The ratio values obtained from IS measurements are shown in the left column, for μ_a in the upper, and μ'_s in the lower graph. The corresponding results obtained from DSR measurements are shown in the right column. As can be seen, the relative standard error for μ'_s was in most cases smaller ($r < 1$) than in the case of homogenized samples, except for lung tissue. For μ_a around one-third of the values were larger

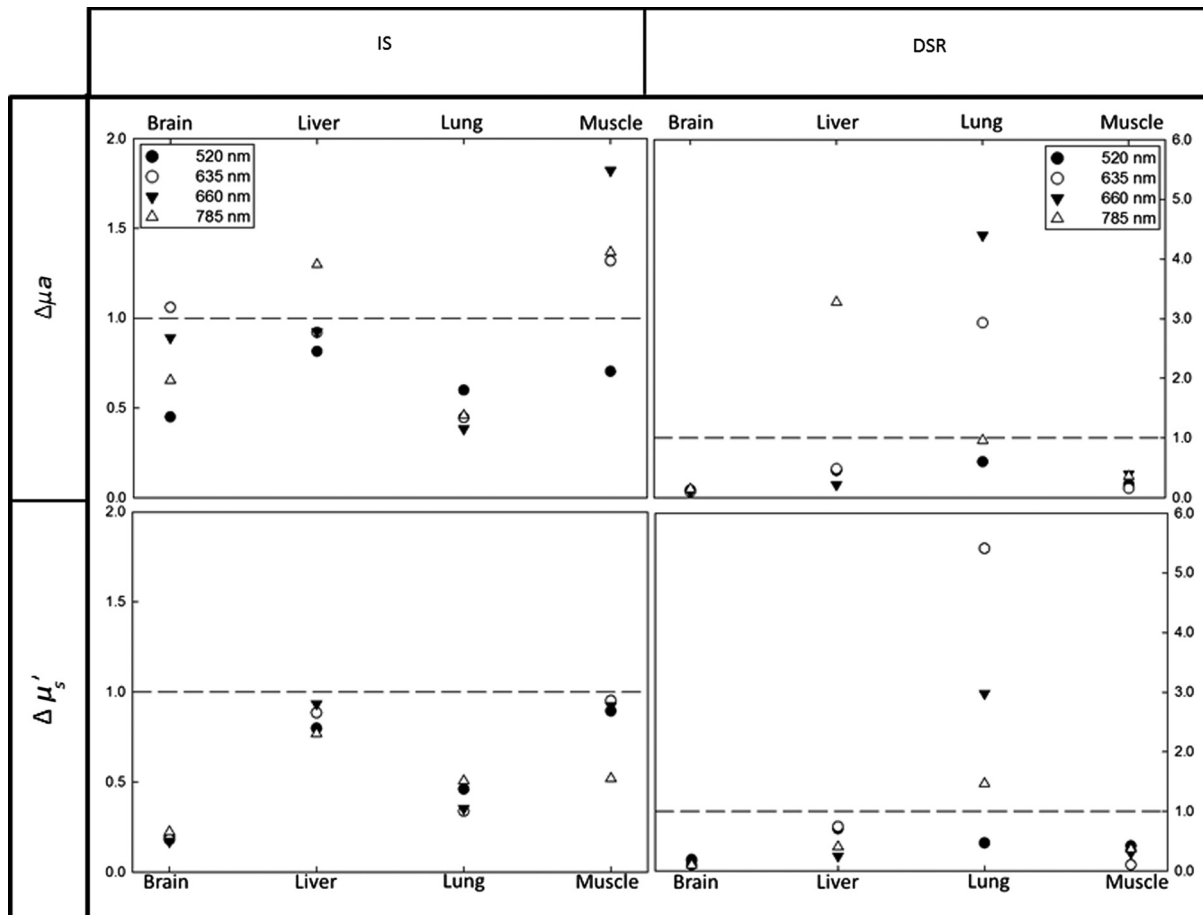


Fig. 7 Ratio of relative standard errors between homogenized and the corresponding dissected tissue samples, plotted for the absorption coefficient and the reduced scattering coefficient in the upper and lower graphs, respectively. Results are shown for the four different source tissues and the four different laser wavelengths of the DSR setup, where results from IS and DSR measurements are collected in the left and right columns, respectively. A ratio value < 1 indicates a smaller relative standard error in case of homogenized tissue. Ratio values > 1 indicate that the dissected tissue samples showed smaller relative standard errors.

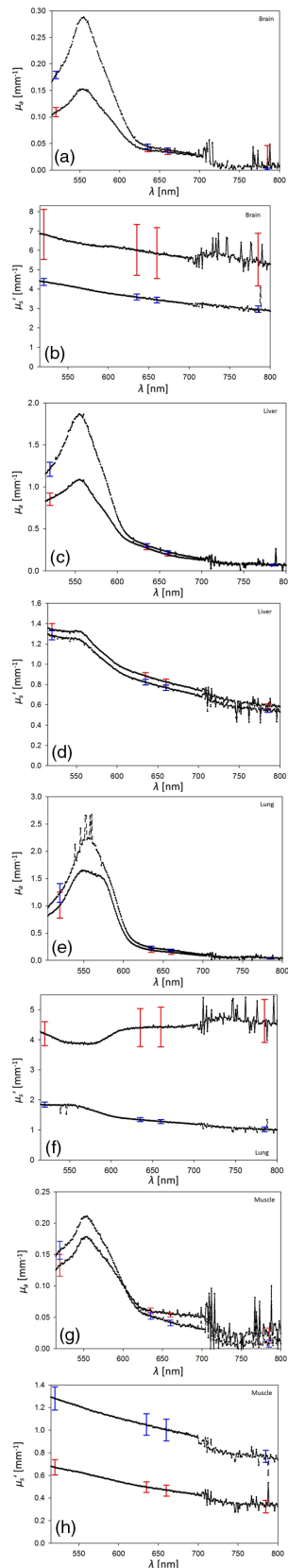


Fig. 8 Mean values ($n = 5$) of the absorption and scattering spectra of the IS measurements (515 to 800 nm). Dissected tissue (solid line) is illustrated with red colored error bars at the DSR wavelength, homogenized samples (interrupted line) with blue error bars at the same wavelength positions, respectively. (a) Brain tissue: μ_a , (b) μ_s' . (c) Liver: μ_a , (d) μ_s' . (e) Lung: μ_a , (f) μ_s' . (g) Muscle: μ_a , (h) μ_s' .

Table 1 The results of the tissue density measurements.

	Homogenized ρ (g/cm ³)	Dissected ρ (g/cm ³)	Literature dissected ρ (g/cm ³)
Brain	0.962 to 0.969	1.028 to 1.038	1.030 to 1.041
Liver	1.025 to 1.045	1.068 to 1.082	1.050 to 1.070
Lung	1.012 to 1.018	0.462 to 0.498	0.230 to 1.092
Muscle	1.023 to 1.039	1.069 to 1.093	1.038 to 1.056

($r > 1$) than one and hence had smaller relative standard errors for dissected tissue.

The IS mean values ($n = 5$) for the absorption and scattering coefficient for both preparation methods derived from IS investigations (mean of $n = 5$) in the spectral range from 515 to 800 nm are shown in Figs. 8(a)–8(h). Measurements performed with dissected tissue are displayed as solid lines with red colored error bars at the DSR wavelength positions, for homogenized samples interrupted lines and blue error bars were used. Absorption coefficients [Figs. 8(a), 8(c), 8(e), and 8(g)] are increased for homogenized tissue samples in comparison with dissected in the spectral range of 515 to 580 nm, and become aligned from 580 to 800 nm. The scattering coefficient values for homogenized samples mostly lay below the ones for dissected [Figs. 8(b), 8(d), and 8(f)], except for muscle [Fig. 8(h)]. The smallest deviation depending on preparation method could be observed for liver [Fig. 8(d)]; additionally, the revealed results for absorption and reduced scattering are in good relation to Roggan et al.⁴³ In the most graphs, except for μ_s' [Fig. 8(h)] and μ_a [Fig. 8(g)] of muscle tissue, the standard deviations were smaller or at least very similar in comparison with the error bars of dissected tissue. This agrees very well with the results of the relative errors of the IS measurements shown in Fig. 7.

3.2 Tissue Density Measurements

The results of the tissue density measurements are listed in Table 1 and compared with literature values.⁵¹ In the case of lung tissue, the obtained results were compared with both deflated and inflated lung tissue; in the case of muscle tissue, to skeletal muscle tissue. For all types of tissue, except lung, a decrease in the mass density was observed upon homogenization. The values for dissected tissue correspond well with the literature data.

4 Discussion

The optical properties of different types of homogenized and dissected porcine tissue samples (brain, liver, lung, and muscle) were determined using IS and DSR measurements. In the case of homogenized tissue, a reduction in the relative standard error of the obtained optical coefficients was observed, which can be attributed to an improved reproducibility of the experiments. Furthermore, the improved reproducibility can be attributed to the destruction of internal tissue structures, so that extreme local changes³³ in the optical properties of the specific tissue sample can be overcome. This seems to be a fact for all tissues investigated except for lung samples (Fig. 7), which might be traced back to incomplete homogenizing within the 2 min shredding. Overall, using homogenized tissue samples, the

preparation of the samples was much easier, and the performance of the experiments was less time consuming. All in all, homogenization of tissues for *ex vivo* experiments using standard setups like IS or diffuse reflectance analysis seems to be a promising way to create stable and reproducible datasets of the optical properties of different tissues. However, one has to consider whether the gained results of such a methodology are suitable for the particular clinical application.

It can be derived that the absorption coefficient is increased for homogenized tissue samples in comparison with the corresponding sliced tissue, which can be explained by a more even distribution of blood cells within the tissue sample. Red blood cells are one of the main absorbers in tissues,⁷ whereby the increased μ_a values in the spectral range of 500 to 580 nm can be explained.^{43,52} In contrast to the dissected samples, where blood is concentrated in certain areas and vessels, the blood will be spread fairly evenly over the whole sample volume upon homogenization. This may lead to a higher μ_a from 400 to 600 nm as seen in the IS spectral data [Figs. 8(a), 8(c), 8(e), and 8(g)] and can be related to an effect known as pigment packaging.⁵³ Equally, the destruction of internal structures changes the scattering coefficient in comparison with the sliced sample due to altering of local nonuniformities in the microstructure, e.g., the size, shape, and orientation as well as the refractive index mismatch of the scattering particles.⁵⁴

The homogenization process also raises issues like how the changes in tissue morphology, namely the introduction or extraction of air, in addition to the redistribution of tissue fluids or other tissue constituents, may influence the absorption and scattering coefficients measurable on the sample.⁵⁴ Therefore, mass density measurements were performed additionally to assess the extent of such morphological changes induced by the used tissue homogenization procedure.

Within the experimental errors, the measured mass densities of the dissected tissue samples were quite consistent with the corresponding literature values. The wide range of literature values in the case of lung tissue can be explained by the potentially high air content in the tissue. For full inflation, densities around 0.23 g/cm³ are found in the literature, whereas for deflation the density is reported to increase to around 1.09 g/cm³. The performed density measurements on dissected lung tissue yielded values of around 0.480 g/cm³, which is intermediate between the two extreme values reported in the literature.⁵¹

In all cases, despite lung tissue, homogenizing of the tissue samples lead to a decrease in density. This might be explained by destroying denser structures and simultaneously inserting air into the sample due to the mixing procedure. Such an effect could potentially be avoided by performing the homogenization in vacuum. Lung tissue, on the other hand, becomes a lot denser (from 0.480 to 1.015 g/cm³) upon homogenization, which might be due to a removal or destruction of the air inclusions in the lung tissue. In the case of muscle tissue, the opposite effect is observed, whereby rather well-aligned supporting structures within muscle tissue are destroyed; upon homogenization, these “boundaries” are strongly disturbed so that they strongly scatter the impinging light.^{18,33,52} The performed tissue preparation may affect the determined optical properties. Although the destruction of the structure may influence the absorption and reduced scattering coefficient, packaging effects and blood distribution may alter mainly the absorption coefficient, and the preparation related density changes may have influences on both parameters.

The advantages tissue homogenization compared to tissue slices is that even small samples become usable for the determination of its optical properties. This applies especially to the IS measurement technique, where the sample size and thickness do not need to be particularly large.⁵⁵ Hence, after homogenizing the tissue, a thin layer of the disintegrated tissue can be spread between two glass slides whose distance can be quite small. One only has to ensure that the sample port is fully covered and that the sample is not squeezed. Regarding experimental aspects, homogenization allows for a much faster and easier sample preparation, due to the fact that no preparation time is required for a suitable tissue dissection aiming for an increase in reproducibility of the optical property data.

5 Conclusion

The optical properties of tissue samples were investigated and compared for homogenized versus dissected tissues. The comparison of the data showed good agreement for μ'_s , while the μ_a differences were probably influenced by blood. Experiments using homogenized tissue samples show high reproducibility and are less time consuming. Further investigations should be performed to statistically proof the statement.

Disclosures

The authors have no financial interests in this article and no potential conflicts of interest to disclose. All tissues were received from local abattoir. Thus, no animal experiments were performed and no animal was sacrificed especially for the experiments. In principle, the tissues examined are generally sold for public consume.

Acknowledgments

This manuscript was part of the inaugural thesis of Maximilian Eisel to be submitted at the Medical Faculty of the Ludwig-Maximilians-Universität, Munich.

References

1. D. E. Dolmans, D. Fukumura, and R. K. Jain, “Photodynamic therapy for cancer,” *Nat. Rev. Cancer* **3**(5), 380–387 (2003).
2. T. J. Dougherty et al., “Photodynamic therapy,” *J. Natl. Cancer Inst.* **90**(12), 889–905 (1998).
3. H. I. Pass, “Photodynamic therapy in oncology: mechanisms and clinical use,” *J. Natl. Cancer Inst.* **85**(6), 443–456 (1993).
4. M. Burger et al., “Photodynamic diagnostics and noninvasive bladder cancer: is it cost-effective in long-term application? A Germany-based cost analysis,” *Eur. Urol.* **52**(1), 142–147 (2007).
5. S. Denzinger and M. Burger, “Photodynamic diagnostics of bladder tumors,” *Curr. Urol. Rep.* **9**(2), 101–105 (2008).
6. E. K. Chan et al., “Effects of compression on soft tissue optical properties,” *IEEE J. Sel. Top. Quantum Electron.* **2**(4), 943–950 (1996).
7. S. L. Jacques, “Optical properties of biological tissues: a review,” *Phys. Med. Biol.* **58**(11), R37–R61 (2013).
8. S. Andersson-Engels et al., “In vivo fluorescence imaging for tissue diagnostics,” *Phys. Med. Biol.* **42**(5), 815–824 (1997).
9. J. Hegyi et al., “New developments in fluorescence diagnostics,” *J. Dtsch Dermatol. Ges.* **9**(5), 368–372 (2011).
10. D. W. Burden, “Guide to the disruption of biological samples-2012,” *Random Primers* **12**(12), 1–25 (2012).
11. E. Salomatina and A. N. Yaroslavsky, “Evaluation of the in vivo and ex vivo optical properties in a mouse ear model,” *Phys. Med. Biol.* **53**(11), 2797–2807 (2008).
12. Y. Peng and S. Dhakal, “Optical methods and techniques for meat quality inspection,” *Trans. Am. Soc. Agric. Biol. Eng.* **58**, 1371 (2015).

13. A. Kim and B. C. Wilson, "Measurement of ex vivo and in vivo tissue optical properties: methods and theories," in *Optical-Thermal Response of Laser-Irradiated Tissue*, A. J. Welch and M. J. C. Van Gemert, Eds., pp. 267–319, Springer, Dordrecht, Netherlands (2010).
14. J. F. Beek et al., "In vitro double-integrating-sphere optical properties of tissues between 630 and 1064 nm," *Phys. Med. Biol.* **42**(11), 2255–2261 (1997).
15. J. W. Pickering et al., "Double-integrating-sphere system for measuring the optical properties of tissue," *Appl. Opt.* **32**(4), 399–410 (1993).
16. T. L. Troy and S. N. Thennadil, "Optical properties of human skin in the near infrared wavelength range of 1000 to 2200 nm," *J. Biomed. Opt.* **6**(2), 167–176 (2001).
17. A. N. Yaroslavsky et al., "Optical properties of selected native and coagulated human brain tissues in vitro in the visible and near infrared spectral range," *Phys. Med. Biol.* **47**(12), 2059–2073 (2002).
18. B. Aernouts et al., "Effect of ultrasonic homogenization on the Vis/NIR bulk optical properties of milk," *Colloids Surf., B* **126**, 510–519 (2015).
19. A. López-Maestresalas et al., "Bulk optical properties of potato flesh in the 500–1900 nm range," *Food Bioprocess Technol.* **9**(3), 463–470 (2016).
20. Y. Villanueva, C. Veenstra, and W. Steenbergen, "Measuring absorption coefficient of scattering liquids using a tube inside an integrating sphere," *Appl. Opt.* **55**(11), 3030–3038 (2016).
21. F. Foschum, M. Jäger, and A. Kienle, "Fully automated spatially resolved reflectance spectrometer for the determination of the absorption and scattering in turbid media," *Rev. Sci. Instrum.* **82**(10), 103104 (2011).
22. F. Foschum and A. Kienle, "Broadband absorption spectroscopy of turbid media using a dual step steady-state method," *J. Biomed. Opt.* **17**(3), 037009 (2012).
23. S. Jacques, "Video reflectometry to specify optical properties of tissue in vivo," *Proc. SPIE* **10311**, 103110D (1993).
24. A. Kienle et al., "Spatially resolved absolute diffuse reflectance measurements for noninvasive determination of the optical scattering and absorption coefficients of biological tissue," *Appl. Opt.* **35**(13), 2304–2314 (1996).
25. A. Wang, R. Lu, and L. Xie, "Improved algorithm for estimating the optical properties of food products using spatially-resolved diffuse reflectance," *J. Food Eng.* **212**, 1–11 (2017).
26. J. J. Xia et al., "Characterizing beef muscles with optical scattering and absorption coefficients in VIS-NIR region," *Meat Sci.* **75**(1), 78–83 (2007).
27. R. L. P. van Veen et al., "Determination of VIS-NIR absorption coefficients of mammalian fat, with time- and spatially resolved diffuse reflectance and transmission spectroscopy," in *Biomedical Topical Meeting*, Miami Beach, Florida, Optical Society of America (2004).
28. M. S. Patterson, B. Chance, and B. C. Wilson, "Time resolved reflectance and transmittance for the noninvasive measurement of tissue optical properties," *Appl. Opt.* **28**(12), 2331–2336 (1989).
29. M. S. Patterson et al., "Frequency-domain reflectance for the determination of the scattering and absorption properties of tissue," *Appl. Opt.* **30**(31), 4474–4476 (1991).
30. E. R. Anderson, D. J. Cuccia, and A. J. Durkin, "Detection of bruises on golden delicious apples using spatial-frequency-domain imaging," *Proc. SPIE* **6430**, 64301O (2007).
31. A. I. Kholodnykh et al., "Precision of measurement of tissue optical properties with optical coherence tomography," *Appl. Opt.* **42**(16), 3027–3037 (2003).
32. V. V. Tuchin, *Optical Clearing of Tissues and Blood*, SPIE Press, Bellingham, Washington (2006).
33. E. A. Genina et al., "Effect of storage conditions of skin samples on their optical characteristics," *Opt. Spectrosc.* **107**(6), 934–938 (2009).
34. D. B. MacDougall, "Changes in the colour and opacity of meat," *Food Chem.* **9**(1), 75–88 (1982).
35. B. M. Nicolaï et al., "Nondestructive measurement of fruit and vegetable quality by means of NIR spectroscopy: a review," *Postharvest Biol. Technol.* **46**(2), 99–118 (2007).
36. A. Pitzschke et al., "Optical properties of rabbit brain in the red and near-infrared: changes observed under in vivo, postmortem, frozen, and formalin-fixed conditions," *J. Biomed. Opt.* **20**(2), 025006 (2015).
37. K.-B. Sung et al., "Accurate extraction of optical properties and top layer thickness of two-layered mucosal tissue phantoms from spatially resolved reflectance spectra," *J. Biomed. Opt.* **19**(7), 077002 (2014).
38. N. Honda et al., "Optical properties of tumor tissues grown on the chorioallantoic membrane of chicken eggs: tumor model to assay of tumor response to photodynamic therapy," *J. Biomed. Opt.* **20**(12), 125001 (2015).
39. M. S. Wróbel et al., "Nanoparticle-free tissue-mimicking phantoms with intrinsic scattering," *Biomed. Opt. Express* **7**(6), 2088–2094 (2016).
40. M. S. Wróbel et al., "Measurements of fundamental properties of homogeneous tissue phantoms," *J. Biomed. Opt.* **20**(4), 045004 (2015).
41. H. Sajjadi, "Endoscopic middle ear and mastoid surgery for cholesteatoma," *Iranian J. Otorhinolaryngol.* **25**(71), 63–70 (2013).
42. D. W. Roberts and J. Olson, "Fluorescein guidance in glioblastoma resection," *New Engl. J. Med.* **376**(18), e36 (2017).
43. A. Roggan et al., "The effect of preparation technique on the optical parameters of biological tissue," *Appl. Phys. B* **69**(5), 445–453 (1999).
44. S. Doizi and O. Traxer, "Re: evaluation of a novel single-use flexible ureteroscope," *Eur. Urol.* **72**(1), 152–153 (2017).
45. M. Pilz, S. Honold, and A. Kienle, "Determination of the optical properties of turbid media by measurements of the spatially resolved reflectance considering the point-spread function of the camera system," *J. Biomed. Opt.* **13**(5), 054047 (2008).
46. T. J. Beck et al., "Clinical determination of tissue optical properties in vivo by spatially resolved reflectance measurements," in *Photon Migration and Diffuse-Light Imaging*, Munich, Optical Society of America (2003).
47. S. Prah, "Optical property measurements using the inverse adding doubling program," (2011).
48. S. A. Prah, M. J. C. van Gemert, and A. J. Welch, "Determining the optical properties of turbid media by using the adding-doubling method," *Appl. Opt.* **32**(4), 559–568 (1993).
49. F. P. Bolin et al., "Refractive index of some mammalian tissues using a fiber optic cladding method," *Appl. Opt.* **28**(12), 2297–2303 (1989).
50. J. J. Dirckx, L. C. Kuypers, and W. F. Decraemer, "Refractive index of tissue measured with confocal microscopy," *J. Biomed. Opt.* **10**(4), 44014 (2005).
51. F. A. Duck, *Physical Properties of Tissues: A Comprehensive Reference Book*, Academic Press Inc., San Diego, California (1990).
52. D. Cozzolino, D. De Mattos, and D. V. Martins, "Visible/near infrared reflectance spectroscopy for predicting composition and tracing system of production of beef muscle," *Anim. Sci.* **74**(3), 477–484 (2002).
53. J. C. Finlay and T. H. Foster, "Effect of pigment packaging on diffuse reflectance spectroscopy of samples containing red blood cells," *Opt. Lett.* **29**(9), 965–967 (2004).
54. R. Van Beers et al., "Evolution of the bulk optical properties of bovine muscles during wet aging," *Meat Sci.* **136**, 50–58 (2018).
55. E. Chan, T. Menovsky, and A. J. Welch, "Effects of cryogenic grinding on soft-tissue optical properties," *Appl. Opt.* **35**(22), 4526–4532 (1996).

Maximilian Eisel began his studies in applied physics at the University of Applied Sciences Munich after finishing school in 2009, and finished his bachelor degree after completing his thesis at Truma GmbH in 2014. Afterwards he received his master's degree in photonics at the University of Applied Sciences in 2016, by finishing his master's thesis at the Laser-Forschungslabor (LFL) in the LIFE-Center of the University Hospital of Munich. Since, that time he is a PhD student at the LFL working on investigations to improve clinical laser induced lithotripsy.

Ronald Sroka is the head of the LFL at the LIFE-Center of the University Hospital of Munich. He is mostly engaged in the research and development of fluorescence diagnosis, photodynamic therapy and laser surgery in nearly all medical disciplines focusing on the translational technical implementation of several laser applications into the clinics. He is the general secretary of the German Society of Lasermedicine (DGLM e.V.) and executive member of the ELA. Since 2015, he is adjunct professor and advisory board member of the Institute of Photomedicine Tongji-University Shanghai.

Biographies for the other authors are not available.

LITERATURVERZEICHNIS

1. A. Pietropaolo, S. Proietti, R. Geraghty, et al., "*Trends of 'urolithiasis: interventions, simulation, and laser technology' over the last 16 years (2000–2015) as published in the literature (PubMed): a systematic review from European section of Uro-technology (ESUT)*". World Journal of Urology, 2017. **35**(11): p. 1651-1658.
2. N. Velázquez, D. Zapata, H.-H. S. Wang, et al., "*Medical expulsive therapy for pediatric urolithiasis: Systematic review and meta-analysis*". Journal of Pediatric Urology, 2015. **11**(6): p. 321-327.
3. S. A. M. Michaelis, K. D. Kalache, 25 - *Biliary Anomalies*, in *Obstetric Imaging: Fetal Diagnosis and Care (Second Edition)*, J.A. Copel, et al., Editors. 2018, Elsevier. p. 105-111.e101.
4. M. U. Baumann, B. Tutschek, 28 - *Hepatic Anomalies*, in *Obstetric Imaging: Fetal Diagnosis and Care (Second Edition)*, J.A. Copel, et al., Editors. 2018, Elsevier. p. 130-137.e132.
5. P. E. Sigismund, J. Zenk, M. Koch, et al., "*Nearly 3,000 salivary stones: Some clinical and epidemiologic aspects*". The Laryngoscope, 2015. **125**(8): p. 1879-1882.
6. S. Kraaij, K. H. Karagozoglu, T. Forouzanfar, et al., "*Salivary stones: symptoms, aetiology, biochemical composition and treatment*". Bdj, 2014. **217**: p. E23.
7. A. Graham, S. Lubner, A. B. Wolfson, "*Urolithiasis in the emergency department*". Emergency medicine clinics of North America, 2011. **29**(3): p. 519-538.
8. C. D. Lallas, X. S. Liu, A. N. Chiura, et al., "*Urolithiasis location and size and the association with microhematuria and stone-related symptoms*". J Endourol, 2011. **25**(12): p. 1909-1913.
9. C. Türk, A. Neisius, A. Petřík, et al., *EAU Guidelines on Urolithiasis 2018*, in *European Association of Urology Guidelines. 2018 Edition*. 2018, The European Association of Urology Guidelines Office: Arnhem, The Netherlands.
10. I. Sorokin, C. Mamoulakis, K. Miyazawa, et al., "*Epidemiology of stone disease across the world*". World Journal of Urology, 2017. **35**(9): p. 1301-1320.
11. *Epidemiology of Nephrolithiasis*, in *Primer on the Metabolic Bone Diseases and Disorders of Mineral Metabolism*.
12. A. Ramello, C. Vitale, M. Marangella, "*Epidemiology of nephrolithiasis*". Journal of nephrology, 2001. **13**: p. S45-S50.
13. J. Shoag, G. E. Tasian, D. S. Goldfarb, et al., "*The New Epidemiology of Nephrolithiasis*". Advances in Chronic Kidney Disease, 2015. **22**(4): p. 273-278.
14. C. D. Scales, Jr., A. C. Smith, J. M. Hanley, et al., "*Prevalence of kidney stones in the United States*". European urology, 2012. **62**(1): p. 160-165.
15. F. Wimpissinger, C. Turk, O. Kheifets, et al., "*The silence of the stones: asymptomatic ureteral calculi*". J Urol, 2007. **178**(4 Pt 1): p. 1341-1344; discussion 1344.
16. F. Chen, "*Genetic and developmental basis for urinary tract obstruction*". Pediatric Nephrology, 2009. **24**(9): p. 1621-1632.

-
17. R. L. Chevalier, "*Molecular and cellular pathophysiology of obstructive nephropathy*". Pediatric Nephrology, 1999. **13**(7): p. 612-619.
 18. G. Jindal, P. Ramchandani, "*Acute Flank Pain Secondary to Urolithiasis: Radiologic Evaluation and Alternate Diagnoses*". Radiologic Clinics of North America, 2007. **45**(3): p. 395-410.
 19. O. W. Moe, "*Kidney stones: pathophysiology and medical management*". Lancet (London, England), 2006. **367**(9507): p. 333-344.
 20. T. Knoll, "*Epidemiology, Pathogenesis, and Pathophysiology of Urolithiasis*". European Urology Supplements, 2010. **9**(12): p. 802-806.
 21. W. L. Strohmaier, "*Epidemiologie und Pathogenese der Urolithiasis*", in *Die Urologie*, M.S. Michel, et al., Editors. 2016, Springer Berlin Heidelberg: Berlin, Heidelberg. p. 473-478.
 22. F. L. Coe, A. P. Evan, E. M. Worcester, et al., "*Three pathways for human kidney stone formation*". Urol Res, 2010. **38**(3): p. 147-160.
 23. F. L. Coe, J. Keck, E. R. Norton, "*The natural history of calcium urolithiasis*". JAMA, 1977. **238**(14): p. 1519-1523.
 24. C. Türk, A. Petřík, K. Sarica, et al., "*EAU Guidelines on Interventional Treatment for Urolithiasis*". European urology, 2016. **69**(3): p. 475-482.
 25. V. G. Dell'Orto, E. A. Belotti, B. Goeggel-Simonetti, et al., "*Metabolic disturbances and renal stone promotion on treatment with topiramate: a systematic review*". British journal of clinical pharmacology, 2014. **77**(6): p. 958-964.
 26. T. Yasui, A. Okada, M. Usami, et al., "*2082 Association of the Loci 5Q35.3, 7Q14.3, and 13.Q14.1 with urolithiasis: A case-control study in the Japanese population, involving genome-wide association study*". The Journal of Urology, 2013. **189**(4): p. e854.
 27. R. L. Kuo, J. E. Lingeman, A. P. Evan, et al., "*Urine calcium and volume predict coverage of renal papilla by Randall's plaque*". Kidney international, 2003. **64**(6): p. 2150-2154.
 28. S. C. Kim, F. L. Coe, W. W. Tinmouth, et al., "*Stone formation is proportional to papillary surface coverage by Randall's plaque*". J Urol, 2005. **173**(1): p. 117-119; discussion 119.
 29. N. L. Miller, D. L. Gillen, J. C. Williams, Jr., et al., "*A formal test of the hypothesis that idiopathic calcium oxalate stones grow on Randall's plaque*". BJU international, 2009. **103**(7): p. 966-971.
 30. N. L. Miller, J. C. Williams, Jr., A. P. Evan, et al., "*In idiopathic calcium oxalate stone-formers, unattached stones show evidence of having originated as attached stones on Randall's plaque*". BJU international, 2010. **105**(2): p. 242-245.
 31. R. K. Low, M. L. Stoller, "*Endoscopic mapping of renal papillae for Randall's plaques in patients with urinary stone disease*". J Urol, 1997. **158**(6): p. 2062-2064.
 32. F. J. Sampaio, A. H. Aragao, "*Anatomical relationship between the intrarenal arteries and the kidney collecting system*". J Urol, 1990. **143**(4): p. 679-681.
 33. R. Smith-Bindman, C. Aubin, J. Bailitz, et al., "*Ultrasonography versus computed tomography for suspected nephrolithiasis*". The New England journal of medicine, 2014. **371**(12): p. 1100-1110.

-
34. A. A. Ray, D. Ghiculete, K. T. Pace, et al., "*Limitations to ultrasound in the detection and measurement of urinary tract calculi*". Urology, 2010. **76**(2): p. 295-300.
35. V. Ganesan, S. De, D. Greene, et al., "*Accuracy of ultrasonography for renal stone detection and size determination: is it good enough for management decisions?*". BJU international, 2017. **119**(3): p. 464-469.
36. A. G. Martov, D. A. Mazurenko, M. M. Klimkova, et al., "*[Dual energy computed tomography in diagnosis of urolithiasis: a new method for determining the chemical composition of urinary stones]*". Urologiia (Moscow, Russia : 1999), 2017(3): p. 98-103.
37. L. B. Kapanadze, S. K. Ternovoy, V. I. Rudenko, et al., "*[Clinical implications of dual-energy computed tomography in the diagnosis and treatment of urolithiasis]*". Urologiia (Moscow, Russia : 1999), 2018(1): p. 143-149.
38. M. Ilyas, G. Dev, A. Gupta, et al., "*Dual-energy computed tomography: A reliable and established tool for In vivo differentiation of uric acid from nonuric acid renal Stones*". The Nigerian postgraduate medical journal, 2018. **25**(1): p. 52-59.
39. A. Franken, P. A. Gevenois, A. V. Muylem, et al., "*In Vivo Differentiation of Uric Acid Versus Non-Uric Acid Urinary Calculi With Third-Generation Dual-Source Dual-Energy CT at Reduced Radiation Dose*". AJR. American journal of roentgenology, 2018. **210**(2): p. 358-363.
40. X. Zheng, Y. Liu, M. Li, et al., "*Dual-energy computed tomography for characterizing urinary calcified calculi and uric acid calculi: A meta-analysis*". European journal of radiology, 2016. **85**(10): p. 1843-1848.
41. M. Sudah, "Re: *Christian Türk, Aleš Petřík, Kemal Sarica, et al. EAU Guidelines on Diagnosis and Conservative Management of Urolithiasis. Eur Urol 2016;69:468-74 2013;74*". European urology, 2016. **69**(4): p. e76-e77.
42. A. Leppert, S. Nadalin, E. Schirg, et al., "*Impact of magnetic resonance urography on preoperative diagnostic workup in children affected by hydronephrosis: should IVU be replaced?*". Journal of pediatric surgery, 2002. **37**(10): p. 1441-1445.
43. G. E. Tasian, L. Copelovitch, "*Evaluation and medical management of kidney stones in children*". J Urol, 2014. **192**(5): p. 1329-1336.
44. C. Passerotti, J. S. Chow, A. Silva, et al., "*Ultrasound versus computerized tomography for evaluating urolithiasis*". J Urol, 2009. **182**(4 Suppl): p. 1829-1834.
45. M. M. Chen, F. V. Coakley, A. Kaimal, et al., "*Guidelines for computed tomography and magnetic resonance imaging use during pregnancy and lactation*". Obstetrics & Gynecology, 2008. **112**(2): p. 333-340.
46. "*Committee Opinion No. 656: Guidelines for Diagnostic Imaging During Pregnancy and Lactation*". Obstetrics and gynecology, 2016. **127**(2): p. e75-80.
47. E. Tremblay, E. Thérasse, I. Thomassin-Naggara, et al., "*Quality Initiatives: Guidelines for Use of Medical Imaging during Pregnancy and Lactation*". RadioGraphics, 2012. **32**(3): p. 897-911.
48. R. Siener, D. Ebert, C. Nicolay, et al., "*Dietary risk factors for hyperoxaluria in calcium oxalate stone formers*". Kidney international, 2003. **63**(3): p. 1037-1043.
49. L. Borghi, T. Schianchi, T. Meschi, et al., "*Comparison of two diets for the prevention of recurrent stones in idiopathic hypercalciuria*". The New England journal of medicine, 2002. **346**(2): p. 77-84.

50. H. A. Fink, J. W. Akornor, P. S. Garimella, et al., "*Diet, fluid, or supplements for secondary prevention of nephrolithiasis: a systematic review and meta-analysis of randomized trials*". *European urology*, 2009. **56**(1): p. 72-80.
51. H. A. Fink, T. J. Wilt, K. E. Eidman, et al., "*Medical management to prevent recurrent nephrolithiasis in adults: a systematic review for an American College of Physicians Clinical Guideline*". *Ann Intern Med*, 2013. **158**(7): p. 535-543.
52. J. S. Rodman, J. J. Williams, C. M. Peterson, "*Dissolution of uric acid calculi*". *J Urol*, 1984. **131**(6): p. 1039-1044.
53. G. Becker, "*The CARI guidelines. Kidney stones: uric acid stones*". *Nephrology (Carlton, Vic.)*, 2007. **12 Suppl 1**: p. S21-25.
54. O. El-Gamal, M. El-Bendary, M. Ragab, et al., "*Role of combined use of potassium citrate and tamsulosin in the management of uric acid distal ureteral calculi*". *Urol Res*, 2012. **40**(3): p. 219-224.
55. B. M. Dropkin, R. A. Moses, D. Sharma, et al., "*The Natural History of Nonobstructing Asymptomatic Renal Stones Managed with Active Surveillance*". *The Journal of Urology*, 2015. **193**(4): p. 1265-1269.
56. A. M. Loske, *Shock Wave Lithotripsy*, in *Medical and Biomedical Applications of Shock Waves*. 2017, Springer International Publishing: Cham. p. 83-187.
57. H.-G. Tiselius, C. G. Chaussy, "*Arguments for choosing extracorporeal shockwave lithotripsy for removal of urinary tract stones*". *Urolithiasis*, 2015. **43**(5): p. 387-396.
58. B. Christian, S. C. G., S. Frank, "*Improvement of SWL Efficacy: Reduction of the Respiration-Induced Kidney Motion by Using an Abdominal Compression Plate*". *Journal of Endourology*, 2016. **30**(4): p. 411-416.
59. P. Shen, M. Jiang, J. Yang, et al., "*Use of ureteral stent in extracorporeal shock wave lithotripsy for upper urinary calculi: a systematic review and meta-analysis*". *J Urol*, 2011. **186**(4): p. 1328-1335.
60. H. Wang, L. Man, G. Li, et al., "*Meta-Analysis of Stenting versus Non-Stenting for the Treatment of Ureteral Stones*". *PLoS One*, 2017. **12**(1): p. e0167670.
61. A. Skolarikos, N. Grivas, P. Kallidonis, et al., "*The Efficacy of Medical Expulsive Therapy (MET) in Improving Stone-free Rate and Stone Expulsion Time, After Extracorporeal Shock Wave Lithotripsy (SWL) for Upper Urinary Stones: A Systematic Review and Meta-analysis*". *Urology*, 2015. **86**(6): p. 1057-1064.
62. Y. Ruhayel, A. Tepeler, S. Dabestani, et al., "*Tract Sizes in Miniaturized Percutaneous Nephrolithotomy: A Systematic Review from the European Association of Urology Urolithiasis Guidelines Panel*". *European urology*, 2017. **72**(2): p. 220-235.
63. E. C. Carlos, D. A. Wollin, B. B. Winship, et al., "*In Vitro Comparison of a Novel Single Probe Dual-Energy Lithotripter to Current Devices*". *J Endourol*, 2018. **32**(6): p. 534-540.
64. C. B. H., M. A. A., d. I. R. Thomas, et al., "*Benchtop and Initial Clinical Evaluation of the ShockPulse Stone Eliminator in Percutaneous Nephrolithotomy*". *Journal of Endourology*, 2017. **31**(2): p. 191-197.
65. P. Olbert, J. Weber, A. Hegele, et al., "*Combining Lithoclast and ultrasound power in one device for percutaneous nephrolithotomy: in vitro results of a novel and highly effective technology*". *Urology*, 2003. **61**(1): p. 55-59; discussion 59.
66. G. R. M., J. Patrick, S. B. K., "*Worldwide Trends of Urinary Stone Disease Treatment Over the Last Two Decades: A Systematic Review*". *Journal of Endourology*, 2017. **31**(6): p. 547-556.

-
67. G. M. Preminger, H. G. Tiselius, D. G. Assimos, et al., "2007 guideline for the management of ureteral calculi". J Urol, 2007. **178**(6): p. 2418-2434.
68. M. Ordon, S. Andonian, B. Blew, et al., "CUA Guideline: Management of ureteral calculi". Canadian Urological Association journal = Journal de l'Association des urologues du Canada, 2015. **9**(11-12): p. E837-851.
69. G. Wendt-Nordahl, T. Mut, P. Krombach, et al., "Do new generation flexible ureterorenoscopes offer a higher treatment success than their predecessors?". Urol Res, 2011. **39**(3): p. 185-188.
70. M. T. Gettman, J. W. Segura, "Management of ureteric stones: issues and controversies". BJU international, 2005. **95**: p. 85-93.
71. S. P. Dretler, "Laser lithotripsy: a review of 20 years of research and clinical applications". Lasers Surg Med, 1988. **8**(4): p. 341-356.
72. A. Hofstetter, "Lasers in urology". Lasers Surg Med, 1986. **6**(4): p. 412-414.
73. A. Vogel, "Nonlinear absorption: intraocular microsurgery and laser lithotripsy". Physics in medicine and biology, 1997. **42**(5): p. 895-912.
74. B. Altay, B. Erkurt, S. Albayrak, "A review study to evaluate holmium:YAG laser lithotripsy with flexible ureteroscopy in patients on ongoing oral anticoagulant therapy". Lasers in Medical Science, 2017. **32**(7): p. 1615-1619.
75. A. Hofstetter, "The Laser in Urology (State of the Art)". Laser-Medizin: eine interdisziplinäre Zeitschrift ; Praxis, Klinik, Forschung, 2000. **15**(4): p. 155-160.
76. E. D. Jansen, T. G. van Leeuwen, M. Motamedi, et al., "Temperature dependence of the absorption coefficient of water for midinfrared laser radiation". Lasers in Surgery and Medicine, 1994. **14**(3): p. 258-268.
77. J. T. Walsh, Jr., J. P. Cummings, "Effect of the dynamic optical properties of water on midinfrared laser ablation". Lasers Surg Med, 1994. **15**(3): p. 295-305.
78. B. Alexander, A. I. Fishman, M. Grasso, "Ureteroscopy and laser lithotripsy: technologic advancements". World Journal of Urology, 2015. **33**(2): p. 247-256.
79. P. A. Geavlete, D. Georgescu, R. Muțescu, et al., Chapter 6 - Retrograde Ureteroscopy in the Treatment of Upper Urinary Tract Lithiasis, in Retrograde Ureteroscopy, P.A. Geavlete, Editor. 2016, Academic Press: San Diego. p. 105-216.
80. H. Lee, H. W. Kang, J. M. H. Teichman, et al., "Urinary calculus fragmentation during Ho: YAG and Er:YAG lithotripsy". Lasers in Surgery and Medicine, 2006. **38**(1): p. 39-51.
81. N. M. Fried, "Recent advances in infrared laser lithotripsy [Invited]". Biomedical Optics Express, 2018. **9**(9): p. 4552-4568.
82. D. M. Wieliczka, S. Weng, M. R. Querry, "Wedge shaped cell for highly absorbent liquids: infrared optical constants of water". Applied optics, 1989. **28**(9): p. 1714-1719.
83. M. M. Elhilali, S. Badaan, A. Ibrahim, et al., "Use of the Moses Technology to Improve Holmium Laser Lithotripsy Outcomes: A Preclinical Study". Journal of Endourology, 2017. **31**(6): p. 598-604.
84. T. C. Hutchens, D. A. Gonzalez, P. B. Irby, et al., "Fiber optic muzzle brake tip for reducing fiber burnback and stone repulsion during thulium fiber laser lithotripsy". Journal of Biomedical Optics, 2017. **22**(1): p. 018001.

-
85. P. Kronenberg, O. Traxer, "Update on lasers in urology 2014: current assessment on holmium:yttrium-aluminum-garnet (Ho:YAG) laser lithotripter settings and laser fibers". *World J Urol*, 2015. **33**(4): p. 463-469.
86. R. Sroka, N. Haseke, T. Pongratz, et al., "In vitro investigations of repulsion during laser lithotripsy using a pendulum set-up". *Lasers in Medical Science*, 2012. **27**(3): p. 637-643.
87. J. J. Zhang, D. Rajabhandharaks, J. R. Xuan, et al., "Calculus migration characterization during Ho:YAG laser lithotripsy by high-speed camera using suspended pendulum method". *Lasers in Medical Science*, 2017. **32**(5): p. 1017-1021.
88. H. W. Kang, H. Lee, J. M. H. Teichman, et al., "Dependence of calculus retropulsion on pulse duration during HO: YAG laser lithotripsy". *Lasers in Surgery and Medicine*, 2006. **38**(8): p. 762-772.
89. H. O. Lee, R. T. Ryan, J. M. H. Teichman, et al., "Stone Retropulsion During Holmium:Yag Lithotripsy". *The Journal of Urology*, 2003. **169**(3): p. 881-885.
90. J. Sea, L. M. Jonat, B. H. Chew, et al., "Optimal Power Settings for Holmium:YAG Lithotripsy". *The Journal of Urology*, 2012. **187**(3): p. 914-919.
91. M. Sofer, J. D. Watterson, T. A. Wollin, et al., "Holmium:YAG Laser Lithotripsy for upper urinary tract calculi in 598 patients". *The Journal of Urology*, 2002. **167**(1): p. 31-34.
92. B. Somani, M. Desai, O. Traxer, et al., *Stone-free rate (SFR): A new proposal for defining levels of SFR*. Vol. 42. 2013.
93. K. Peter, "Editorial Comment on: Ureteroscopic High-Frequency Dusting Utilizing a 120-W Holmium Laser by Tracey et al". *Journal of Endourology*, 2018. **32**(4): p. 296-296.
94. S. Hein, A. Miernik, K. Wilhelm, et al., "Clinical significance of residual fragments in 2015: impact, detection, and how to avoid them". *World Journal of Urology*, 2016. **34**(6): p. 771-778.
95. J. F. Donaldson, M. Lardas, D. Scrimgeour, et al., "Systematic Review and Meta-analysis of the Clinical Effectiveness of Shock Wave Lithotripsy, Retrograde Intrarenal Surgery, and Percutaneous Nephrolithotomy for Lower-pole Renal Stones". *European urology*, 2015. **67**(4): p. 612-616.
96. A. E. Perlmutter, C. Talug, W. F. Tarry, et al., "Impact of Stone Location on Success Rates of Endoscopic Lithotripsy for Nephrolithiasis". *Urology*, 2008. **71**(2): p. 214-217.
97. R. M. Vilches, A. Aliaga, D. Reyes, et al., "Comparison between retrograde intrarenal surgery and extracorporeal shock wave lithotripsy in the treatment of lower pole kidney stones up to 15mm. Prospective, randomized study". *Actas Urológicas Españolas (English Edition)*, 2015. **39**(4): p. 236-242.
98. T. Drake, N. Grivas, S. Dabestani, et al., "What are the Benefits and Harms of Ureteroscopy Compared with Shock-wave Lithotripsy in the Treatment of Upper Ureteral Stones? A Systematic Review". *European urology*, 2017. **72**(5): p. 772-786.
99. M. Ursiny, A. Yaghoubian, M. Humphreys, et al., "PD53-02 Cost-Effectiveness of Dusting vs. Basketing Intrarenal Stones: A Study From the Edge Consortium". *The Journal of Urology*, 2018. **199**(4, Supplement): p. e1046-e1047.
100. L. Roger, R. David, K. Mohamed, et al., "High-Frequency Dusting Versus Conventional Holmium Laser Lithotripsy for Intrarenal and Ureteral Calculi". *Journal of Endourology*, 2017. **31**(3): p. 272-277.

-
101. M. B. R., C. Ben, E. Brian, et al., "Ureteroscopic Laser Lithotripsy: A Review of Dusting vs Fragmentation with Extraction". *Journal of Endourology*, 2018. **32**(1): p. 1-6.
 102. A. H. Aldoukhi, W. W. Roberts, T. L. Hall, et al., "Understanding the Popcorn Effect During Holmium Laser Lithotripsy for Dusting". *Urology*, 2018.
 103. M. S. Nomikos, G. Koritsiadis, N. Bafaloukas, et al., "P10 - Safety and efficacy of high power Holmium-Yag laser in percutaneous nephrolithotomy". *European Urology Supplements*, 2018. **17**(4): p. e2017.
 104. J. W. Lee, J. Park, M. C. Cho, et al., "PD30-12 How to perform the dusting technique for calcium oxalate stones during Ho:YAG lithotripsy". *The Journal of Urology*, 2017. **197**(4): p. 582.
 105. S. Chen, L. Zhu, S. Yang, et al., "High- vs Low-power Holmium Laser Lithotripsy: A Prospective, Randomized Study in Patients Undergoing Multitract Minipercutaneous Nephrolithotomy". *Urology*, 2012. **79**(2): p. 293-297.
 106. S. Hein, R. Petzold, M. Schoenthaler, et al., "Thermal effects of Ho: YAG laser lithotripsy: real-time evaluation in an in vitro model". *World Journal of Urology*, 2018.
 107. A. H. Aldoukhi, K. R. Ghani, T. L. Hall, et al., "Thermal Response to High-Power Holmium Laser Lithotripsy". *J Endourol*, 2017. **31**(12): p. 1308-1312.
 108. A. H. Aldoukhi, T. L. Hall, K. R. Ghani, et al., "Caliceal Fluid Temperature During High-Power Holmium Laser Lithotripsy in an In Vivo Porcine Model". *J Endourol*, 2018.
 109. W. R. Molina, I. N. Silva, R. Donalisio da Silva, et al., "Influence of saline on temperature profile of laser lithotripsy activation". *J Endourol*, 2015. **29**(2): p. 235-239.
 110. D. A. Wollin, E. C. Carlos, W. R. Tom, et al., "Effect of Laser Settings and Irrigation Rates on Ureteral Temperature During Holmium Laser Lithotripsy, an In Vitro Model". *J Endourol*, 2018. **32**(1): p. 59-63.
 111. B. Lange, J. Cordes, R. Brinkmann, "Stone/tissue differentiation for holmium laser lithotripsy using autofluorescence". *Lasers in Surgery and Medicine*, 2015. **47**(9): p. 737-744.
 112. B. Lange, D. Jocham, R. Brinkmann, et al., "Stone/ tissue differentiation for Holmium laser lithotripsy using autofluorescence: Clinical proof of concept study". *Lasers Surg Med*, 2017. **49**(4): p. 361-365.
 113. K. Xavier, G. W. Hruby, C. R. Kelly, et al., "Clinical Evaluation of Efficacy of Novel Optically Activated Digital Endoscope Protection System Against Laser Energy Damage". *Urology*, 2009. **73**(1): p. 37-40.
 114. T. C. Hutchens, D. A. Gonzalez, P. B. Irby, et al. *Fiber optic muzzle brake tip for reducing fiber burnback and stone retropulsion during thulium fiber laser lithotripsy*. 2017. SPIE.
 115. C. R. Wilson, J. D. Kennedy, P. B. Irby, et al. *Anti-reflection coated optical fibers for use in thulium fiber laser lithotripsy*. in *SPIE BiOS*. 2017. SPIE.
 116. C. R. Wilson, J. D. D. Kennedy, P. B. Irby, et al. *Miniature ureteroscope distal tip designs for potential use in thulium fiber laser lithotripsy*. 2018. SPIE.
 117. L. A. Hardy, D. A. Gonzalez, P. B. Irby, et al. *Fragmentation and dusting of large kidney stones using compact, air-cooled, high peak power, 1940-nm, Thulium fiber laser*. in *SPIE BiOS*. 2018. SPIE.
 118. D. A. Wollin, A. Ackerman, C. Yang, et al., "Variable Pulse Duration From a New Holmium:YAG Laser: The Effect on Stone Comminution, Fiber Tip Degradation, and Retropulsion in a Dusting Model". *Urology*, 2017. **103**: p. 47-51.

-
119. M. J. Bader, T. Pongratz, W. Khoder, et al., "*Impact of pulse duration on Ho:YAG laser lithotripsy: fragmentation and dusting performance*". World Journal of Urology, 2015. **33**(4): p. 471-477.
 120. E. Maximilian, S. Stephan, P. Thomas, et al., "*In vitro investigations of propulsion during laser lithotripsy using video tracking*". Lasers in Surgery and Medicine, 2018. **50**(4): p. 333-339.
 121. K. Stock, D. Steigenhöfer, T. Pongratz, et al., "*Investigation on cavitation bubble dynamics induced by clinically available Ho:YAG lasers*". Photonics \& Lasers in Medicine, 2016. **5**(2).
 122. D. E. Dolmans, D. Fukumura, R. K. Jain, "*Photodynamic therapy for cancer*". Nature reviews. Cancer, 2003. **3**(5): p. 380-387.
 123. T. J. Dougherty, C. J. Gomer, B. W. Henderson, et al., "*Photodynamic therapy*". Journal of the National Cancer Institute, 1998. **90**(12): p. 889-905.
 124. H. I. Pass, "*Photodynamic therapy in oncology: mechanisms and clinical use*". Journal of the National Cancer Institute, 1993. **85**(6): p. 443-456.
 125. M. Burger, D. Zaak, C. G. Stief, et al., "*Photodynamic diagnostics and noninvasive bladder cancer: is it cost-effective in long-term application? A Germany-based cost analysis*". European urology, 2007. **52**(1): p. 142-147.
 126. S. Denzinger, M. Burger, "*Photodynamic diagnostics of bladder tumors*". Current urology reports, 2008. **9**(2): p. 101-105.
 127. E. K. Chan, B. Sorg, D. Protsenko, et al., "*Effects of compression on soft tissue optical properties*". {IEEE} Journal of Selected Topics in Quantum Electronics, 1996. **2**(4): p. 943-950.
 128. S. L. Jacques, "*Optical properties of biological tissues: a review*". Physics in Medicine & Biology, 2013. **58**(11): p. R37.
 129. S. Andersson-Engels, C. Klinteberg, K. Svanberg, et al., "*In vivo fluorescence imaging for tissue diagnostics*". Physics in medicine and biology, 1997. **42**(5): p. 815-824.
 130. J. Hegyi, V. Hegyi, T. Ruzicka, et al., "*New developments in fluorescence diagnostics*". Journal der Deutschen Dermatologischen Gesellschaft = Journal of the German Society of Dermatology : JDDG, 2011. **9**(5): p. 368-372.
 131. S. Prahl, *Optical Property Measurements Using the Inverse Adding Doubling Program*. 2011.
 132. S. A. Prahl, M. J. C. van Gemert, A. J. Welch, "*Determining the optical properties of turbid media by using the adding-doubling method*". Applied optics, 1993. **32**(4): p. 559-568.
 133. M. Pilz, S. Honold, A. Kienle, "*Determination of the optical properties of turbid media by measurements of the spatially resolved reflectance considering the point-spread function of the camera system*". J Biomed Opt, 2008. **13**(5): p. 054047.
 134. T. J. Beck, T. Pongratz, W. Stummer, et al. *Clinical Determination of Tissue Optical Properties in vivo by Spatially Resolved Reflectance Measurements*. in *Photon Migration and Diffuse-Light Imaging*. 2003. Munich: Optical Society of America.
 135. A. Kim, B. C. Wilson, *Measurement of ex vivo and in vivo tissue optical properties: methods and theories*, in *Optical-Thermal Response of Laser-Irradiated Tissue*. 2010, Springer. p. 267-319.
 136. D. W. Burden, "*Guide to the disruption of biological samples-2012*". Random Primers, 2012. **12**(1).
 137. V. V. Tuchin, *Optical clearing of tissues and blood*. 2006: Spie Press Bellingham.

-
138. E. A. Genina, A. N. Bashkatov, V. I. Kochubey, et al., "*Effect of storage conditions of skin samples on their optical characteristics*". Optics and Spectroscopy, 2009. **107**(6): p. 934.
139. D. B. MacDougall, "*Changes in the colour and opacity of meat*". Food Chemistry, 1982. **9**(1): p. 75-88.
140. B. M. Nicolăi, K. Beullens, E. Bobelyn, et al., "*Nondestructive measurement of fruit and vegetable quality by means of NIR spectroscopy: A review*". Postharvest Biology and Technology, 2007. **46**(2): p. 99-118.



DANKSAGUNG

Seit meinem Start im Juli 2014 am LIFE Zentrum um meine Projektstudie als Vorbereitung zur Masterarbeit durchzuführen, durfte ich zahlreiche neue Personen und Persönlichkeiten kennen lernen. Aus vielen Arbeitskollegen wurden geschätzte Freunde, mit denen auch in Zukunft der Kontakt gepflegt wird.

Allen voran möchte ich Ronald Sroka für seine inzwischen doch langjährige Unterstützung in privaten und beruflichen Angelegenheiten danken. Durch seinen Führungsstil war und ist stets eine tolle Arbeitsatmosphäre im LIFE-Team gegeben. Besonders sein Engagement zur Förderung der Motivation Neues auszuprobieren und kreative Ansätze oder themenübergreifende Ideen aufzugreifen, machte die Arbeit am LIFE-Zentrum interessant.

Bei Adrian Rühm und Herbert Stepp bedanke ich mich für ihre langjährige Zusammenarbeit und intensive Diskussionsrunden. Durch ihre Erfahrung wurden Problemstellungen aus anderer Perspektive kritisch hinterfragt und neue kreative Ansätze gefunden.

Thomas Pongratz war in allen Arbeiten durch seine technische Unterstützung beteiligt und lockerte mit seinem trockenen Humor zur rechten Zeit den Tagesablauf auf. Ein herzliches Dankeschön an dieser Stelle für die Hilfe seit meinem Start am LFL.

Besonderer Dank gilt auch all den Praktikanten, Bacheloranden, Masteranden, Doktoranden und Mitarbeitern, die das LFL erst zu dem machen, was es ist. Unter anderem die Vorbereitung und Durchführung der PDT-Konferenz in Kochel hat gezeigt, was für ein starkes und harmonisierendes Team am LFL ansässig ist.

Ein Dankeschön geht auch speziell an alle LFL-Doktoranden: Max Aumiller, Christian Feymüller, Christian Heckl, Stephan Ströbl und an den langjährigen Wegbegleiter Alexander Lang.

Stephan Ströbl ist besonders hervorzuheben, der seit seiner Bachelorarbeit ein geschätzter Freund, Publikationspartner und Büro-Genosse geworden ist. Viel Erfolg weiterhin bei der Promotion in Vorarlberg.

Bei Christian Heckl möchte ich mich für die vielen konstruktiven Gespräche, Diskussionen und Korrekturvorschläge bedanken und wünsche auch ihm nur das Beste für sein Promotionsvorhaben.

Stephan Dittmar wurde zu einem guten Freund und war durch sein lasertechnisches Fachwissen eine große Hilfe bei der Planung und Durchführung der Experimente.

Der medizinische Teil dieser Arbeit wurde insbesondere durch den Freund und Arbeitskollegen Frank Strittmatter unterstützt. Ein herzliches Dankeschön für die Einblicke in die Medizin und die Erklärungen der urologischen Diagnostik und Therapie.

Auch Herrn Jörg Schirra möchte ich für seine medizinische Unterstützung in gastroenterologischen Fragestellungen und den Einblick in dieses Feld der Medizin danken.

Dem ganzen Team der Metzgerei Weichart danke ich für die langjährige Unterstützung der Arbeiten am LFL, aber auch für ihre kulinarische Versorgung an Weihnachtsfeiern, Sommerfesten oder einem gelegentlichen Grillen im Innenhof.

Zu guter Letzt bedanke ich mich bei meiner Familie für die Unterstützung und Geduld zu meinem Promotionsvorhaben. Besonders dankbar bin ich für den tatkräftigen Beistand meiner Freundin Daniela, die durch interessante Diskussionen einen Teil dieser Arbeit mitgestaltet hat.

LEBENS LAUF

PERSÖNLICHE DATEN

Name: Eisel, Maximilian
Geburtsdatum und Ort: 23.02.1990 in Weilheim i. OB.

BERUFSERFAHRUNG

03/2016 – heute Promotion (Dr. rer. biol. hum.) am Laser-Forschungslabor, Klinikum der Universität München („Untersuchungen zur laserinduzierten Lithotripsie“)

03/2016 – 03/2017 R&D Assistant bei StarMedTec GmbH (Boston Scientific)

05/2015 – 11/2015 Masterarbeit am Laser-Forschungslabor, Klinikum der Universität München („Vergleichende Messung optischer Eigenschaften von biologischem Gewebe mittels Ulbrichtkugel, orts aufgelöster Remission und interstitieller Messmethodik“)

11/2013 – 02/2014 Bachelorarbeit bei Truma Gerätetechnik GmbH, Entwicklungsabteilung für Heizgeräte;
(„Programmierung einer LabVIEW-Steuerung für hand- und teilautomatisierten Betrieb eines neuartigen Brenners“)

07/2012 – 03/2013 Praxissemester bei Truma Gerätetechnik GmbH, Entwicklungsabteilung für Heizgeräte; „Serienbetreuung dieselbetriebener Heizgeräte der Firma Truma“ (Steuerungstests, Klimakammer-Versuche, Dauerlauf tests- Durchführung und Betreuung). Anschließend Werksstudententätigkeit mit ähnlichem Betätigungsfeld bis 03/2014

SCHULE & STUDIUM

03/2014 – 03/2016 Master of Science | Photonik (2.0)
Hochschule München

10/2010 – 03/2014 Bachelor of Science (2.5) | Physikalische Technik
Hochschule München

09/1996 – 07/2009 Grundschule und Gymnasium
Allgemeine Hochschulreife (3.0) in Tutzing

WISSENSCHAFTLICHE LEHRE

Betreuung wissenschaftlicher Arbeiten

Masterarbeiten:

Stephan Ströbl (Ludwig-Maximilians-Universität, Fakultät für Physik, Abgabe: 20.09.2017)
“Investigations on laserinduced Ho:YAG lithotripsy“

Nikolas Dominik (Ludwig-Maximilians-Universität, Fakultät für Physik, Abgabe: 24.11.2017) *“Optical-fiber-based localization of blood via ICG fluorescence detection or remission spectrometry and of PpIX fluorescence in turbid media“*

Bachelorarbeiten:

Stephan Ströbl (Ludwig-Maximilians-Universität, Fakultät für Physik, Abgabe: 11.07.2015)
„Untersuchungen zur fasergestützten Temperaturmessung mittels Rubinfluoreszenz“

Kevin Scharl (Ludwig-Maximilians-Universität, Fakultät für Physik, Abgabe: 20.07.2017)
„Untersuchung von Ho:YAG-Laser-induzierten Kavitationsblasen“

Yik Long Li (Carl von Ossietzky Universität Oldenburg, Engineering Physics, Abgabe: 25.09.2017) *“Investigations for DPM-Er:YAG Lasers application in Medicine“*

Markus Kasparofsky (Ludwig-Maximilians-Universität, Fakultät für Physik, Abgabe: noch ausstehend) *„Untersuchungen von 2 μ m- und 3 μ m-Laserstrahlung für die Laserlithotripsie“*

Praktikanten:

Mang Wang, (Gaststudent:Shanghai University Hospital, Department of Urology) Messungen zur Laserlithotripsie (Fragmentation, Propulsion)

Masa al Masri (Carl von Ossietzky Universität Oldenburg, Engineering Physics), Referenzmessungen zur Propulsion mit BEGO Kugeln, Fluoreszenzuntersuchungen humaner Nierensteine

Martin van Beke (Ludwig-Maximilians-Universität, Fakultät für Medizin) Evaluation von einweg- und mehrweg-Endoskopen für die Laserlithotripsie

Vorlesungsaktivität

07/2018 Organisator des Sommer-Seminars des LIFE-Zentrums (3-tägiges Labor Off-Site); Softskill – Vortrag über „Lab-Journals: Modern Docuementation and Archiving“

09/2017 Organisator des Sommer-Seminars des LIFE-Zentrums (3-tägiges Labor Off-Site); Softskill – Vortrag über: „Dokumentation und Archivierung im Labor“

Halbjährlich: Vortragender in der Vorlesungsreihe „Physikalische und biomolekulare Methoden in der medizinischen Forschung“ über Optische Gewebeeigenschaften, Laserinduzierte Lithotripsie, Laser- & Lichtquellen und Pathogenese humaner Steine



EIDESSTATTLICHE VERSICHERUNG

Ich erkläre hiermit an Eides statt,

dass ich die vorliegende Dissertation mit dem Thema

Untersuchungen zur laserinduzierten Lithotripsie

selbständig verfasst, mich außer der angegebenen keiner weiteren Hilfsmittel bedient und alle Erkenntnisse, die aus dem Schrifttum ganz oder annähernd übernommen sind, als solche kenntlich gemacht und nach ihrer Herkunft unter Bezeichnung der Fundstelle einzeln nachgewiesen habe.

Ich erkläre des Weiteren, dass die hier vorgelegte Dissertation nicht in gleicher oder in ähnlicher Form bei einer anderen Stelle zur Erlangung eines akademischen Grades eingereicht wurde.

München, 18.12.2019

Ort, Datum

Maximilian Eisel

Unterschrift Doktorand